Engineering Journal

First Quarter 2023 | Volume 60, No. 1

Smarter. Stronger. Steel.

Engineering Journal

American Institute of Steel Construction

Dedicated to the development and improvement of steel construction, through the interchange of ideas, experiences, and data.

Engineering Journal (ISSN 0013-8029) is published quarterly. Published by the American Institute of Steel Construction at 130 E Randolph Street, Suite 2000, Chicago, IL 60601.

Archives: Search at **aisc.org/ej**. Article downloads are free for current members and are available for a nominal fee for non-members.

Experimental Evaluation on Lateral Torsional Buckling Resistance of Continuous Steel Stringers

C. Shawn Sun, Daniel G. Linzell, Jay A. Puckett, and Ahmed Rageh

ABSTRACT

An extensive experimental study evaluated lateral torsional buckling resistance of two-span, continuous, steel beams in a test assembly that included three beam lines, an interior transverse support (floor beam), and transverse diaphragms at the end supports. Funded by the Louisiana Transportation Research Center (LTRC), this study was conducted to better understand continuous stringer behavior so that simplified analyses would better capture their lateral torsional buckling (LTB) behavior. Current practice produces Louisiana Department of Transportation and Development (LA DOTD) bridge ratings often conservatively controlled by stringer LTB capacity and, in many cases, necessitates posting—thereby imposing significant and often unnecessary operational restrictions. Forty-seven elastic tests were completed. The tests encompassed a variety of unbraced lengths and support conditions with steel diaphragms or timber ties acting as bracing members. The interior beam in the test assembly was loaded orthogonal to its strong axis at the middle of one or both spans using a spreader beam that minimized restraint and prevented the development of follower forces. Tests demonstrated that minimal bracing could significantly increase lateral torsional buckling resistance and justify a higher LTB resistance than what is currently used. Although the tests were conducted on assemblies used to represent a bridge floor system, the results provided an extensive set of valuable data that could be used by structural steel researchers interested in examining flexural resistance of continuous beams.

Keywords: continuous, stringers, lateral torsional buckling, bracing.

INTRODUCTION

Some of Louisiana's bridges built in the 1950s and 1960s used two-girder or truss systems, in which floor beams are supported by main longitudinal members that then support continuous stringers (Figure 1). When the continuous stringers are load-rated, lateral torsional buckling (LTB) resistance is calculated in accordance with the *AASHTO LRFD Bridge Design Specifications* (AASHTO BDS) (AASHTO, 2020), which does not attempt to account for bracing effects that could be provided by a noncomposite deck. Consequently, LTB resistance can be underestimated and may necessitate load restrictions via unnecessarily conservative postings (Sun et al., 2021). This study, funded by the Louisiana Transportation Research Center (LTRC), was conducted to explore the development of more realistic replication of actual LTB resistance for continuous stringers supported by transverse floor beams. This paper presents the first set of tests of a reduced-scale assembly, those completed before placement of a noncomposite concrete deck, whose focus was examining LTB behavior of an interior, longitudinal stringer. These tests are generally applicable to LTB of any continuous steel beam, and the extensive amount of test results that were generated should be of interest to the steel research community.

C. Shawn Sun, Ph.D., PE, Assistant Professor, Department of Civil Engineering and Construction Management, California State University, Northridge, Calif. Email: shawn.sun@csun.edu (corresponding)

Daniel G. Linzell, Ph.D., PE, F.ASCE, F.SEI, Associate Dean and Leslie D. Martin Professor, Department of Civil and Environmental Engineering, University of Nebraska-Lincoln, Lincoln, Neb. Email: dlinzell@unl.edu

Jay A. Puckett, Ph.D., PE, F.ASCE, Professor, Durham School of Architectural Engineering and Construction, University of Nebraska-Lincoln, Omaha, Neb. Email: Jay.Puckett@unl.edu

Ahmed Rageh, Ph.D., Project Engineer, SDR Engineering, Tallahassee, Fla. Email: a.eissa.rageh@gmail.com

Paper No. 2021-08R

EXPERIMENTAL PROGRAM

As stated earlier, this paper summarizes an experimental program examining LTB resistance of two-span, continuous, steel stringers in a test assembly. The test assembly had three beam lines, an interior transverse support, and transverse diaphragms at its end supports. Forty-seven elastic tests were completed. The tests encompassed a variety of unbraced lengths and support conditions with steel diaphragms or timber ties acting as bracing members. The interior beam in the test assembly was loaded orthogonal to its strong axis at the middle of one or both spans using a spreader beam system that minimized restraint and prevented development of follower forces.

Test Setup

The test assembly was designed to address critical parameters from a group of representative bridges, including span, spacing, stringer size, material properties, and support

conditions. The test assembly also accommodated a variety of bracing configurations, stringer-to-floor beam relative stiffness, and connection fixity conditions. The test assembly included three lines of 50-ft-long W16×31 stringers, one 25-ft-long W24×68 floor beam, and C12×20 end diaphragms bolted to the stringers. Figures 2 and 3 show the framing plan and a section at the floor beam, respectively. Stringer center-to-center span lengths were 24 ft. The floor beam was supported by interior steel bearing plates at the stringer locations to represent a rigid support (neglect floor beam displacements). Without these interior plates, the floor beam was free to bend between its end supports, thereby representing flexible supports for the stringers. Additionally, the stringer bottom flange was bolted or unbolted to the floor beam to simulate various fixity conditions. The bolted condition provided resistance to slippage and anchored the bottom flange to the floor beam, thereby providing rotational (i.e., torsional) resistance. Without the bolts, the floor beam acted as a vertical bearing support, and any translational resistance was provided by friction that might occur between the stringer and floor beam flanges. The stringer bottom flange was also free to uplift from the floor beam flange due to torsion.

Grade 50 W16×31 sections were selected for the stringers because they represent stringers used on Louisiana bridges. They also were expected to exhibit elastic LTB behavior, which allowed for repetitive tests. Furthermore, Gr. 50 yield strengths vary less than Gr. 36, and steel grade minimally impacts controlling L_b or L_r.

Test Matrix

Table 1 provides the test matrix, including test groupings, corresponding configurations (i.e., test setups), stringer support conditions (i.e., floor beam flexural stiffness), loading and bracing conditions, and assigned test identification numbers. The experimental program included test setups with and without a noncomposite concrete deck. This paper addresses the tests without the deck, which are categorized into three general groups. A concentrated force was applied at midspan of one or both spans for balanced and unbalanced loading conditions, respectively.

A balanced load referred to a load case in which both spans of the interior stringer were loaded at midspan. An unbalanced load meant that one span of the interior stringer was loaded at midspan. For illustration purposes, Figure 4 shows one- and two-point loads at midspan of the interior stringer, and corresponding moment diagrams are illustrated in Figure 5. When an unbalanced load was applied, the unloaded stringer end was tied to the strong floor to avoid uplift. Stringer geometry measurements were collected using laser scans prior to the tests. The maximum

Fig. 1. I-10 Mississippi River Bridge in Port Allen, La. (photo courtesy of Suba Herath).

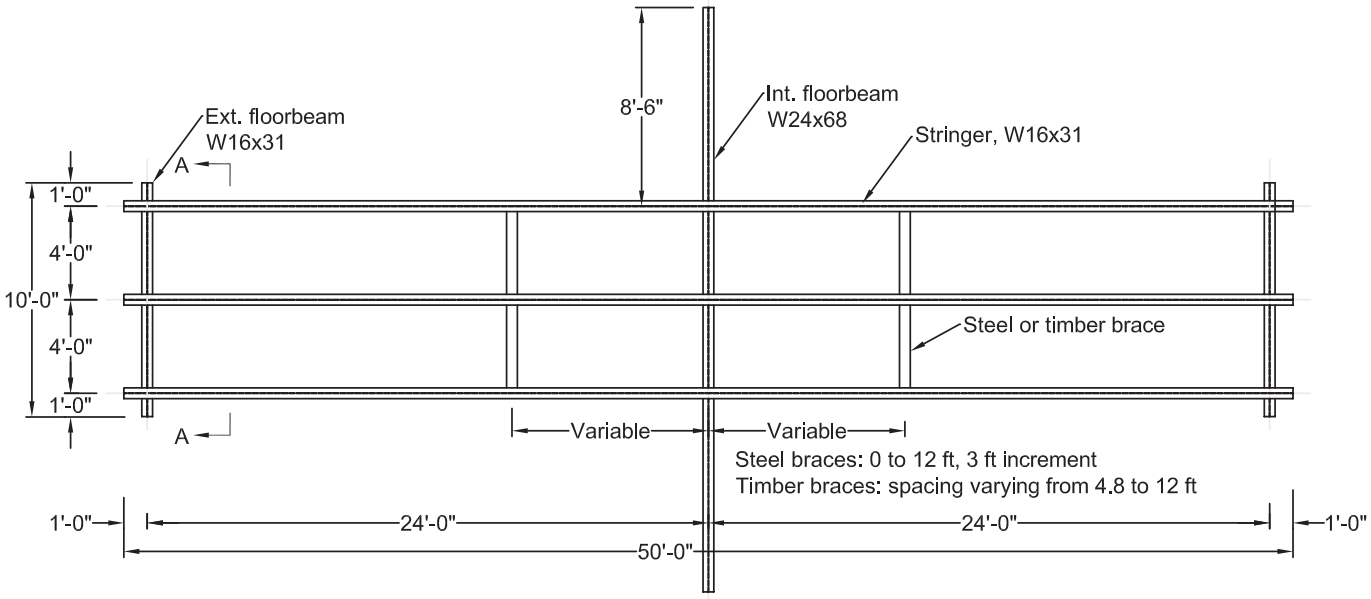

Fig. 2. Test assembly framing plan.

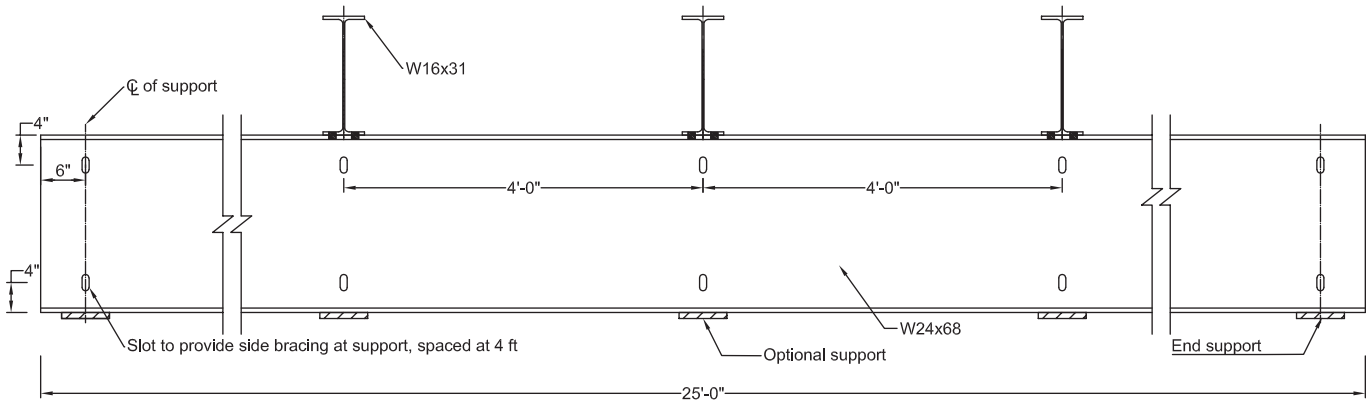

Fig. 3. Test assembly section at floor beam.

Table 1. Test Matrix					
Group	Description of Boundary Conditions			Load Condition	Test No.
	Interior Support at Center Stringer	Top Flange of Stringer	Stringer Bottom Flange to Floor Beam Connection		
I	Rigid	Unbraced	Unbolted to floor beam	1 point load	1
				2 point loads	2
			Bolted to floor beam	1 point load	3
				2 point loads	4
	Flexible		Unbolted to floor beam	1 point load	5
				2 point loads	6
			Bolted to floor beam	1 point load	7
				2 point loads	8
II	Rigid	Diaphragms at interior support	Unbolted to floor beam	1 point load	9
				2 point loads	10
		Diaphragms at $L/2$		1 point load	11
				2 point loads	12
		Diaphragms at $L/8$ from interior support		1 point load	13
				2 point loads	14
		Diaphragms at $L/4$ from interior support		1 point load	15
				2 point loads	16
		Diaphragms at $3L/8$ from interior support		1 point load	17
				2 point loads	18
	Rigid	Diaphragms at interior support	Bolted to floor beam	1 point load	19
				2 point loads	20
		Diaphragms at $L/2$		1 point load	21
				2 point loads	22
		Diaphragms at $L/8$ from interior support		1 point load	23
				2 point loads	24
		Diaphragms at $L/4$ from interior support		1 point load	25
				2 point loads	26
		Diaphragms at $3L/8$ from interior support		1 point load	27
				2 point loads	28

(table continued on next page)

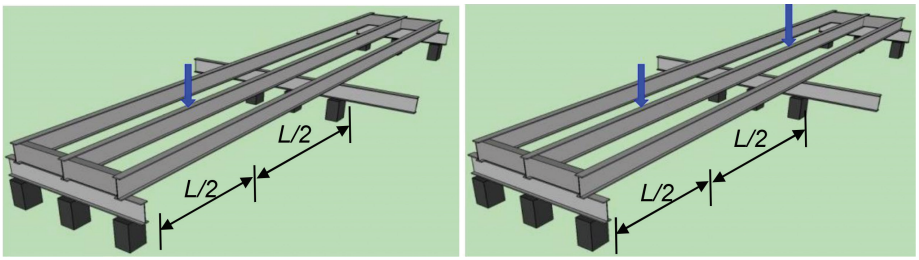

(a) Unbalanced load *(b) Balanced load*

Fig. 4. Load conditions.

Table 1. Test Matrix (continued)					
	Description of Boundary Conditions				
Group	Interior Support at Center Stringer	Top Flange of Stringer	Stringer Bottom Flange to Floor Beam Connection	Load Condition	Test No.
III	Rigid	Timber ties at *L*/2	Unbolted to floor beam	2 point loads	29
		Timber ties at *L*/3			30
		Timber ties at *L*/4, *L*/2, *L*, *L*/2, *L*/4			30'
		Timber ties at *L*/4			31
		Timber ties at *L*/5			32
		Timber ties at *L*/2	Bolted to floor beam	2 point loads	33
		Timber ties at *L*/3			34
		Timber ties at *L*/4, *L*/2, *L*, *L*/2, *L*/4			34'
		Timber ties at *L*/4			35
		Timber ties at *L*/5			36
		Timber ties at *L*/8, *L*/4, *L*/2, L, *L*/8, L/4, L/2			36'
	Flexible	Timber ties at *L*/2	Unbolted to floor beam	2 point loads	37
		Timber ties at *L*/3			38
		Timber ties at *L*/4			39
		Timber ties at *L*/5			40
		Timber ties at *L*/2	Bolted to floor beam	2 point loads	41
		Timber ties at *L*/3			42
		Timber ties at *L*/4			43
		Timber ties at *L*/5			44

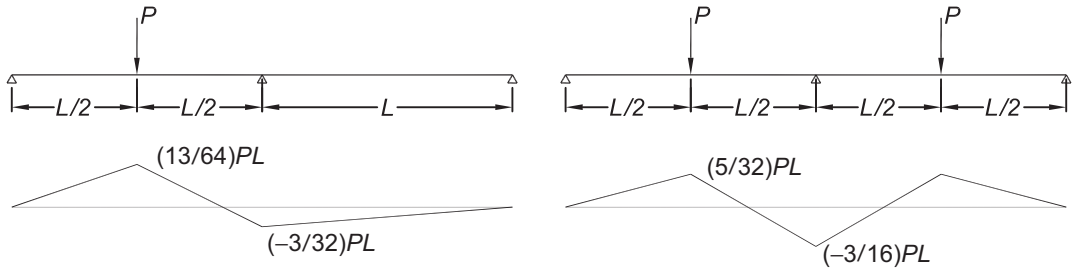

(a)Unbalanced load *(b) balanced load*

Fig. 5. Moment diagrams for two-span stringer.

sweep imperfection was approximately $L/1500$ (L = span) for the top flange at midspan.

Group I included Tests 1 to 8, in which the stringer top flanges were unbraced (Figure 6). Either a rigid or flexible interior floor beam supported the stringers. A rigid interior support was provided beneath the stringers by supporting the floor beam on the laboratory strong floor along its length using steel plates. Stringer bottom flanges were either unbolted or bolted to the floor beam. When bolted, four ⅞-in.-diameter high-strength bolts were used. No stringer stiffeners were provided over the floor beam. Group I tests served as a baseline for comparison to other tests.

As shown in Figure 7, the load application system included upper and lower bearing plates with a spherical bearing between them. A load cell was installed between the upper plate and spreader beam to monitor the applied loads. A lubricant was applied to the spherical bearing to minimize friction between the spherical bearing and plates. As a result, rotational and lateral restraints from the load point were minimized. In addition, potential bracing

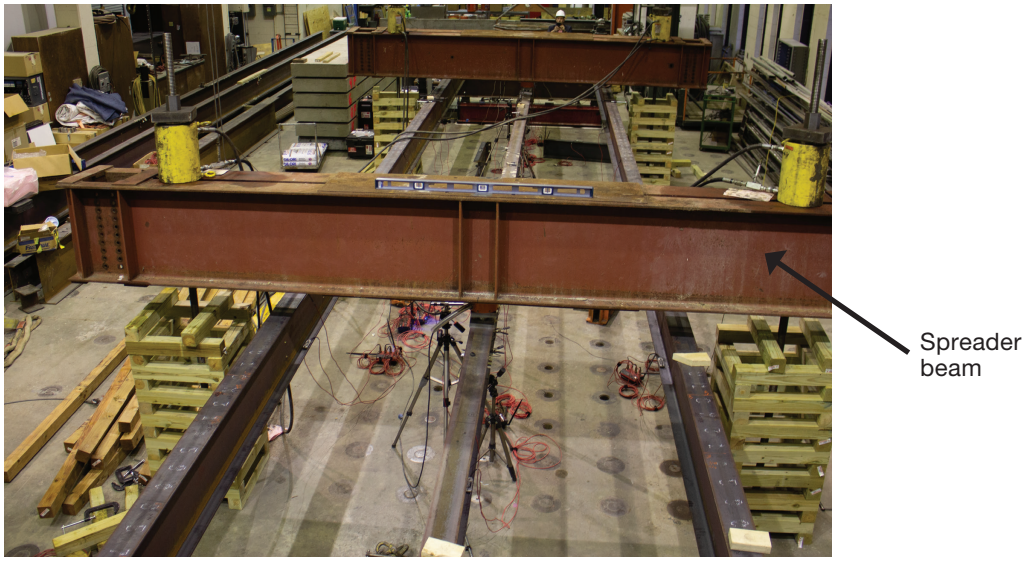

Fig. 6. Example Group I setup.

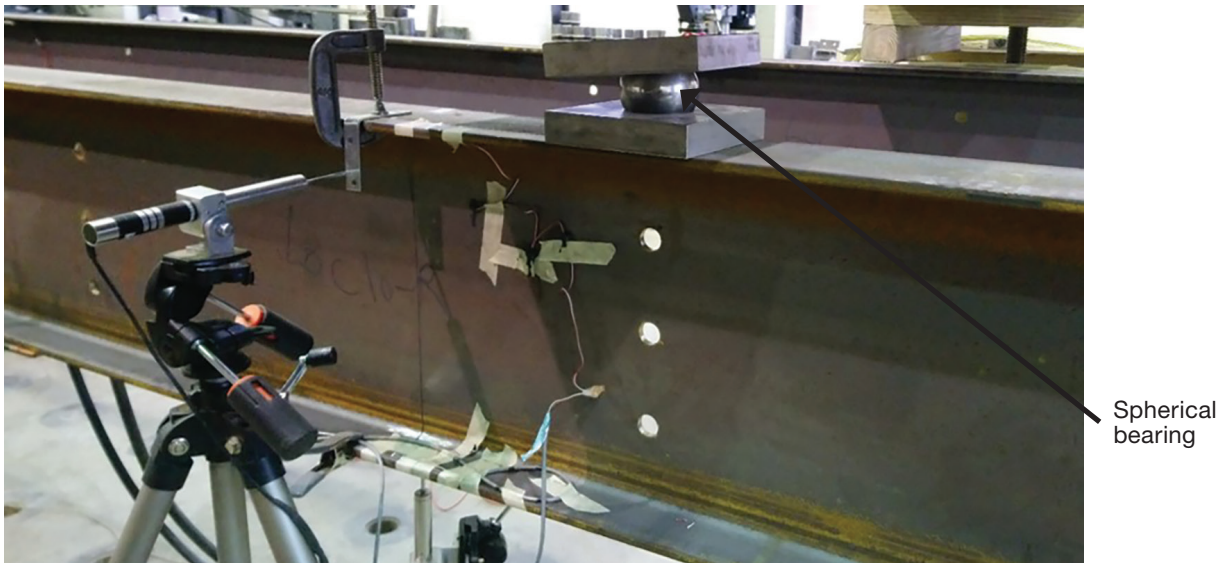

Fig. 7. Load application detail.

restraint from the spreader beams used to apply point loads was minimal because the spreader beam above the load cell was supported at its ends by two vertical threaded rods, whose flexural stiffness was measured and shown to be negligible.

Group II included Tests 9 to 28, where the stringers were braced by intermediate steel diaphragms at various locations, including the interior support and $L/2$, $L/8$, $L/4$, and $3L/8$ away from the interior support, where L is the span length. Diaphragms were bolted to the stringers, and the floor beam was supported along its length by the laboratory strong floor. Again, the stringer bottom flanges were either unbolted or bolted to the floor beam, and balanced and unbalanced loads were applied. Figure 8 depicts a representative Group II test.

Group III included Tests 29 to 44, in which the stringer top flanges were laterally braced using #2 red pine timber ties (4 in. × 4 in.) connected using C-clamps (Figure 9). Lateral support included a range of bracing locations before a noncomposite concrete deck was placed and allowed for a wide range of lateral support conditions to be efficiently studied. Consistent with the other groups, rigid or flexible interior floor beam support was provided, and stringer bottom flanges were either unbolted or bolted to the floor beam. Balanced loads were applied.

Instrumentation

Load and pressure cells, strain gages and transducers, and linear variable differential transformers (LVDTs) measured applied forces and structural response. Instrument locations are detailed in Figure 10. Strain gages and transducers were placed at multiple sections on the interior stringer and transducers at critical exterior stringer sections to capture effects due to primary, weak-axis, and lateral bending moments, as well as axial loads. Transducers were installed on both the top and bottom flanges. LVDTs were placed at midspan of the interior stringer in both spans and were oriented to capture vertical and lateral deflections. Load and pressure cells were provided at the spreader beams to apply load. Results were commonly reported at four critical locations as described in Table 2. Figures 11 and 12 detail LVDTs, strain gages, and transducers at Locations 10 and 4 (see Figure 10), respectively.

Test Results

Test results for Group I and III are provided herein. Representative results are presented as plots of applied load versus stringer vertical and lateral deflections, and load versus stringer strains. Applied load versus axial, and lateral, primary, out-of-plane, bending normal stress components are

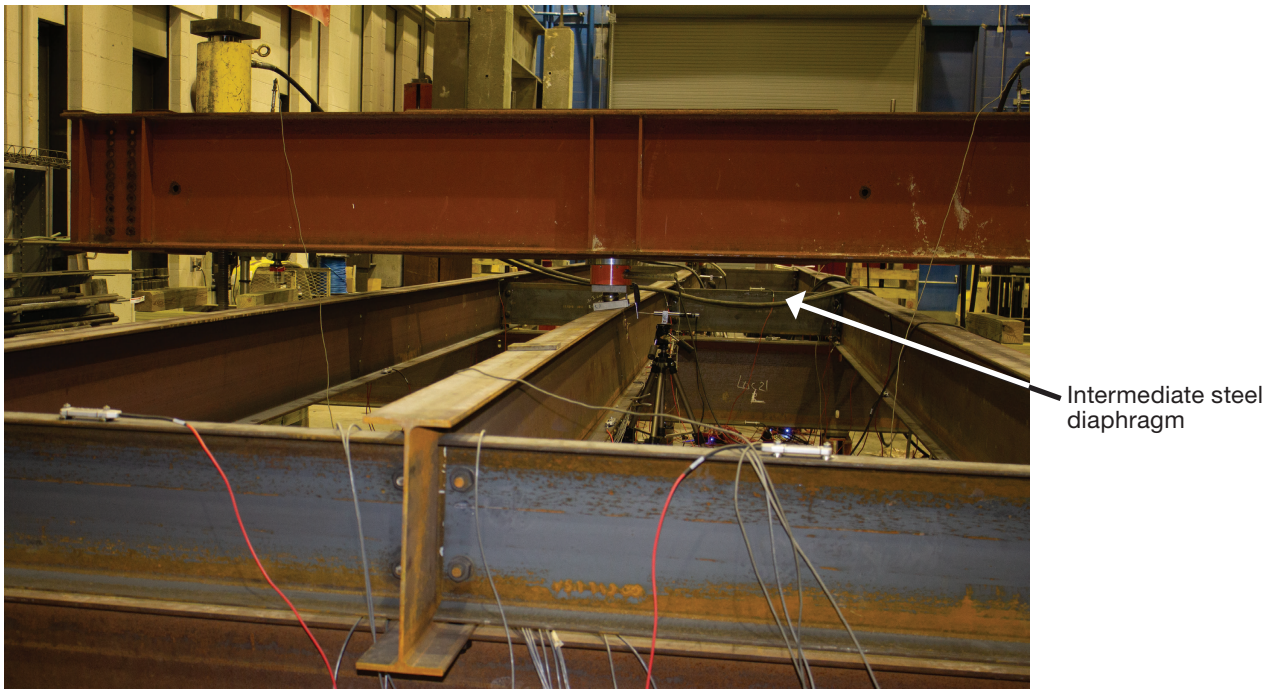

Fig. 8. Example Group II setup.

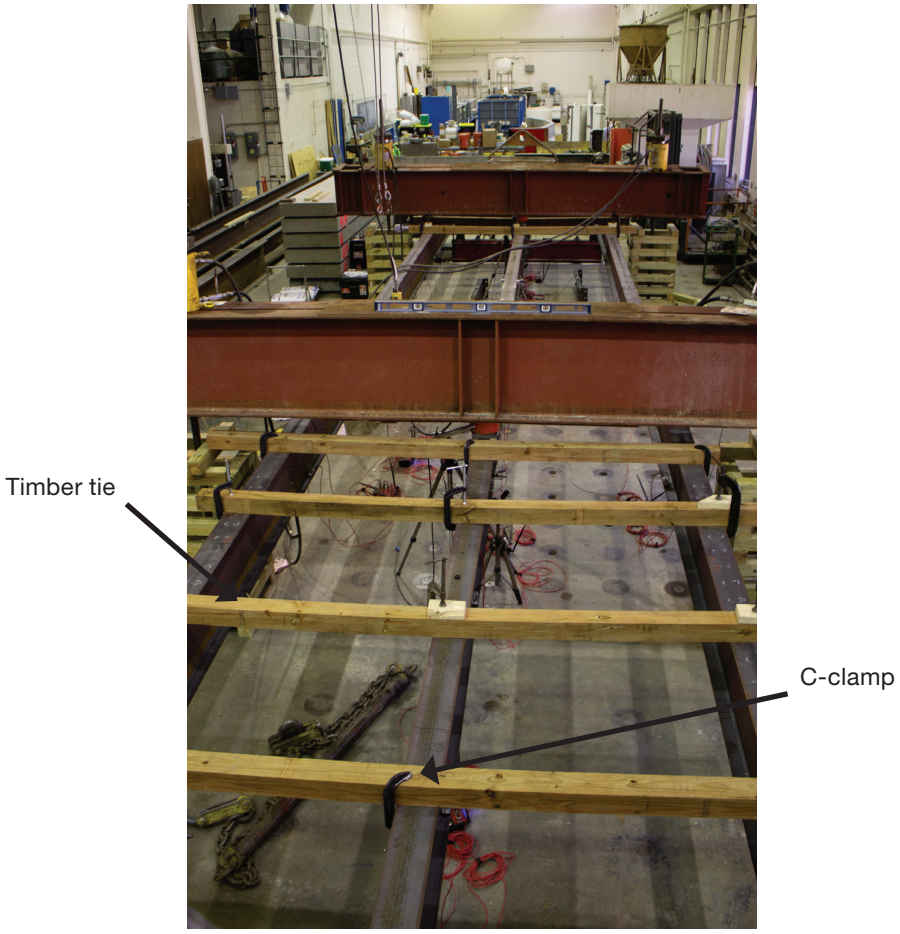

Fig. 9. Example Group III setup.

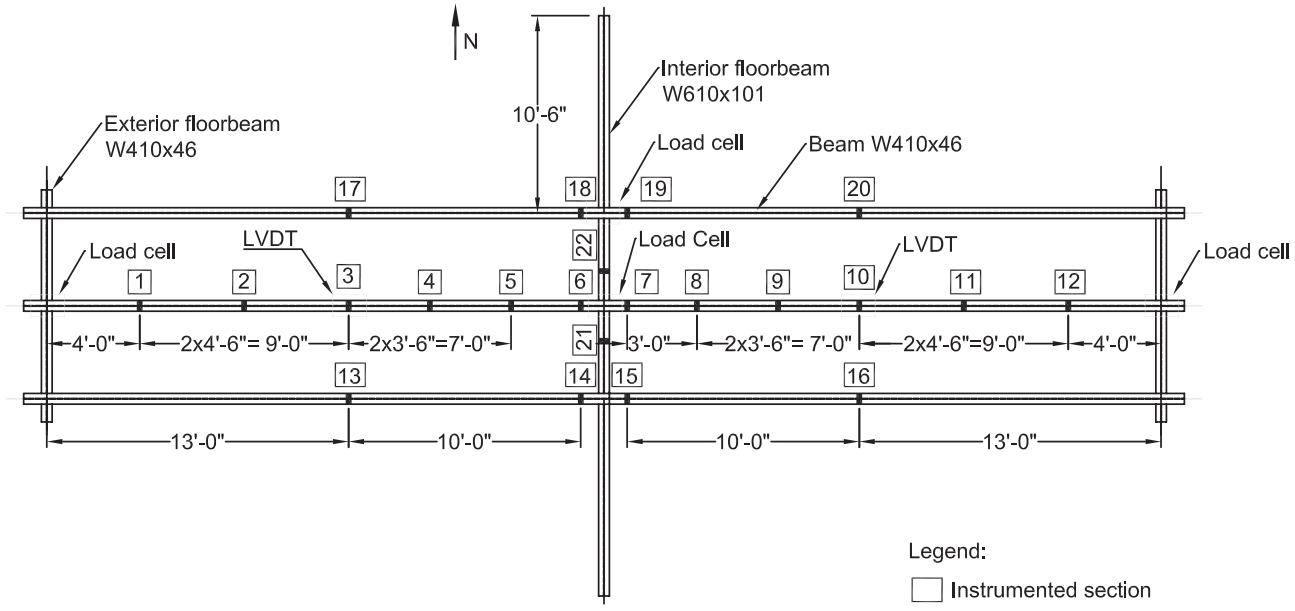

Fig. 10. Instrumentation plan view.

Table 2. Critical Locations	
Location	**Description**
3	Midspan maximum + M when loaded at Location 3 Midspan – M when loaded at Location 10 (see Figure 6)
6	Critical – M location adjacent to floor beam
7	Critical – M location adjacent to floor beam
10	Midspan maximum + M when loaded at Location 10 Midspan – M when loaded at Location 3 (see Figure 6)

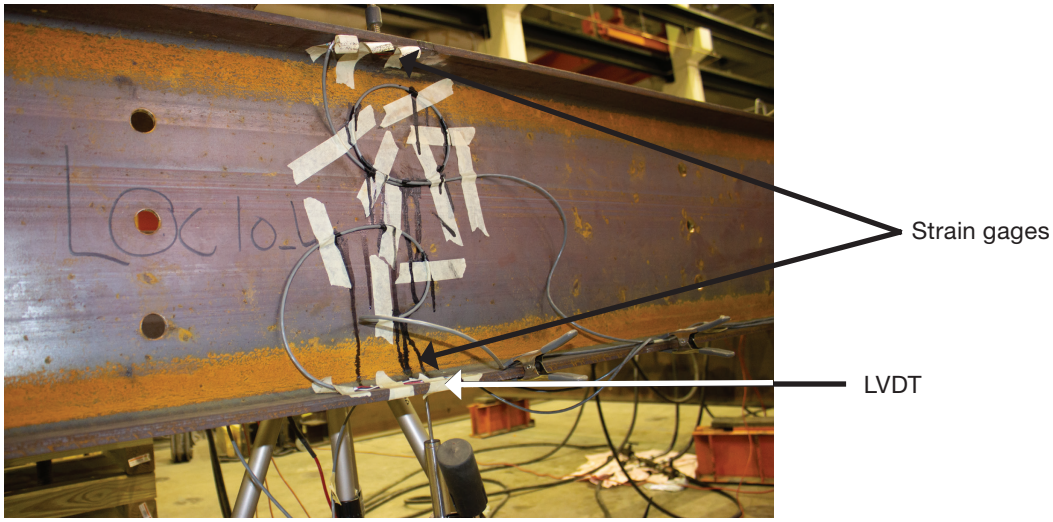

Fig. 11. LVDT and strain transducers, Location 10.

Fig. 12. Strain gage, Location 4.

Table 3. Test and Elastic Analysis Stresses, Spreader Beam Placement							
Gauge		One Spreader Beam (Unbalanced Load)			Two Spreader Beams (Balanced Load)		
		Measured Stress (ksi)	Predicted Stress (ksi)	Ratio	Measured Stress (ksi)	Predicted Stress (ksi)	Ratio
Ch0	Top	1.04	1.15	90%	–2.58	–2.96	87%
Ch1	Bottom	–0.98	–1.15	85%	3.03	2.96	103%
Ch2	Bottom	–0.98	–1.15	85%	2.71	2.96	92%

also provided. More complete data are provided in Sun et al. (2021).

Group I Tests—Unbraced

As indicated in Table 1, Group I tests had no intermediate bracing. Figure 13 depicts Test No. 3, showing vertical and lateral LVDTs on the interior stringer, the spreader beam, and corresponding load cell at midspan, a supported floor beam, and the bolted connection between the interior stringer and floor beam.

Each spreader beam weighed approximately 3.7 kips. For tests that had loads applied at midspan of both spans, data were recorded as the spreader beams were sequentially placed onto the test assembly and measured deflections caused by their placement compared well with elastic analyses. Corresponding measured, midspan stresses from strain data were comparable to calculated stresses as shown in Table 3.

Tests 1, 3, 5, and 7 results are presented for discussion purposes because they experienced LTB and accounted for various support and bracing conditions: a rigid or flexible interior floor beam with the stringer bottom flanges either unbolted or bolted to the floor beam. Load-lateral deflection plots in Figure 14 show that Test No. 3 provided the largest lateral stiffness because stringer bottom flanges were bolted to the floor beam and the interior support was considered rigid (i.e., floor beam supported along its length). There is apparent noise in the plots in Figure 14 because tests were run in force control and applied loads were manually controlled, resulting in some relaxation of the system after each load step. Figure 15 depicts the LTB of the interior stringer for Test No. 3. Test No. 1 exhibited the highest lateral flexibility because stringer bottom flanges were not bolted to the floor beam. Tests 5 and 7, both of which had flexible interior supports and unbolted and bolted stringer flanges, exhibited lateral stiffness between Tests 1 and 3. Test No. 7 provided slightly higher lateral stiffness than Test No. 5 because stringer bottom flanges were bolted to the floor beam.

Figures 16 and 17 present load-strain plots for transducers at Location 3 TN (top north) and TS (top south) for the four tests. Figure 18 identifies transducer locations. Test No. 1 exhibited comparable strains to the other three tests until it reached peak load, which, again, was lower than that for the other tests. LTB was evident via measured bifurcation for three of the four tests.

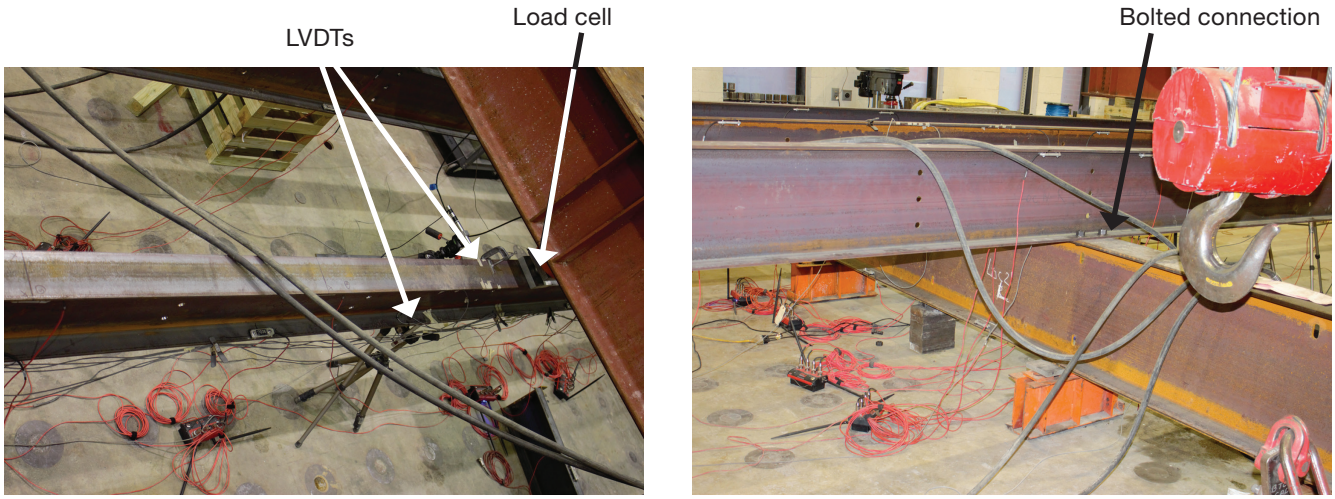

(a) Midspan LVDTs and load cell *(b) Supports and bolted connection at floor beam*

Fig. 13. Test No. 3.

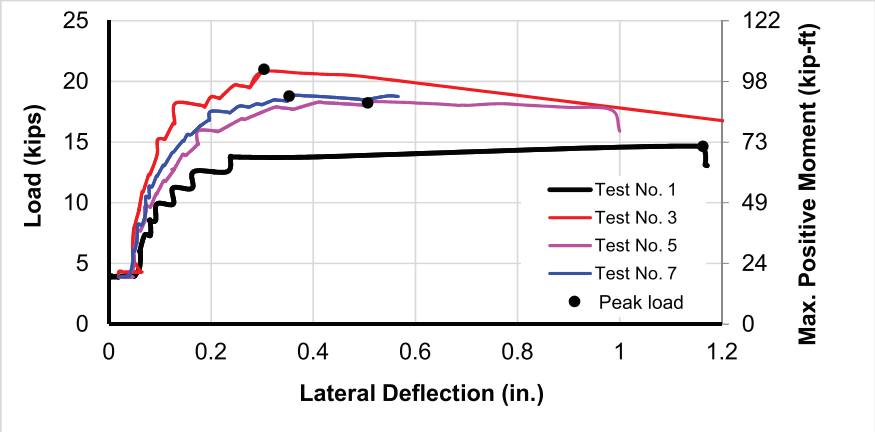

Fig. 14. Load versus lateral deflections, Tests 1, 3, 5, and 7.

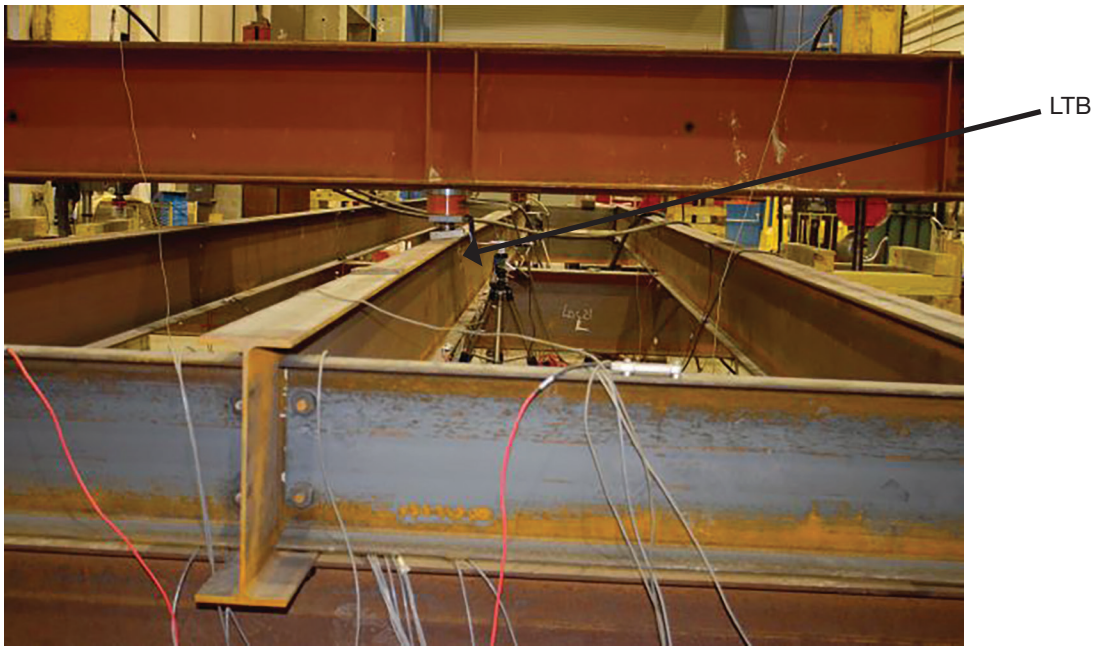

Fig. 15. LTB of the interior stringer, Test No. 3.

To further assess behavior at a typical section, strains were converted to stresses and values were decoupled to capture axial (σ_a), and primary (σ_x), out-of-plane (σ_y), and lateral bending (σ_w) normal stress components. Equations 1 through 4 detail relationships between total stress and its components at each of the four instrument locations in a typical cross section (i.e., TN, TS, BN, and BS in Figure 18).

$$f_{TN} = -\sigma_x + \sigma_y - \sigma_w + \sigma_a \quad (1)$$

$$f_{TS} = -\sigma_x - \sigma_y + \sigma_w + \sigma_a \quad (2)$$

$$f_{BN} = \sigma_x + \sigma_y + \sigma_w + \sigma_a \quad (3)$$

$$f_{BS} = \sigma_x - \sigma_y - \sigma_w + \sigma_a \quad (4)$$

For illustrative purposes, Figure 19 shows stress components at Location 3 TN for Test No. 1. As expected, the axial stress was zero, while weak-axis and lateral bending stresses shown in Figures 19 through 22 experienced a gradual increase after peak load, indicating LTB. As shown in Figures 19 and 20, the magnitude and sign associated with top of flange out-of-plane and lateral bending stresses influenced total stress. Figures 21 and 22, which plot bottom flange stress components, indicate that out-of-plane and lateral bending stresses were of opposite sign and did not significantly affect total stress.

Figure 23 illustrates the effect of floor beam relative stiffness on observed response for Tests 1 to 8. For most cases, a flexible floor beam resulted in an appreciable difference in LTB resistance, with peak loads changing by more than 25%. Negative moments decreased due to translation of the floor beam. Figure 24 illustrates the effect of the stringer-to-floor beam fixity for Tests 1 to 8. LTB commonly occurred at higher applied loads when the stringer bottom flange was connected to the floor beam because of increased lateral restraint. Stringer bracing conditions over the floor beam were established to represent continuous stringers in Louisiana bridges. As stated earlier, Group I tests served as comparison baselines for the additional noncomposite tests (Sun et al., 2022). As a result, a diaphragm

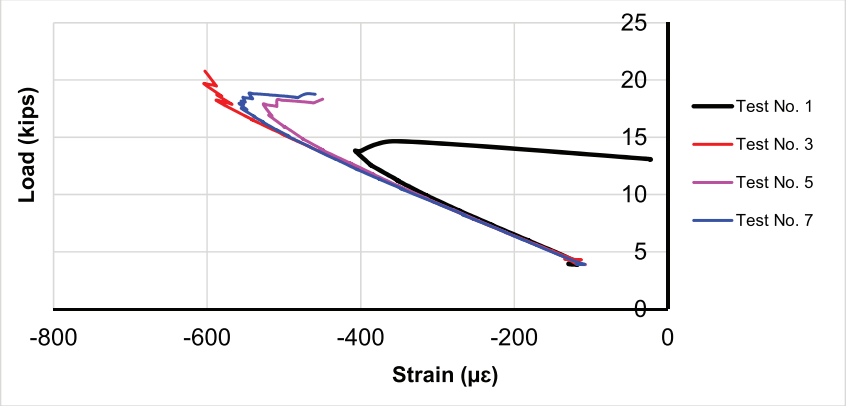

Fig. 16. Load-strain plots at Location 3 TN, Tests 1, 3, 5, and 7.

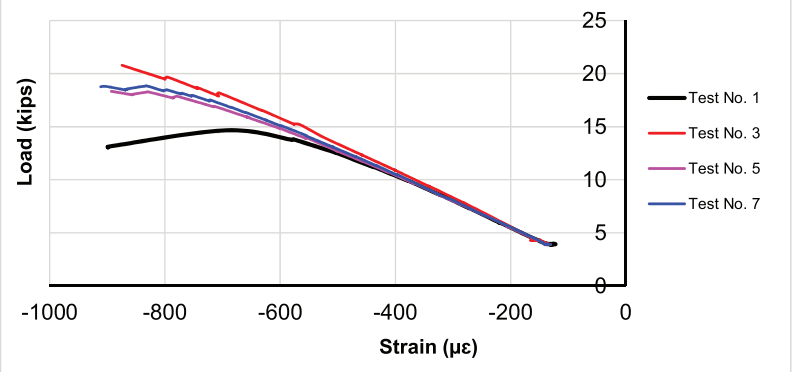

Fig. 17. Load-strain plots at Location 3 TS, Tests 1, 3, 5, and 7.

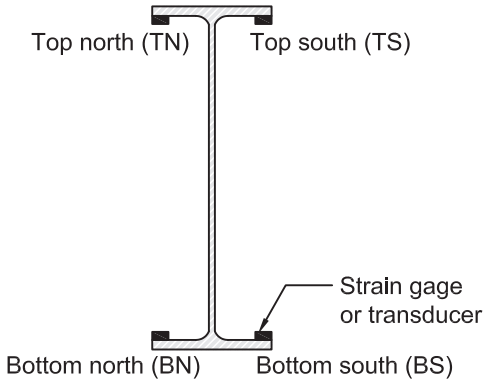

Fig. 18. Strain transducer locations.

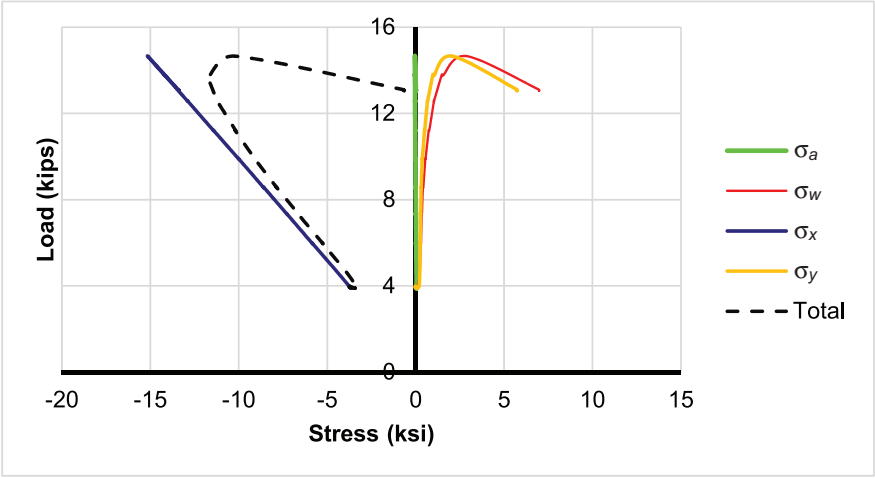

Fig. 19. Stress components, Location 3 TN, Test No. 1.

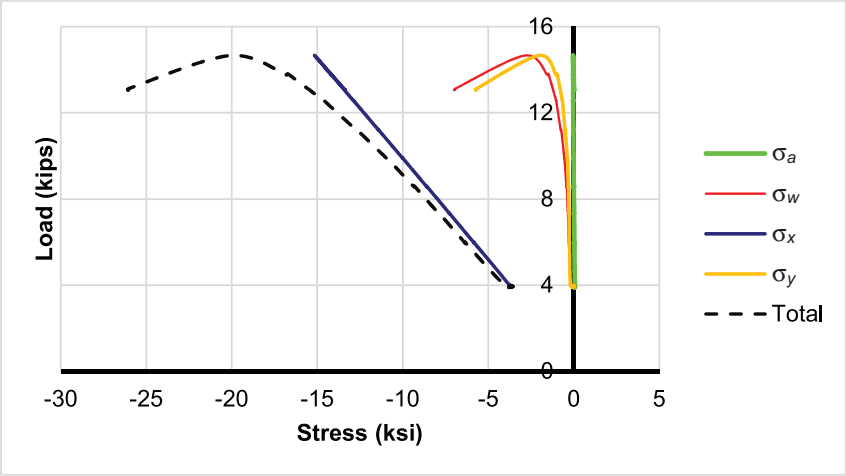

Fig. 20. Stress components, Location 3 TS, Test No. 1.

was not provided between adjacent stringers over the floor beam for Test 1 to 8. Those tests that included unbolted stringer bottom flanges helped evaluate LTB resistance for situations where the unbraced length did not explicitly meet the formal definition for unbraced length in LTB equations used in current codes and specifications. It was observed that stringer compression flanges at both supports should be laterally braced.

Group II Test Results—Intermediately Braced by Diaphragms

Intermediate steel diaphragms were installed at various locations for Group II tests to determine their effect on LTB. Rigid interior supports were provided, and stringer bottom flanges were either unbolted or bolted at the floor beam using ⅞-in.-diameter high-strength bolts. The interior stringer was loaded at midspan of one or both spans. The unbraced lengths varied from 12 to 24 ft. The longer unbraced lengths corresponded to reduced buckling loads, as expected. The connection types (e.g., bolted or unbolted connections) at the stringer bottom flange affected the buckling load, with unbolted connections generally resulted in a slightly lower buckling load. Refer to Sun et al. (2021) for more detailed discussion of these tests.

Group III Test Results—Intermediate Bracing Using Timber Ties

As indicated in Table 1, Group III tests were of stringers braced using 4 in. × 4 in. timber ties, which were affixed to the stringer top flanges using C-clamps. As stated earlier,

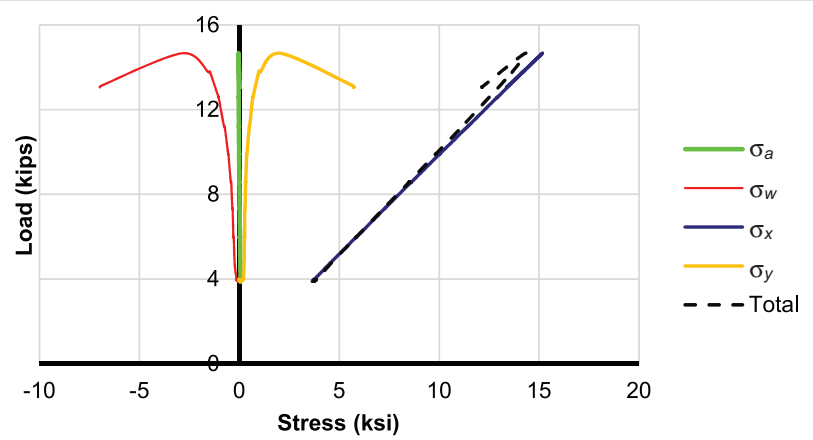

Fig. 21. Stress components, Location 3 BN, Test No. 1.

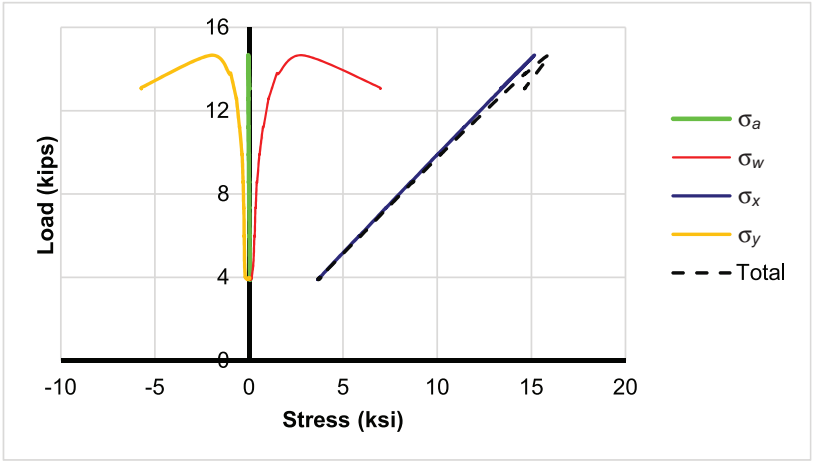

Fig. 22. Stress components, Location 3 BS, Test No. 1.

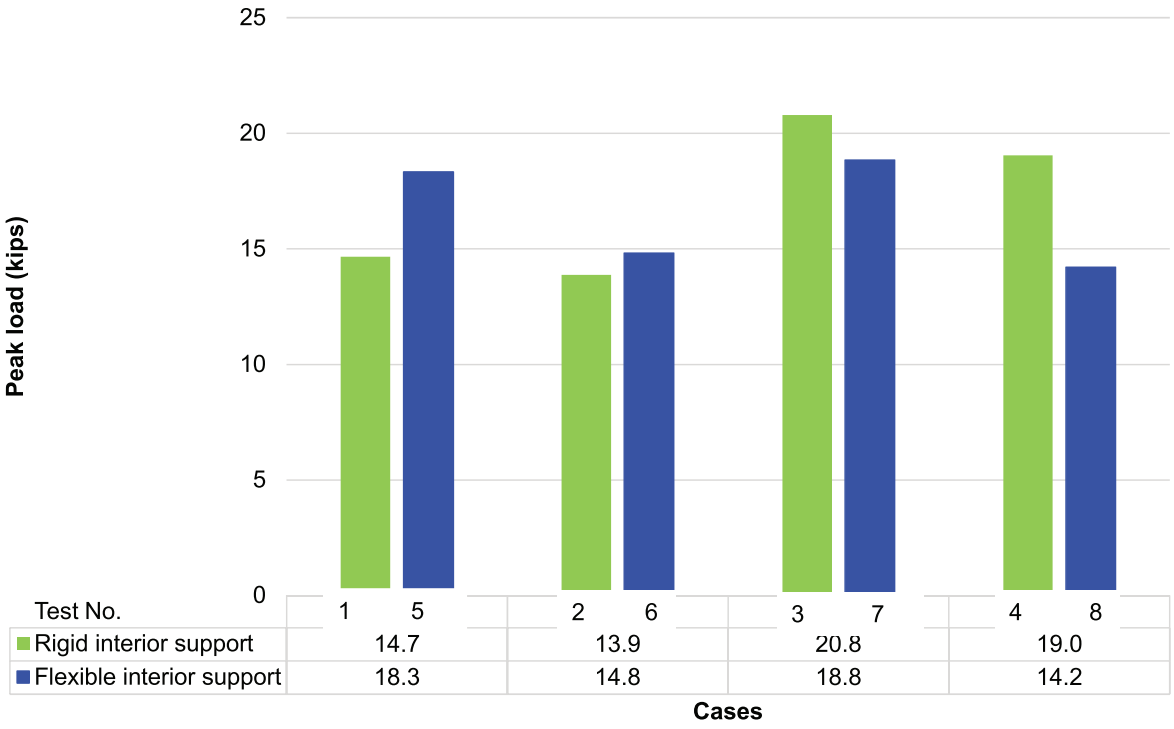

Fig. 23. Effect of floor beam relative stiffness on loading capacity.

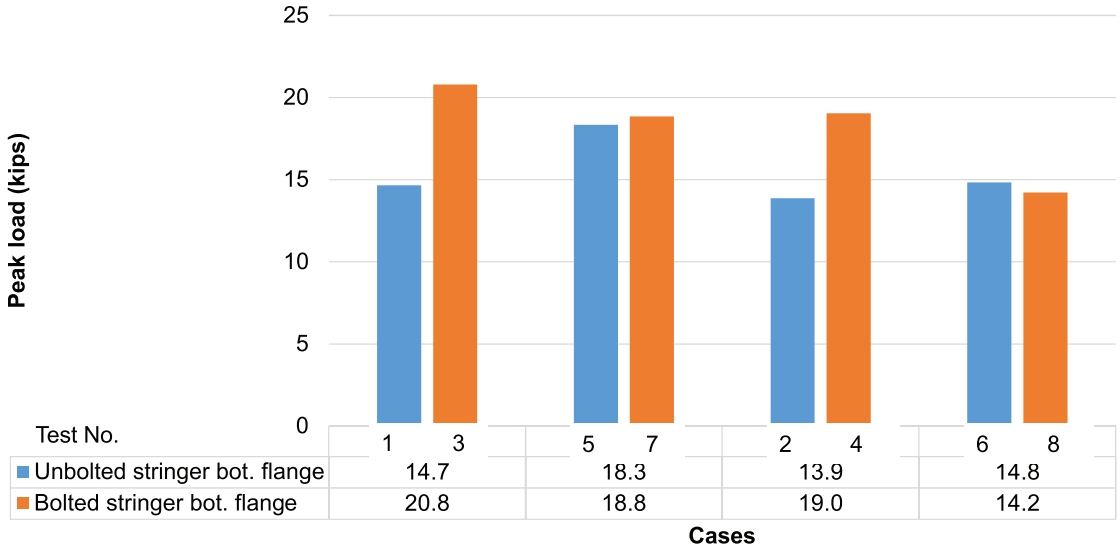

Fig. 24. Effect of stringer to floor beam fixity on loading capacity.

these tests were completed to demonstrate that a small increase in bracing, even with low strength, can significantly change LTB behavior. Table 4 provides descriptions of Tests 2 and 29 to 32, which were subjected to concentrated loads at midspan of both spans. Figure 25 plots load versus lateral deflection, and Figure 26 plots load versus strain at Location 3 TN. Beneficial effects provided by minimal lateral bracing, ones that increase LTB resistance, are clearly demonstrated via placement of a pair of timber ties at midspan (Test No. 29), which nearly doubled the capacity compared to the baseline unbraced test (Test No. 2). Midspan bracing was also more effective than bracing using ties spaced at $L/3$ (Test No. 30). Bracing effects for ties spaced at $L/4$ and $L/5$ (Tests 31 and 32) were nearly identical and only nominally improved capacity over that observed for Test No. 29. These findings were generally consistent with those from full-scale tests of a timber deck conducted by Webb and Yura (1992), in which the friction between the deck and stringer was shown to increase strength. A full-size test on a five-beam, short, single-span bridge conducted by Vegesna and Yura (1992) also showed that timber decks not positively attached to supporting stringers doubled stringer LTB resistance.

The level of lateral restraint provided by minimal placement of timber ties [i.e., small bracing stiffness and connection strength (C-clamps)] was further evaluated for several tests having either rigid or flexible interior supports. Results are shown in Figures 27 and 28. These figures plot peak loads as a function of tie spacing and compare them to baseline tests (e.g., Tests 2, 4, 6, and 8) where no ties

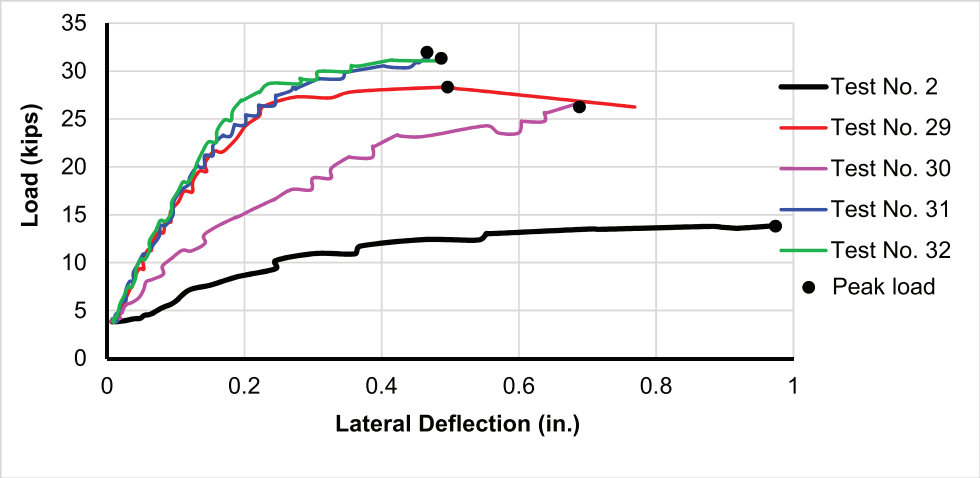

Fig. 25. Load versus lateral deflections, Tests 2 and 29 to 32.

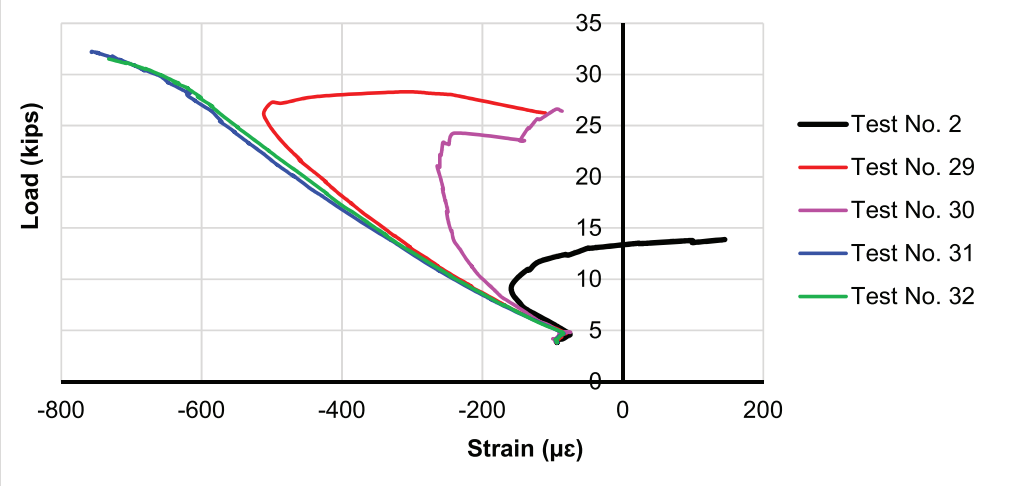

Fig. 26. Load-strain plots at Location 3 TN, Tests 2 and 29 to 32.

Table 4. Descriptions of Tests 2 and 29 to 32, Both Spans Loaded				
	Boundary Conditions			
Test No.	Floor Beam Relative Stiffness	Stringer Top Flange Bracing		Stringer Bottom Flange to Floor Beam Connection
2	Rigid	Unbraced		Unbolted to floor beam
29	Rigid	Timber ties (4 in. × 4 in.), connected using C-clamps	Spaced at $L/2$	Unbolted to floor beam
30			Spaced at $L/3$	
31			Spaced at $L/4$	
32			Spaced at $L/5$	

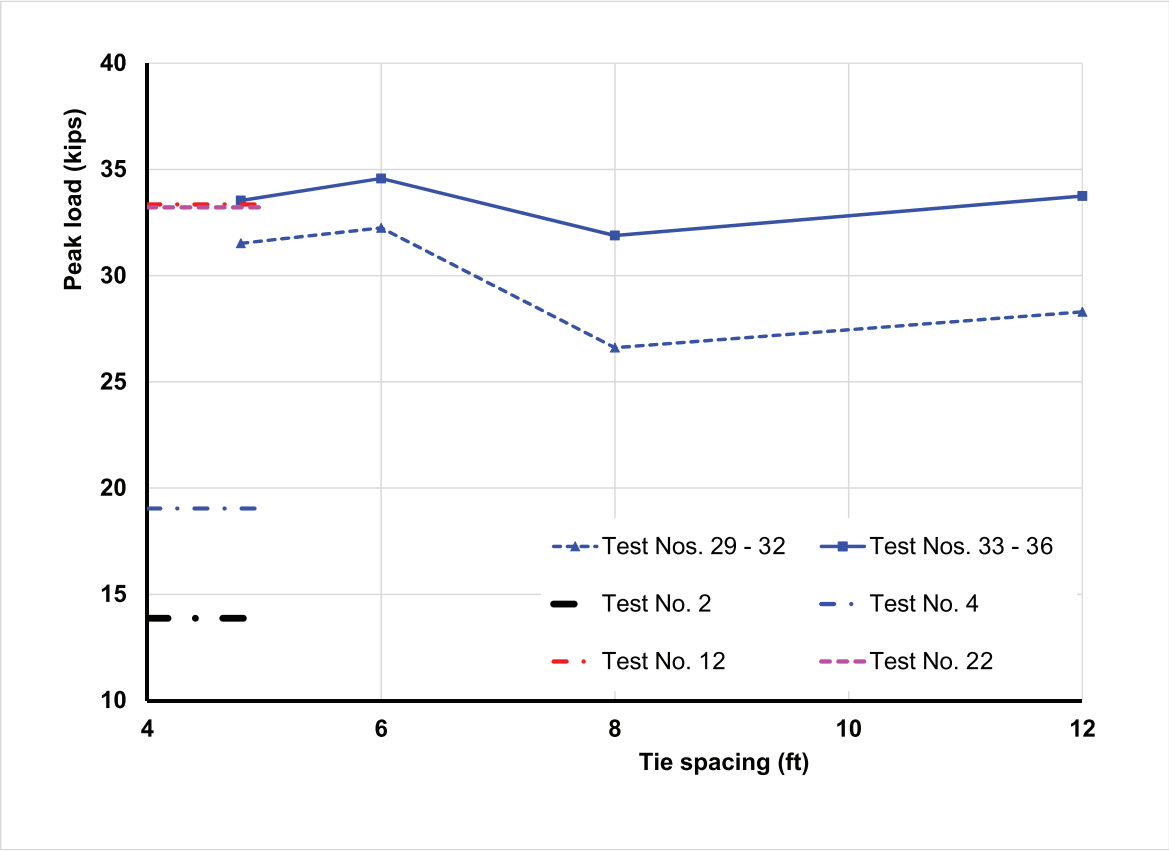

Fig. 27. Timber tie bracing effects, rigid interior support.

were provided. Figure 27 also shows peak loads for Tests 12 and 22, which had steel diagrams installed at midspan. The bracing effect provided by the timber ties at spacings of Span/4 and Span/5 was comparable to that of the steel diaphragms at midspan. Group III tests show that LTB resistance can be increased significantly using minimal lateral stiffness provided by C-clamped 4 in. × 4 in. timber ties and lend credence to potential LTB resistance noncomposite decks can provide.

CONCLUSIONS

An experimental study was completed to examine LTB resistance of continuous stringers. The assembly was designed to represent floor systems in twin girder or truss bridges in Louisiana and was subjected to loads that represented design tandems or design trucks. The study outlined herein was part of a larger study that included a noncomposite, cast-in-place concrete deck. It included extensive tests of a two-span test assembly containing three stringer lines and a supporting floor beam. A variety of unbraced lengths and stiffness were investigated along with flexible and rigid interior supports, and bolted and unbolted connections between the stringer bottom flange and interior supporting floor beam. Both steel diaphragms and timber ties acted as bracing members. Results provided a robust database for evaluation of continuous beam LTB resistance. The following conclusions were drawn:

1. A flexible interior support (i.e., floor beam) largely produced LTB resistances that differed by 25% from rigid interior support cases.
2. LTB commonly occurred at higher applied loads when the stringer bottom flange was bolted to its supporting floor beam.
3. Minimal lateral bracing stiffness provided by 4 in. by 4 in. timber ties and C-clamps provided benefit to stringer LTB resistance, with capacities nearly doubling compared to baseline, unbraced tests. These results appear to justify higher LTB resistances than what are typically used for noncomposite concrete decks.

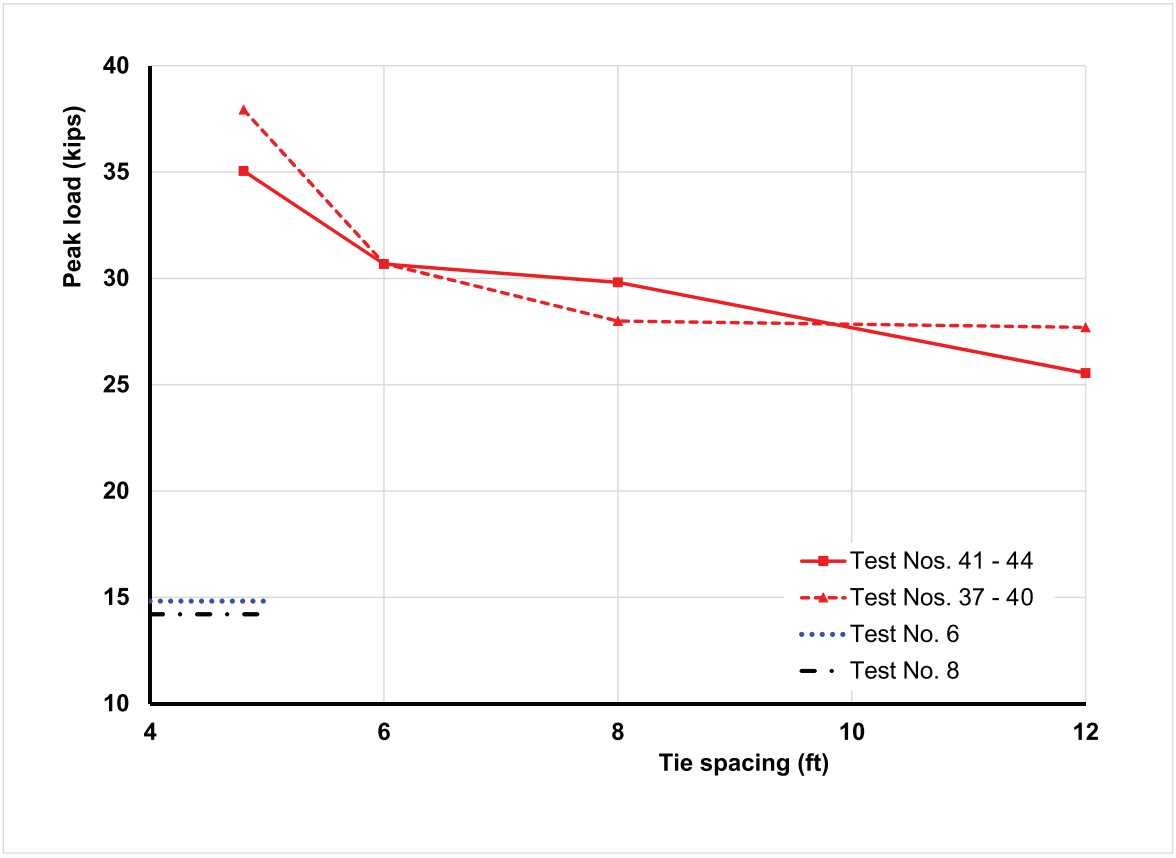

Fig. 28. Timber tie bracing effects, flexible interior support.

ACKNOWLEDGMENTS

The authors would like to thank the LTRC and the LA DOTD for funding this project. The authors are grateful to the Project Review Committee Members, including Art Aguirre, Alden Allen, Michael Boudreaux, Mark Bucci, Nick Fagerburg, Dana Feng, Kelly Kemp, William Metcalf, and Kian Yap, for their guidance and support. Special thanks go to Walid R. Alaywan, Senior Structures Research Engineer at the LTRC, for leading and managing this project. The authors are also grateful to Peter Hilsabeck for assisting in lab testing. The contents of this paper do not necessarily reflect the official views or policies of the LA DOTD and LTRC.

REFERENCES

AASHTO (2020), *AASHTO LRFD Bridge Design Specifications*, 9th Ed., American Association of State Highway and Transportation Officials, Washington, D.C.

Sun, C., Linzell, D., and Puckett, J. (2021), "Load Rating of Existing Continuous Stringers on Louisiana's Bridges," LTRC Project 18-4ST Report, Louisiana Transportation Research Center, Baton Rouge, La.

Sun, C., Linzell, D., Puckett, J., Akintunde, E., and Rageh, A. (2022), "Experimental Study of Continuous Beam Lateral Torsional Buckling Resistance with a Noncomposite Concrete Deck," *Journal of Structural Engineering*, Vol. 148, No. 4, 04022026.

Vegesna, S. and Yura, J.A. (1992), "An Ultimate Load Test to Study Bracing Effects of Bridge Decks," Report No. FHWA/TX-92+1239-2, Center for Transportation Research, University of Texas at Austin, Austin, Texas.

Webb, S.T. and Yura, J.A. (1992), "Evaluation of Bridge Decks as Lateral Bracing for Supporting Steel Stringers," Report No. FHWA/TX-92+1239-3, Center for Transportation Research, University of Texas at Austin, Austin, Texas.

Overstrength of I-Shaped Shear Links for EBF Design

Hyoung-Bo Sim, Xiao-Jun Fang, and Chia-Ming Uang

ABSTRACT

Past experimental research on EBF indicated that the link overstrength, particularly that for short (i.e., shear) links, could be much higher than that specified in the AISC Seismic Provisions, thus potentially leading to an unsafe design of beams, columns, and gusset connections per the capacity design requirements. This study aims to identify key factors contributing to the high overstrength and to derive an expression to predict the overstrength of short links. Available experimental data were first collected, and main parameters affecting the overstrength were identified from the database and used for a multi-variate regression analysis. It was found that the following two parameters affect the link overstrength the most: (1) the F_u/F_y ratio between the actual tensile strength and yield stress and (2) K_w, a factor that represents the contribution of localized bending of link flanges. The link length, to a lesser extent, also affects the overstrength. A predictive overstrength equation based on these three parameters was proposed for capacity design of EBF with short links.

KEYWORDS: eccentrically braced frames, cyclic tests, link overstrength, seismic design.

INTRODUCTION

Eccentrically braced frames (EBFs) combine the advantages of the high ductility of special moment frames and the high elastic lateral stiffness approaching that of concentrically braced frames (Roeder and Popov, 1978; Popov and Engelhardt, 1988; Bruneau et al., 2011). A typical EBF consists of links, braces, beams outside the links, columns, and connections. According to the AISC *Seismic Provisions*, ANSI/AISC 341 (AISC 2016, 2022a), hereafter referred to as AISC 341, links are designed to dissipate seismic energy, while structural components other than beams outside the link are designed to remain essentially elastic in a seismic event. (Because beams outside the link and the link itself are continuous and have the same section, it is difficult to keep the beams elastic without stiffening. Thus, AISC 341 allows these beams to experience limited flexural yielding.) Observed performance of actual EBF buildings in earthquakes is very limited in the United States. But experience from the 2010 and 2011 Christchurch, New Zealand, earthquakes did show good overall performance (Bruneau et al., 2010; Clifton et al., 2011).

Hyoung-Bo Sim, Associate Professor, Department of Civil and Environmental Engineering, In.eon National University, In.eon, South Korea. Email: hbsim@inu.ac.kr

Xiao-Jun Fang, Graduate Student Researcher, Department of Civil and Environmental Engineering, In.eon National University, In.eon, South Korea. Email: fangxiaojun@inu.ac.kr

Chia-Ming Uang, Professor, Department of Structural Engineering, University of California, San Diego, La Jolla, Calif. Email: cmu@ucsd.edu (corresponding)

Paper No. 2022-04

The link rotation angle, γ_p, defined as the inelastic (or plastic) angle between the link and the beam outside of the link, is used to describe the inelastic deformation capacity of a link. The rotation angle is a function of the link length, e, which in turn dictates if it will yield primarily in shear, flexure, or a combination of the two (Roeder and Popov, 1978; Malley and Popov, 1984; Kasai and Popov, 1986; Okazaki and Engelhardt, 2007). Define the normalized link length, ρ, as

$$\rho = \frac{e}{M_p/V_p} \tag{1}$$

where M_p is the plastic moment and V_p is the plastic shear strength. When $\rho \le 1.6$ (i.e., short or shear links), AISC 341 specifies that a properly stiffened shear-yielding link has a link rotation angle capacity of at least 0.08 rad.

For capacity design of diagonal braces and brace connections, beams outside the link, and columns, the nominal shear strength of a link needs to be adjusted to reflect two effects: (1) actual yield strength of the steel and (2) other factors, including strain hardening and flange contribution under cyclic loading. AISC 341 uses an adjustment factor R_y to account for the first effect. For shear-yielding links, the second effect is quantified by defining an overstrength factor, Ω_l, in this study:

$$\Omega_l = \frac{V_u}{V_{pa}} \tag{2}$$

where V_u represents the maximum shear strength measured in experimental testing (which is equivalent to the required shear strength in design) and V_{pa} is the plastic shear strength:

$$V_{pa} = 0.6F_{ya}(d - 2t_f)t_w \tag{3}$$

In Equation 3, d, t_f, and t_w are the overall depth, flange thickness, and web thickness, respectively, and F_{ya} is the measured yield stress of the web. To avoid confusion, F_y and F_u refer to the minimum specified yield stress and tensile strength, respectively, in AISC 341, while the measured (or actual) yield stress and tensile strength are referred to as F_{ya} and F_{ua} in this study. If F_y were used in Equation 3, the computed Ω_l value from Equation 2 would include both effects mentioned earlier. Because this study investigates the second effect (i.e., link overstrength), the measured yield stress, F_{ya}, from tensile coupon testing is used in Equation 3.

Based on test results of rolled wide-flange links of ASTM A36 steel in the 1980s, an overstrength factor of 1.5 for strain hardening was recommended (Popov and Engelhardt, 1988). Testing that was conducted after the 1994 Northridge, California, earthquake on rolled wide-flange links of ASTM A992 steel showed that the overstrength factor ranges from 1.05 to 1.62, with an overall average of 1.35 (Okazaki and Engelhardt, 2007). For short links dominated by shear yielding, the overstrength tends to be somewhat higher (1.25 to 1.62, with an average of 1.41). Note that all ASTM A36 or A992 steel links tested were rolled wide-flange shapes, and member sizes were small and not heavy; for example, W10×19, W10×33, W16×36, and W18×40 of ASTM A992 steel were tested by Okazaki and Engelhardt (2007).

To achieve an economical EBF design, AISC 341 has been specifying a lower overstrength factor (1.25) for I-shaped links for capacity design of columns, diagonal braces, and their connections. That is, the required seismic forces for these components are based on the assumption that the member forces at the ends of the link correspond to a link shear of 1.25 times the expected shear strength, R_yV_n. According to the Commentary in the 1997 edition of the AISC *Seismic Provisions*, this lower value was justified on the basis that, for brace design, the nominal yield strength and a resistance factor are used in sizing the braces; assuming that R_y is equal to 1.1 and the resistance factor is 0.9, the effective overstrength of the link is $1.25 \times 1.1/0.9 = 1.53$. The link overstrength factor is further relaxed from 1.25 to 1.1 for the design of beams outside the link because (1) beam strength will be enhanced by the presence of a composite slab, and (2) limited yielding in the beams is judged to be non-detrimental to the EBF performance (Commentary to AISC 341, 2016).

The discussion on link overstrength presented earlier applies to hot-rolled W-shape links. For I-shaped built-up links, however, available experimental data indicated that the overstrength factor can be significantly higher than that specified in AISC 341. For example, McDaniel et al. (2003) conducted cyclic tests of two large-size built-up shear links of ASTM A709 Gr. 50 steel to evaluate the link performance for bridge applications; the reported values of the overstrength factor were 1.83 and 1.94, respectively. Itani et al. (2003) reported that the overstrength factor was about 1.80 based on cyclic testing of two built-up links of A709 Gr. 50 steel. Based on finite element simulation, Barecchia et al. (2006) proposed a formula to evaluate the overstrength factor of short and intermediate links with European hot-rolled shapes. The study found that the overstrength factor would increase with a reduced ρ and an increased b_f/d ratio, where b_f is the flange width. Ji et al. (2016) tested very short hybrid steel links, where the yield stresses of the web (33 to 41 ksi) are lower than that of the flanges, and the overstrength factor reached 1.9. The authors attributed this large overstrength to the contribution of link flanges and cyclic hardening of the web steel. Two large-size built-up shear links with ASTM A709 Gr. 50 steel were tested for building construction and, again, large overstrength was observed (Sim and Uang, 2011; Gulec et al., 2012).

Based on Richards and Uang (2006), the AISC 341 Commentary (AISC, 2016) states that designers should consider a high overstrength factor for large built-up links with very thick flanges and very short lengths ($e < M_p/V_p$ or $\rho < 1.0$). Azad and Topkaya (2017) provided a summary of past research, both analytical and experimental, on the overstrength factor of links and found it inconclusive that thick flanges are the main contributing factor for very high overstrength.

OBJECTIVE AND SCOPE

There is no consensus on the cause and main contributing factors for the "unusual" high overstrength observed from testing of some short links. Because this would potentially produce an unsafe capacity design and AISC 341 does not provide any design guidelines, the goal of this study is to identify key contributing factors and to derive an expression to predict the overstrength of short links.

EXPERIMENTAL DATABASE

The following criteria were used to establish the experimental database (see Table 1). First, only short links were selected because links that showed large overstrength in testing were classified per AISC 341 as short links. Therefore, only data with ρ no greater than 1.6 were considered. Table 1 shows that most of the specimens collected had ρ less than 1.1. Second, links with both rolled wide-flange and built-up I-shape sections were included. Third, only specimens that were tested after the 1994 Northridge, California, earthquake were considered because 36 ksi steel is much less likely to be used for new construction in the future. For rolled shapes, therefore, it means that only A992 steel was considered, and A36 steel was excluded in the

Table 1. Test Matrix for Regression Analysis of Link Overstrength Factors

Group No.	Steel Grade	Section	Specimen Designation	ρ	F_{ya} (ksi)		F_{ua} (ksi)		$b_f/2t_f$	h/t_w	t_f/t_w	A_f/A_w	b_f/d	K_w	Ω_l[a]	Ω_l[b]
					Web	Flange	Web	Flange								
1 Okazaki and Engelhardt (2007)	A992	W10×33	4A-RLP	1.04	51.6	55.4	73.5	73.0	9.2	28.4	1.50	1.23	0.82	0.070	1.45	1.32
		W18×40	12-RLP	1.02	51.1	57.0	72.4	76.4	6.1	54.0	1.67	0.56	0.34	0.038	1.44	1.36
		W16×36	8-RLP	1.49	52.5	56.9	77.5	81.9	7.1	48.0	1.46	0.64	0.44	0.023	1.37	1.30
		W10×68	10-RLP	1.25	46.3	58.6	69.5	77.0	6.6	17.8	1.64	1.59	0.97	0.100	1.47	1.25
		W10×33(B)	S9	0.99	55.0	58.3	75.1	76.9	9.2	28.4	1.50	1.23	0.82	0.070	1.43	1.30
2 Mansour et al. (2011)	A992	W14×68	UT-3A	1.16	55.1	64.5	72.7	80.0	7.0	28.6	1.73	1.24	0.71	0.076	1.41	1.27
		W14×68	UT-3B	1.16	55.1	64.5	72.7	80.0	7.0	28.6	1.73	1.24	0.71	0.076	1.42	1.28
3 Dusicka et al. (2010)	A709 Gr. 50	Built-up I-section	C345	0.83	56.6	54	78.7	73.9	6.8	31.0	1.57	0.99	0.63	0.078	1.90	1.72
4 Itani et al. (2003)	A709 Gr. 50	Built-up I-section	BU16	1.31	54.0	57.0	84.0	81.0	4.7	34.7	4.00	3.50	0.88	0.109	1.82	1.48
			BU30	1.31	54.0	57.0	84.0	81.0	4.7	54.0	3.00	1.40	0.47	0.044	1.79	1.61
5 McDaniel et al. (2003)	A709 Gr. 50	Built-up I-section	TYPE 1	0.82	53.4	51.3	77.2	72.1	6.7	30.8	1.61	1.02	0.63	0.082	1.83	1.66
			TYPE 3	0.58	53.4	51.3	77.2	72.1	6.7	30.8	1.61	0.80	0.50	0.108	1.94	1.76
6 Gulec et al. (2012)	A709 Gr. 50	Built-up I-section	Spec. 1	1.11	53.0	53.0	78.3	81.9	6.2	35.5	2.25	1.58	0.70	0.076	1.77	1.57
			Spec. 2	1.11	53.8	53.0	82.7	81.9	6.2	35.5	2.25	1.58	0.70	0.076	1.87	1.66
7 Chi and Uang (2000)	A572 Gr. 50	Built-up I-section	SDE-1	0.64	57.1	58.4	87.3	79.5	4.4	50.0	3.00	1.43	0.48	0.124	1.75	1.58
			SDE-2	0.64	57.1	58.4	87.3	79.5	4.4	50.0	3.00	1.43	0.48	0.098	1.71	1.55
			SDE-3	0.86	57.0	58.4	88.5	79.5	6.9	50.7	2.67	1.27	0.48	0.081	1.65	1.49

[a] based on $V_p = 0.6F_{ya}(d–2tf)t_w$
[b] based on $V_p = 0.6F_{ya}dt_w$

study. (Rolled wide-flange shapes of A36 steel are practically unavailable in the United States after the Northridge earthquake.) For built-up links, only A572 Gr. 50 steel and A709 Gr. 50 steel were considered. Note in Table 1 that h for computing h/t_w is defined in AISC 341: (1) the clear distance between flanges less the fillet or corner radius for rolled shapes or (2) the clear distance between flanges for welded built-up sections.

Okazaki and Engelhardt (2007) reported test results of 37 link specimens of A992 steel with five different W-shapes and varying lengths. One objective of the study was to investigate the effect of using different test loading protocols. Group 1 in Table 1 contains five short specimens with $\rho < 1.5$ that were tested with the loading protocol consistent with that specified in the 2016 edition of AISC 341. (The majority of the specimens were tested with more severe loading sequences, which would potentially affect the failure mode and the associated overstrength, and thus they were excluded from the database.)

Group 2 includes 2 of 13 specimens reported by Mansour et al. (2011) in a study to develop replaceable links. Nine specimens that were excluded from the database were composed of back-to-back double channels that were bolted at both ends. The remaining four specimens used W-shape links with welded end plates at both ends. But tensile coupon tests were not conducted on two specimens, and therefore, they were excluded from the database because the actual overstrength could not be calculated.

Group 3 contains one of five specimens reported by Dusicka et al. (2010); three specimens that were excluded explored the potential of using low-yield steel and without intermediate stiffeners. A709 steel was specified for the remaining two specimens, one with Gr. 50 and another with Gr. 70 steel. Because the minimum specified yield stress of Gr. 70 steel violates the maximum value permitted in AISC 341, only one specimen (C345) was included in the database.

Group 4 includes two links reported by Itani et al. (2003). These two built-up links used A709 Gr. 50 steel. Relative to the web thickness, the flanges were the thickest among all specimens in the database ($t_f/t_w = 4.0$ and 3.0, respectively).

Group 5 consists of two large-size built-up links (depth = 37.4 in.) with A709 Gr. 50 steel (McDaniel et al., 2003). The t_f/t_w ratio (= 1.61) falls in the normal range of rolled shapes (e.g., see Group 1). Group 6 also includes two large-size links (depth = 40 in.) with the same grade of steel (Gulec et al., 2012). But the t_f/t_w ratio (= 2.25) is higher.

Three link specimens in Group 7 were tested to verify the cyclic performance of a coupled moment-resisting frame system, where vertical links were installed between two girders in a frame (Chi and Uang, 2000). A572 Gr. 50 steel was specified for the built-up links. The t_f/t_w ratio varies from 2.67 to 3.0.

Figure 1 shows the distribution of the link overstrength, Ω_l, with respect to the normalized link length, ρ. The data is scattered within the range considered ($\rho \leq 1.6$). But a trend does indicate that the link overstrength increases when ρ is reduced. Data points with rolled-shape links are circled; they show a lower overstrength ($\Omega_l < 1.6$). Figure 2 shows similar plots with respect to the width-to-thickness ratios of the flanges and web. No clear trend can be observed between Ω_l and these two width-thickness ratios.

AISC 341 Commentary (AISC, 2016) provides a reminder to the designers that a much higher overstrength may exist in built-up links with very thick flanges and very short lengths ($\rho < 1.0$). To examine this effect, Figure 3 shows the distribution of Ω_l with respect to two parameters: the ratio between the flange thickness and web thickness, t_f/t_w, and the ratio between the flange area and web area, with the latter being computed as $(d - 2t_f)t_w$. Contrary to that described in AISC 341, Figure 3 does not support the claim that thicker flange or larger flange area would necessarily produce a high overstrength factor.

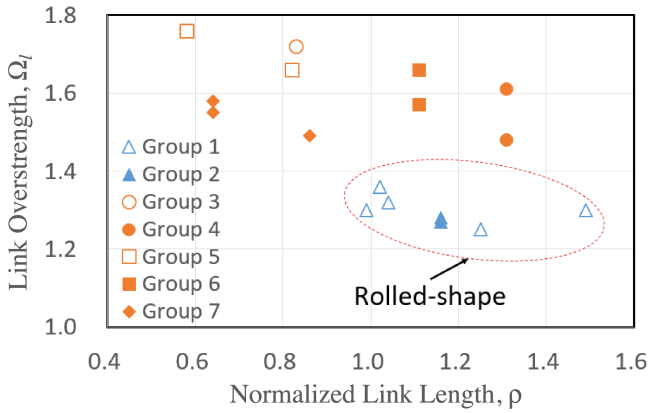

Fig. 1. Distribution of Ω_l with respect to ρ.

A shear link under large inelastic deformations will cause flanges to kink at both ends of the link, a behavior that is analogous to the panel zone shear deformation in special moment frames. AISC *Specification*, ANSI/AISC 360 (AISC, 2022b), hereafter referred to as AISC 360, Section J10.6 provides an equation to compute the nominal shear strength of the panel zone in a beam-to-column moment connection. The equation is written in a slightly different form:

$$V_n = 0.60 F_y d_c t_w (1 + K_w) \tag{4}$$

where

$$K_w = \frac{3 b_{cf} t_{cf}^2}{d_b d_c t_w} \tag{5}$$

The K_w factor represents the contribution from localized bending (i.e., kinking) of the column flanges when the shear deformation reaches four times the shear yield strain of the panel zone. Because both panel zones in a special moment frame and shear links in an EBF undergo large shear deformations, it was speculated that the link overstrength may also be related to K_w. When applying Equations 4 and 5 to the link, d_c, b_{cf}, t_{cf}, t_w, and d_b are the depth, flange width, flange thickness, web thickness, and length of the link, respectively. Note that K_w can be rewritten as

$$K_w = \frac{12 Z_f}{v_w} \tag{6}$$

where Z_f is the plastic section modulus of one flange,

$$Z_f = \frac{b_f t_f^2}{4} \tag{7a}$$

and v_w is the overall volume of the link web,

$$v_w = e d_c t_w \tag{7b}$$

Equations 6 and 7 show that not only a larger flange, but also a reduced web area, $d_c t_w$, and a shorter link length, e, will increase the value of K_w. Figure 4 shows the distribution

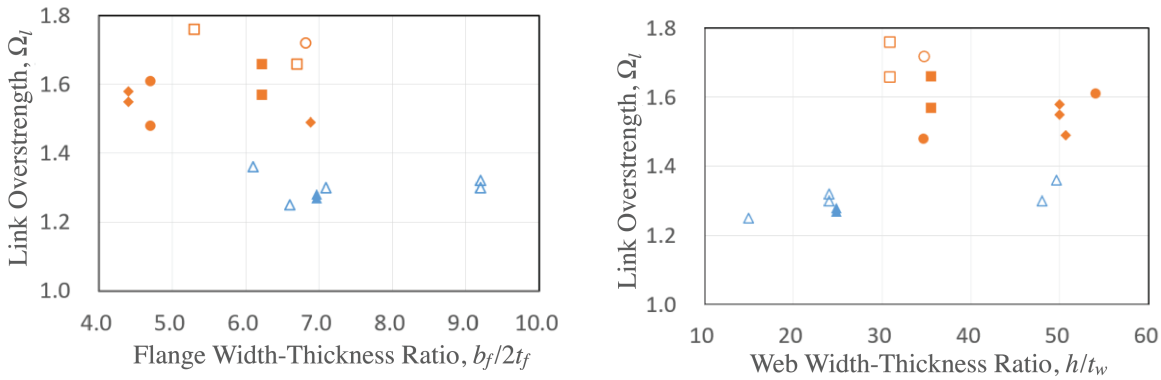

(a) Flange *(b) Web*

Fig. 2. Distribution of Ω_l with respect to section width-thickness ratios.

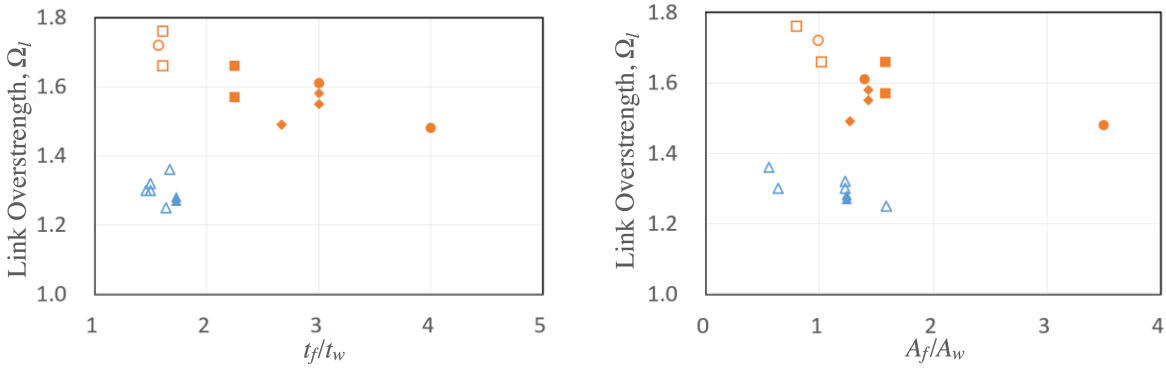

(a) Thickness ratio *(b) Area ratio*

Fig. 3. Distribution of Ω_l with respect to flange-to-web thickness and area ratios.

of the test data in the $(1 + K_w)$ versus Ω_l domain. Although the data is scattered, it appears to show that a larger contribution of the flanges due to kinking tends to produce a higher link overstrength. For the data collected, the figure also shows that built-up links tend to have a larger $(1 + K_w)$ value.

Figure 5 uses the F_{ua}/F_{ya} ratio of the web for the plot, where F_{ya} and F_{ua} are the measured yield stress and tensile strength, respectively. Unlike all the previous parameters examined, this material strength ratio does show a stronger correlation with the link overstrength. This figure also shows that built-up links in the database have higher F_{ua}/F_{ya} ratios than those of rolled-shape links.

As mentioned in the literature review, finite element simulation by Barecchia et al. (2006) indicated that the overstrength factor would increase with an increase of the b_f/d ratio. Figure 6 shows the distribution of the link overstrength with respect to b_f/d. No clear trend can be observed. The observations from figures presented earlier are then used to guide the regression analysis.

REGRESSION ANALYSIS

Parameters listed in Table 1 were considered in a multivariate regression analysis to establish an expression for predicting the link overstrength, Ω_l. A sensitivity study showed that F_{ua}/F_{ya} of the web and $(1 + K_w)$ have the most significant influence. Note that Ω_l is based on the measured yield stress of the web (see Equation 3), yet $(1 + K_w)$ measures the increase of link shear strength due to the contribution from flanges. The $(1 + K_w)$ term needs to be adjusted to $(1 + K_w)(F_{yfa}/F_{ywa})$ in regression to account for the difference of measured yield stresses between the web and flanges.

A regression results in the following expression with a coefficient of determination, R^2, of 0.781:

$$\Omega_l = 1.402\left[(1+K_w)\frac{F_{yfa}}{F_{ywa}}\right]^{1.144}\left(\frac{F_{ua}}{F_{ya}}\right)^{0.414} \quad (8)$$

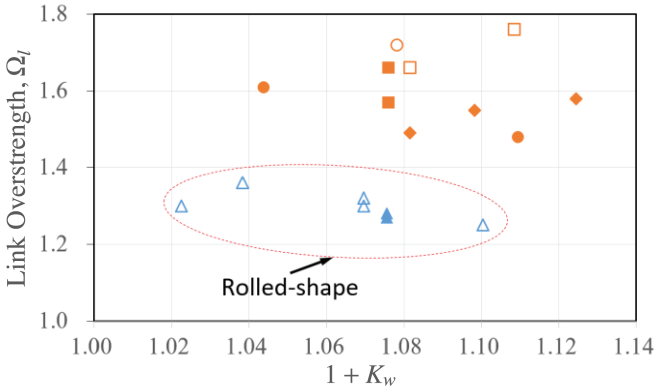

Fig. 4. Distribution of Ω_l with respect to $(1 + K_w)$.

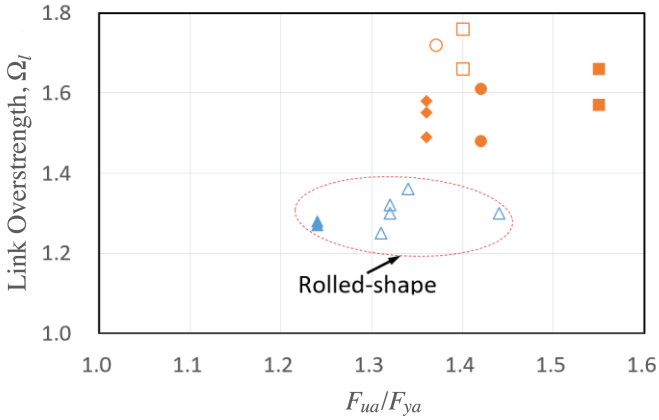

Fig. 5. Distribution of Ω_l with respect to web F_{ua}/F_{ya} ratio.

Table 2. Components of Ω_l					
Group No.	Specimen Designation	$(1+K_w)\frac{F_{yfa}}{F_{ywa}}$	$\left(\frac{F_{ua}}{F_{ya}}\right)^{0.5}$	Ω_l	
				Equation 9	Test
1 Okazaki and Engelhardt (2007)	4A-RLP	1.00	1.15	1.57	1.45
	12-RLP	0.93	1.16	1.47	1.44
	8-RLP	0.94	1.20	1.55	1.37
	10-RLP	0.87	1.15	1.36	1.47
	S9	1.01	1.15	1.59	1.43
2 Mansour et al. (2011)	UT-3A	0.92	1.11	1.40	1.41
	UT-3B	0.92	1.11	1.40	1.42
3 Dusicka et al. (2010)	C345	1.13	1.17	1.81	1.90
4 Itani et al. (2003)	BU16	1.05	1.19	1.71	1.82
	BU30	0.99	1.19	1.61	1.79
5 McDaniel et al. (2003)	TYPE 1	1.12	1.18	1.82	1.83
	TYPE 3	1.15	1.18	1.86	1.94
6 Gulec et al. (2012)	SPEC. 1	1.08	1.24	1.83	1.77
	SPEC. 2	1.09	1.24	1.86	1.87
7 Chi and Uang (2000)	SDE-1	1.10	1.17	1.76	1.75
	SDE-2	1.07	1.17	1.72	1.71
	SDE-3	1.06	1.17	1.69	1.65

Table 2 lists the contribution of each of the last two terms on the right-hand side of Equation 8. Taking Specimen TYPE 3, for example, which is a large-size, full-scale built-up specimen with an overall link depth of 37.4 in. and \a larger overstrength (1.94) from testing, each of these two terms (1.15 vs. 1.18) contribute comparably to the overstrength. Specimen SPEC. 2, which is another large-size, full-scale built-up specimen with an overall link depth of 40 in. and a flange thickness of 2¼ in., has a larger contribution (1.24) from the F_{ua}/F_{ya} term, and the contribution from flange kinking is less (1.09). The small-size rolled-shape W16×36 link specimen 8-RLP also shows a large

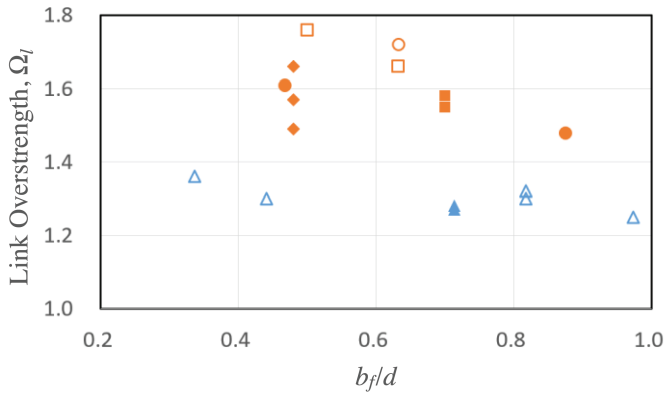

Fig. 6. Distribution of Ω_l with respect to b_f/d ratio.

contribution (1.20) from the F_{ua}/F_{ya} term, but the contribution from the flange kinking is small (0.94), resulting in a smaller overall link overstrength. (The reason for a value of 0.94, which is smaller than 1.0, is because the measured yield stress of the flanges is smaller than that for the web.)

Equation 8 can be adjusted by rounding the exponents as follows ($R^2 = 0.775$):

$$\Omega_l = 1.37\left[(1+K_w)\frac{F_{yfa}}{F_{ywa}}\right]\left(\frac{F_{ua}}{F_{ya}}\right)^{0.5} \tag{9}$$

A comparison of the experimental and predicted overstrengths based on Equation 9 is shown in Figure 7(a). For code implementation in AISC 341, F_{ya} and F_{ua} for the web in Equation 9 can be replaced by R_yF_y and R_tF_u. Assuming that, for design, the expected yield stresses of the flange and webs are the same, Equation 9 becomes

$$\Omega_l = 1.37(1+K_w)\sqrt{\frac{R_tF_u}{R_yF_y}} \tag{10}$$

where K_w is calculated using Equation 6, and F_y and F_u are the specified minimum yield and tensile strength of the web, respectively.

The Ω_l expressions presented here are the link overstrength normalized by using the plastic shear strength defined in Equation 3; this strength is based on a web area of $(d - 2t_f)t_w$ as defined in AISC 341. Because a web area of dt_w is used in AICS 360 (AISC, 2022b) instead, it is worthwhile to examine if using the following plastic shear strength to define the link overstrength would reduce the scatter of the data:

$$V_{pa} = 0.6F_{ya}dt_w \tag{11}$$

Another regression results in the following with $R^2 = 0.826$:

$$\Omega_l = 1.3\left[(1+K_w)\frac{F_{yfa}}{F_{ywa}}\right]^{1.165}\left(\frac{F_{ua}}{F_{ya}}\right)^{0.314} \tag{12}$$

Note that using Equation 11 to compute the link overstrength does reduce the scatter of the data somewhat. After simplification, the following expression can be used ($R^2 = 0.814$):

$$\Omega_l = 1.23\left[(1+K_w)\frac{F_{yfa}}{F_{ywa}}\right]\left(\frac{F_{ua}}{F_{ya}}\right)^{0.5} \tag{13}$$

Figure 7(b) shows the correlation with the test data. From Equation 13, the form suitable for design is:

$$\Omega_l = 1.23(1+K_w)\sqrt{\frac{R_tF_u}{R_yF_y}} \tag{14}$$

SUMMARY AND CONCLUSIONS

Eccentrically braced frames with short (or shear) I-shaped links are expected to perform better in a seismic event due to their high ductility capacity. But testing of short links in the past two decades showed that some links—especially those with built-up sections—exhibited a shear overstrength close to 2.0, significantly larger than the 1.5 observed in testing of rolled-shape links. For capacity design, such unusually

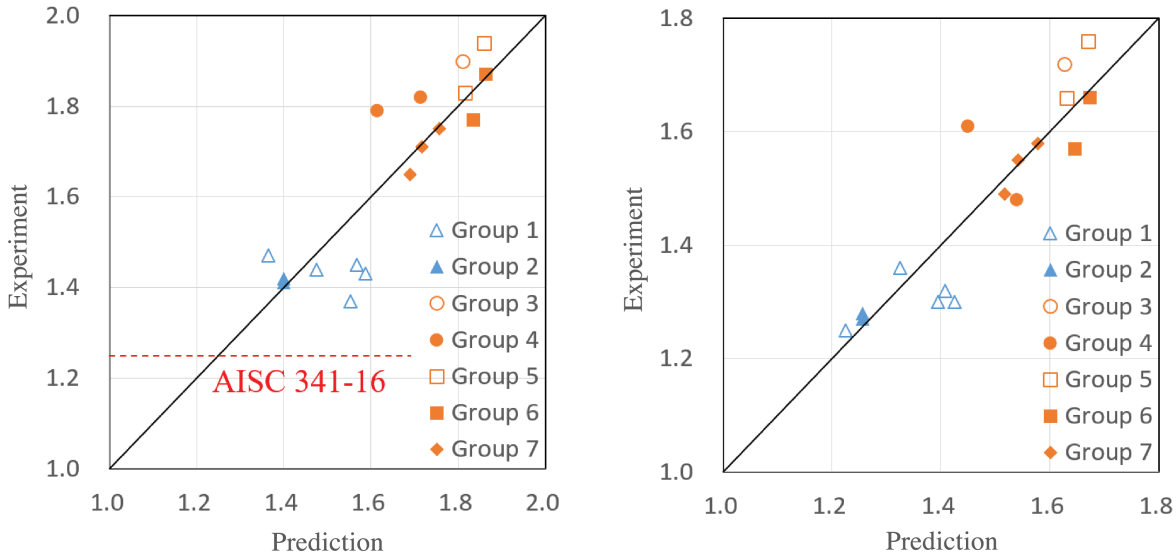

(a) Based on Equation 9 *(b) Based on Equation 13*

Fig. 7. Comparison of predicted and experimental overstrength factor.

high overstrength is also much larger than (1) the 1.25 factor for design of braces, columns, and gusset connections and (2) the 1.1 factor for design of beams outside the links stipulated in AISC 341, thus potentially leading to a mode of behavior inconsistent with the basis of EBF design. Although attempts have been made by some researchers in the past, no consensus could be reached on the main causes for the much higher overstrength. AISC 341 Commentary reminds designers to consider a high overstrength factor for large built-up links with very thick flanges and very short links. Still, no specific design guidance is provided.

This study addresses shear links only. An available experimental database for short links with both rolled and built-up sections and with Gr. 50 steel was assembled. A statistical evaluation was then conducted to identify key factors that contribute to high overstrength. It was found that a thick flange alone could not explain the high overstrength observed from testing. A multi-variate regression analysis was then conducted, and, for use in practical design, an equation (Equation 10) was proposed to evaluate the overstrength factor for shear links. The equation contains two contributing factors. The ratio between the expected tensile strength and expected yield stress of the web plays a more important role. The K_w term in Equation 10, which is defined in Equation 6, reflects the localized bending (or kinking) contribution of the flanges at link ends to the link shear strength; this effect is analogous to the column flange contribution of panel zone design strength in special moment frames.

ACKNOWLEDGMENTS

Part of this work was funded by the National Research Foundation of Korea (No. 2020R1A4A4079299).

REFERENCES

AISC (1997), *Seismic Provisions for Structural Steel Buildings*, American Institute of Steel Construction, Chicago, Ill.

AISC (2016), *Seismic Provisions for Structural Steel Buildings*, ANSI/AISC 341-16, American Institute of Steel Construction, Chicago, Ill.

AISC (2022a), *Seismic Provisions for Structural Steel Buildings*, ANSI/AISC 341-22, American Institute of Steel Construction, Chicago, Ill.

AISC (2022b), *Specification for Structural Steel Buildings*, ANSI/AISC 360-22, American Institute of Steel Construction, Chicago, Ill.

Azad, S.K. and Topkaya, C. (2017), "A Review of Research on Steel Eccentrically Braced Frames," *Journal of Constructional Steel Research*, Vol. 128, pp. 5373.

Barecchia, E., Della Corte, G., and Mazzolani, F.M. (2006), "Plastic Over-Strength of Short and Intermediate Links," *Proceedings of the 5th International Conference on Behaviour of Steel Structures in Seismic Areas* (STESSA), pp. 177–183, Taylor & Francis Group, London.

Bruneau, M., Anagnostopoulou, M., MacRae, G., Clifton, C., and Fussell, A. (2010), "Preliminary Report on Steel Building Damage from the Darfield Earthquake of September 4, 2010," *Bulletin of the New Zealand Society for Earthquake Engineering*, Vol. 43, No. 4, pp. 351–359.

Bruneau, M., Uang, C.-M., and Sabelli, R. (2011), *Ductile Design of Steel Structures*, McGraw-Hill, New York, N.Y.

Chi, B. and Uang, C.-M. (2000), "Cyclic Testing of Steel Shear Links for the San Francisco Moscone Convention Center Expansion Project," Report No. TR-99/06, Department of Structural Engineering, University of California, San Diego, La Jolla, Calif.

Clifton, C., Bruneau, M., MacRae, G., Leon, R., and Fussell, A. (2011), "Steel Structures Damage from the Christchurch Earthquake Series of 2010 and 2011," *Bulletin of the New Zealand Society for Earthquake Engineering*, Vol. 44, No. 4, pp. 297–318.

Dusicka, P., Itani, A.M., and Buckle, I.G. (2010), "Cyclic Behavior of Shear Links of Various Grades of Plate Steel," *Journal of Structural Engineering*, Vol. 136, No. 4, pp. 370–378.

Ji, X.D., Wang, Y.D., and Okazaki, T. (2016), "Cyclic Behavior of Very Short Steel Shear Links," *Journal of Structural Engineering*, Vol. 142, No. 2, 04015114.

Gulec, C.K., Gibbons, B., Chen, A., Sim, H.B., and Uang, C.-M. (2012), "Full-Scale Testing of Transbay Terminal Center Eccentrically Braced Frame Link Beams," *Proceedings of the 81st Annual Convention*, Structural Engineers Association of California, Sacramento, Calif., pp. 455–479.

Itani, A.M., Elfass, S., and Douglas, B.M. (2003), "Behavior of Built-Up Shear Links under Large Cyclic Displacement," *Engineering Journal*, AISC, Vol. 40, No. 4, pp. 221–234.

Kasai, K. and Popov, E.P. (1986), "General Behavior of WF Steel Shear Link Beams," *Journal of Structural Engineering*, Vol. 112, No. 2, pp. 362–382.

Malley, J.O. and Popov, E.P. (1984), "Shear Links in Eccentrically Braced Frames," *Journal of Structural Engineering*, Vol. 110, No. 9, pp. 2,275–2,295.

Mansour, N., Christopoulos, C., and Tremblay, R. (2011), "Experimental Validation of Replaceable Shear Links for Eccentrically Braced Steel Frames," *Journal of Structural Engineering*, Vol. 137, No. 10, pp. 1,141–1,152.

McDaniel, C.C., Uang, C.-M., and Seible, F. (2003), "Cyclic Testing of Built-Up Steel Shear Links for the New Bay Bridge," *Journal of Structural Engineering*, Vol. 129, No. 6, pp. 801–809.

Okazaki, T. and Engelhardt, M.D. (2007), "Cyclic Loading Behavior of EBF Links Constructed of ASTM A992 Steel," *Journal of Constructional Steel Research*, Vol. 63, No. 6, pp. 751–765.

Popov, E.P. and Engelhardt, M.D. (1988), "Seismic Eccentrically Braced Frames," *Journal of Constructional Steel Research*, Vol. 10, pp. 321–354.

Roeder, C.W. and Popov, E.P. (1978), "Eccentrically Braced Steel Frames for Earthquakes," *Journal of the Structural Division*, Vol. 104, No. 3, pp. 391–411.

Richards, P.W. and Uang, C.M. (2006), "Testing Protocol for Short Links in Eccentrically Braced Frames," *Journal of Structural Engineering*, Vol. 132, No. 8, pp. 1,183–1,191.

Sim, H.B. and Uang, C.-M. (2011), "Cyclic Testing of Shear Link Subassemblies in Support of Design for Transbay Transit Center in San Francisco," Report No. TR-11/02, Department of Structural Engineering, University of California, San Diego, La Jolla, Calif.

Steel-Plate Composite Wall to Reinforced Concrete Wall Mechanical Connection—Part 2: In-Plane and Out-Of-Plane Shear Strength

Hassan S. Anwar, Jungil Seo, Amit H. Varma, and Yoonho Nam

ABSTRACT

In safety-related nuclear facilities, steel-plate composite (SC) walls are often used in combination with reinforced concrete (RC) walls or foundations. The design demands need to be transferred between the two different structural systems through appropriate connection design. A design procedure was developed by the authors, and it was evaluated by conducting two full scale tests for SC wall-to-RC wall mechanical connections subjected to out-of-plane flexure. The experimental and numerical results are discussed in Part 1 (Seo et al., 2022). This paper presents a brief description of the design procedure as well as the experimental and numerical investigations conducted to further evaluate the design procedure. The focus was on the performance, strength, and governing failure mode of an SC wall-to-RC wall mechanical connection under in-plane and out-of-plane shear. The investigation results include global force-displacement and applied force-strain responses. The paper also presents overall damage progression in terms of concrete cracking patterns. The experimentally observed and numerically predicted results indicate that the proposed connection design procedure is suitable and conservative for SC wall-to-RC wall mechanical connections.

Keywords: Reinforced concrete, steel-plate composite, mechanical connection, full-strength connection design, wing plate, tie plate, baseplate, In-plane shear, out-of-plane shear, LS-DYNA

INTRODUCTION

Steel-plate composite (SC) walls forming a modular construction system have emerged as a viable alternative to conventional reinforced concrete (RC) walls over the past decade. A typical SC wall is comprised of two steel faceplates, concrete infill, steel headed stud anchors, and tie bars as illustrated in Figure 1. This innovative structural wall has well-known benefits, including superb structural performance (Ozaki et al., 2004; Varma et al., 2014; Bruhl et al., 2015a; Sener et al., 2015; Anvari et al., 2020), and construction schedule economy (DOE, 2006; IAEA, 2011). Consequently, SC walls are continuously gaining interest in the commercial building industry as well as in nuclear power plant construction. In the building industry, SC walls are being used as primary lateral load-resisting systems in high-rise construction. In safety related nuclear facilities, SC walls are being used in lieu of conventional RC walls in the construction of AP1000® in the United States and China as well as in the design of US-APWR®. SC walls are designed to withstand seismic, wind, impulse, impact, and accident thermal loadings (Sener and Varma, 2021), and they typically replace RC walls to prevent rebar congestion due to higher force demands (Seo and Varma, 2017a). However, it is challenging to completely replace RC walls with SC walls in a structure for multiple reasons such as: (i) lack of code provisions for structural systems that are not governed by AISC N690, *Specification for Safety-Related Steel Structures for Nuclear Facilities* (AISC, 2018), (ii) costs associated with implementing SC walls in the entire structure, and (iii) the designer's personal preference for RC walls. Thus, their potential for superior structural performance and accelerated construction schedules can only be realized through appropriate connections between SC walls and RC walls.

SC-to-RC connections can be categorized as: (i) SC wall-to-RC wall connections, (ii) SC wall-to-RC slab connections, and (iii) SC wall-to-RC basemat connections. SC-to-RC connections can be difficult to design as the structural behavior and force transfer mechanisms of the two systems are different from each other. In addition, different connecting elements such as post-tensioned reinforcement, steel headed stud anchors, and shear lugs, etc. (Bhardwaj and Varma, 2017) can be considered for transferring different in-plane and out-of-plane design demands.

Hassan S. Anwar, Graduate Research Assistant, Purdue University, West Lafayette, Ind. Email: hsagheer@purdue.edu (corresponding)

Jungil Seo, Research Assistant Professor, Purdue University, West Lafayette, Ind. Email: seo2@purdue.edu

Amit H. Varma, Karl H. Kettelhut Professor and Director of Bowen Laboratory, Purdue University, West Lafayette, Ind. Email: ahvarma@purdue.edu

Yoonho Nam, Engineering Group Supervisor, Civil & Architectural Engineering Dept. KEPCO E&C, Korea, Email: yoonho.nam@gmail.com

Paper No. 2022-02

JEAC (2009) recommends three connection techniques to transfer forces between an SC wall and an RC basemat, namely, (a) embedding steel faceplates in the RC basemat via shear connectors, (b) anchoring the steel faceplates and RC basemat dowel bars to the baseplate, and (c) non-contact lap splicing between faceplates and dowel bars. These techniques are discussed by Seo et at. (2022).

The SC wall can be connected to an RC wall using a non-contact lap splice or mechanical connections. Typically, more than one reinforcement layer is used in RC walls due to higher force demands. A non-contact lap splice connection for rebar larger than 1.4 in. diameter (#11) would require significant development length (L_d) which may not be an option at certain locations. To prevent this issue, mechanical splicing of rebar greater than 1.4 in. diameter (#11) can be done using the guidance provided by ACI 349-06, *Code Requirements for Nuclear Safety-Related Concrete Structures and Commentary* (ACI, 2006). However, design requirements for mechanical splicing of reinforcement (#11 and beyond) in RC structures per ACI 349-06 cannot be easily applied to SC wall-to-RC wall mechanical connections. This is attributed to the involved force transfer mechanisms associated with two different structural systems and lack of prescriptive design requirements in AISC N690. Therefore, a design procedure for the SC wall-to-RC wall mechanical connection was developed by the authors based on available design philosophy and concepts.

This paper focuses on the behavior and design of only SC wall-to-RC wall mechanical connections, as the other two connections have already been explored by Kurt (2016) and Seo and Varma (2017b). It presents: (i) a brief description of the development of the design procedure, (ii) results and observations from both experimental and numerical investigations conducted to evaluate the performance of the designed mechanical connection under in-plane shear (IPV) and out-of-plane shear (OOPV), and (iii) validation of the design procedure.

BACKGROUND

SC-RC structural connections can be designed in accordance with the performance-based connection design philosophies permitted by AISC N690 for SC wall connections. Accordingly, the design procedure can be based on either an overstrength connection philosophy or a full-strength connection philosophy. In the case of an overstrength connection, the connection is designed for 200% of seismic and 100% of the nonseismic design demands. However, the connection can be weaker than the connected structures. When a full-strength connection is implemented, the connection is designed to develop the full strength (125%) of the weaker of the connected structural members. That is, the energy dissipation in the formation of a plastic hinge would occur outside the connection region during a design basis or beyond seismic event. For this reason, the full-strength connection design is preferred in most cases.

The IPV and OOPV need to be transferred from the concrete and steel components of the RC wall to the SC wall and vice versa. Therefore, it is important to develop a basic understanding of the response of the SC wall under such loading scenarios before discussing the different SC wall-to-RC connection techniques. The behavior of an RC wall under such loading is well known (Biskinis et al., 2004; Mo et al., 2008; Carrillo et al., 2013; Usta, 2017), and will not be repeated here.

In-Plane Shear (IPV) Behavior of SC Wall

The IPV response of SC wall panels was experimentally investigated by Ozaki et al. (2004). The testing program consisted of nine square specimens of 47.2 × 47.2 × 7.9 in. size as shown in Figure 2. The test specimens were subjected to cyclic IPV. The study investigated the influence of steel plate thickness, axial force, and partitioning the web. The specimens exhibited good ductility with a linear relationship between yield strength and steel-plate thickness. The findings from Ozaki et al. (2004) were used to

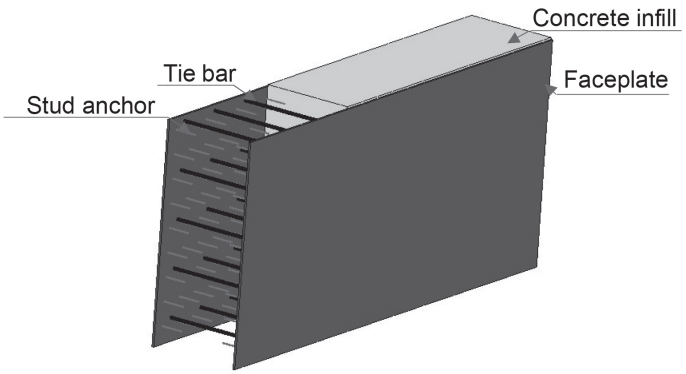

Fig. 1. Typical layout of SC wall.

develop a tri-linear response based on a mechanics based model (MBM) by Varma et al. (2014). The SC wall in-plane (IP) behavior can be simplified into a linear response in three stages: (i) concrete pre-cracking stage where concrete and steel components are in elastic range, (ii) concrete post-cracking stage where steel components are still in elastic range, and (iii) von Mises yield stage with no additional strength or stiffness. The study by Varma et al. (2014) concluded that the MBM model was conservative in predicting the response of SC wall panels tested by Ozaki et al. (2004).

An experimental study was conducted by Epackachi et al. (2015a) to investigate the influence of wall thickness, reinforcement ratio, and tie bar and shear connector spacing on the IP cyclic behavior of rectangular SC walls. The four SC wall specimens, anchored to the concrete basemat using a baseplate bolted connection, failed in flexure. The study concluded that the distance between shear connectors and the baseplate had significant impact on the post-peak shear behavior.

Seo et al. (2016) compiled a comprehensive experimental database of the 26 tests conducted on SC walls (with boundary elements) in the US, Japan, and South Korea. The experimentally observed IPV strength from these tests was compared with the strength predicted by the MBM, ACI 349-06 (ACI, 2006), and AISC N690s1, Specification for Safety-Related Steel Structures for Nuclear Facilities Including Supplement No. 1, (AISC, 2015) design code equations. It was concluded that the design equations used in AISC N690s1 and the MBM predicted the shear strength conservatively, and that the faceplate reinforcement ratio is the key parameter influencing the IPV strength.

Booth et al. (2020) developed an analytical approach using composite shell theory to determine IP response of the SC walls. Equations for predicting the ultimate shear strength and peak shear stains were developed and verified using an existing experimental database of the SC walls. The authors reported that existing shear strength estimation, based on the von Mises yielding of faceplates, is a lower bound estimate because it does not include post-yield shear strength of the walls.

Out-of-Plane Shear (OOPV) Behavior of SC Wall

Sener and Varma (2021) carried out an experimental and analytical study to evaluate the OOPV behavior of SC walls. The test matrix included 10 full-scale SC walls with design parameters including section depth, shear and longitudinal reinforcement ratios, shear span-to-depth ratio, and faceplate thickness. A typical configuration of the full-scale SC wall from the test matrix is shown in Figure 3. The results of this study concluded that current AISC N690 design recommendations are adequate for estimating OOPV strength of SC walls.

SC-RC Connections

Seo and Varma (2017a) experimentally investigated the axial behavior of non-contact lap splice connections, which is one of the typical connection techniques between an SC wall and RC basemat (connection type "c" discussed in the introduction). The authors identified the force transfer mechanism of the connection and developed design recommendations for the SC-to-RC non-contact lap splice connections based on experimental and numerical results.

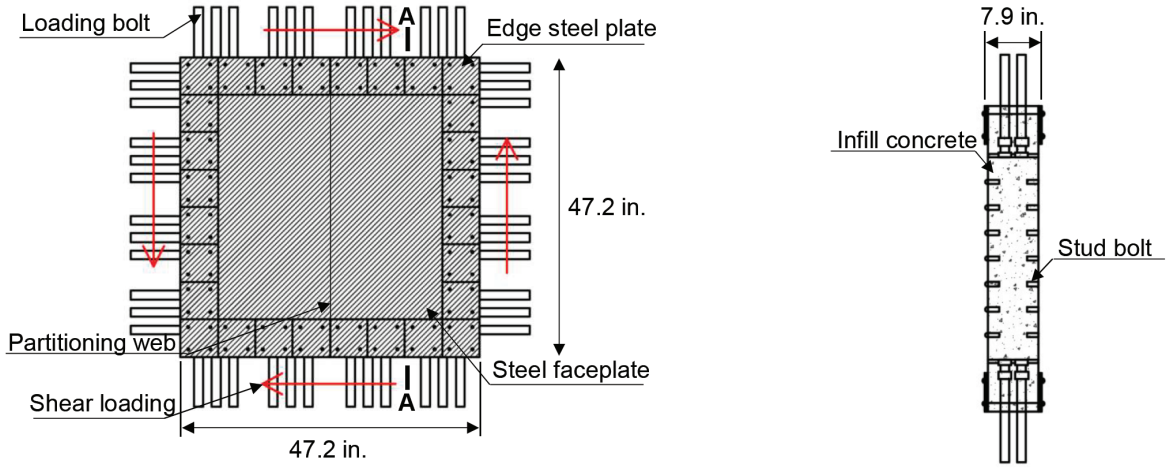

(a) Plan View *(b) Section view A-A*

Fig. 2. SC wall panel in-plane shear test (Ozaki et al., 2004).

Kurt (2016) investigated the full-strength connection philosophy by conducting an experimental and numerical study. SC wall specimens with aspect ratios (h_{wall}/l_{wall}) ranging from 0.6 to 1 were subjected to cyclic in-plane shear until failure. Details of the full-strength connection between the SC wall and RC foundation are shown in Figure 4. The results of this investigation were used to propose design equations to predict the lateral loading capacity of SC walls. The study concluded that the IPV strength decreased with an increase in the aspect ratio of the SC walls.

Seo et al. (2022) developed the design procedure for mechanical connections between SC and RC walls using the full-strength connection design philosophy. Experimental and numerical studies were conducted to evaluate the performance of the mechanical connection designed under out-of-plane flexure. The study concluded that the proposed design procedure was suitable and conservative for designing SC wall-to-RC wall mechanical connections. It was recommended that additional investigations need to be conducted to verify the performance of the design procedure for different loading conditions.

FORCE TRANSFER MECHANISM AND DESIGN PROCEDURE

Figure 5 illustrates the main force transfer mechanism of the SC wall-to-RC wall connection subjected to IPV and OOPV. The shear force transfer takes place across the two concrete surfaces (SC and RC) through friction as a result of clamping force in the rebar embedded in both the SC and RC walls. In this study, it was assumed that the mechanical connection can develop 125% of the yield strength of each rebar, $T_1 = T_2 = T_3 = T_4 = 1.25A_{s,r}F_{y,r}$. That is, sufficient embedment length is provided to the rebar in the RC portion, and therefore, no premature failure of the RC portion associated with the rebar embedment length occurs.

The assumption also results in the maximum shear friction force, V_nSF, of $1.25A_{s,r}F_{y,r}$ per rebar. However, the shear friction force is limited by the lesser of $(480+0.08f_c')A_c$, $0.2f_c'A_c$, and $1600A_c$ in accordance with ACI 318-19, *Building Code Requirements for Structural Concrete* (ACI, 2019), Section 22.9.4.4, where A_c is the area of concrete parallel to the applied shear. In addition, the shear strength of the RC portion (with conventional shear reinforcement)

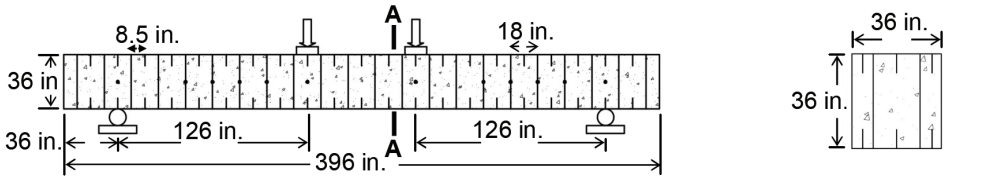

(a) Elevation view *(b) Section view A-A*

Fig. 3. SC wall four-point bending test (Sener and Varma, 2021).

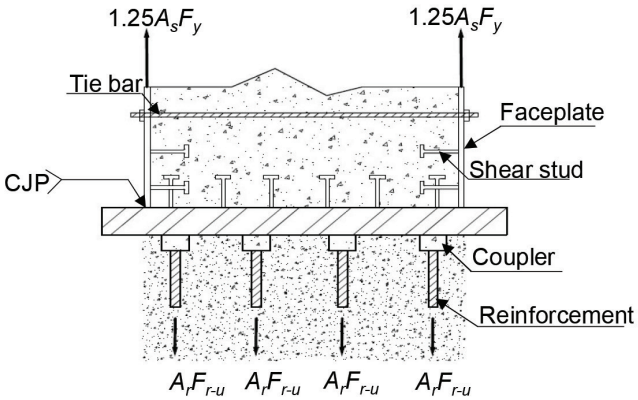

Fig. 4. Full-strength connection between SC wall and concrete foundation (Kurt, 2016).

is less than that of the SC portion. This would potentially result in the shear failure of the RC portion prior to the SC portion while developing rebar strength less than 125% of the rebar yield strength. Additionally, the axial force from the rebar is transferred to the faceplates, which generates eccentric moment that is resisted by SC infill concrete near the baseplates and tie plates that connect the two faceplates.

Additional assumptions made for the design procedure include (1) connected RC and SC walls have already been designed with the same thickness and (2) the wing plate and baseplate have the same width. Figure 6 shows a typical configuration of the designed SC wall-to-RC wall mechanical connection. As shown, the RC wall flexural reinforcement is extended inside the SC wall and connected to the baseplates using mechanical couplers. Baseplates are welded to faceplates and wing plates to provide stability against rebar forces. Tie plates, welded to the faceplates, are provided to resist the tensile component of the moment generated due to eccentricity.

Tie Plate Design

Figure 7 illustrates how the rebar force induced by transferring shear force through shear friction is transferred to the mechanical connection region. In the figure, $R_{u,tp}$ is the required axial force involved in the design of the tie

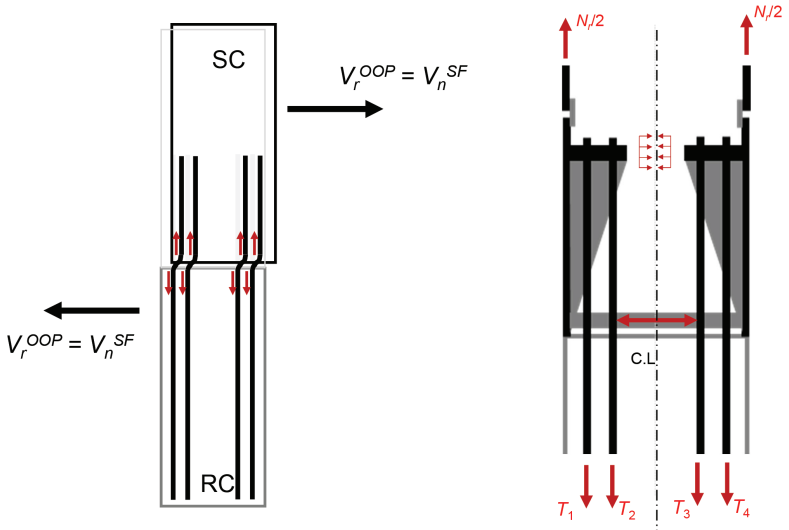

Fig. 5. IPV and OOPV force transfer mechanism (Seo et al., 2022).

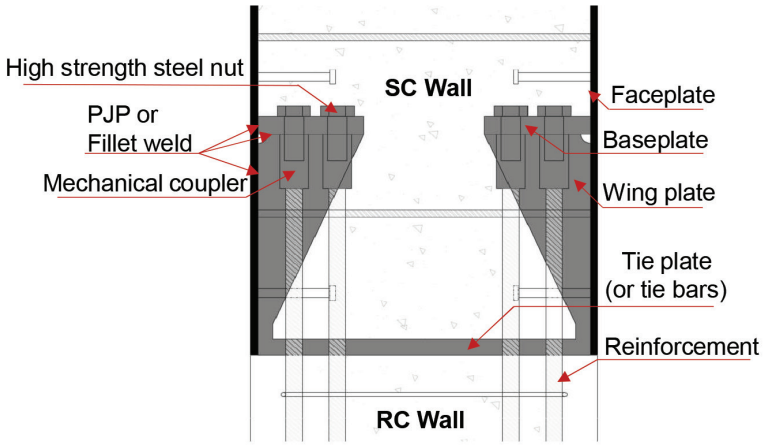

Fig. 6. Typical configuration of mechanical splice connection (Seo et al., 2022).

plate. As shown, the magnitude of $R_{u,tp}$ can be determined by taking the moment about 'O' and the resulting equation is shown as Equation 1. In the equation, h_3 and h_4 are the respective rebar distances from the centerline (CL), h_{tp} is the center-to-center distance between the tie plate and the baseplate, t_p is the faceplate thickness, t_{wall} is the thickness of the wall, and N_r is the maximum transferrable axial force from RC wall-to-SC wall.

$$R_{u,tp} = \frac{\left[\frac{N_r}{2}\left(\frac{t_{wall}}{2} - \frac{t_p}{2}\right)\right] - (T_3 h_3 + T_4 h_4)}{h_{tp}} \quad (1)$$

Baseplate Design

Baseplate design is performed for a unit length of 1 in. using the yield line method. The unit length of the baseplate is subjected to two concentrated forces from the steel reinforcement equal to 125% of the yield strength per rebar ($1.25A_{s,r}F_{y,r}$). The yield line method considers the structural element at its collapse state. The details of the collapse mechanism and respective yield lines corresponding to the flexural capacities (M^+, M^-) are shown in Figure 8. W_{bp} is the width of baseplate, whereas $t_{p,wp}$ and S_{wp} are the thickness and spacing between the wing plates, respectively. Additionally, S_{r1} is the distance of the rebar from the faceplate and S_{r2} is the center-to-center distance between the rebar. Figure 9 illustrates the external work ($\sum W_{ext}$) done in undergoing small deflection (Δ) and the internal work ($\sum W_{int}$) done in rotations (θ_1, θ_2) along yield lines. The required flexural capacity of the baseplate ($M_{u,bp}$) can be determined by equating $\sum W_{ext}$ and $\sum W_{int}$, where $\sum$Wext, $\sum W_{int}$, and $M_{u,bp}$, are given by Equations 2, 3, and 4, respectively.

$$\sum W_{ext} = 2P\Delta = 2(1.25A_{s,r}F_{y,r})\Delta \quad (2)$$

$$\sum W_{int} = \sum Ml\theta \quad (3)$$

$$M_{u,bp} = M = \frac{2(1.25A_{s,r}F_{y,r})\Delta}{2l_1\theta_1 + l_2(\theta_1+\theta_2) + l_3(\theta_1+\theta_2) + l_4\theta_1 + l_6\theta_1 + l_5\theta_2} \quad (4)$$

where

$\Delta = 1$

$l_1 = W_{bp} - S_{r1} - 1.5d_{hole}$

$l_2 = l_3 = \sqrt{\left(\frac{S_{wp} - t_{p,wp}}{2}\right)^2 + (S_{r1})^2} - \frac{1}{2}d_{hole}$

$l_4 = l_6 = W_{bp}$

$l_5 = S_{wp} - t_{p,wp}$

Finally, the minimum baseplate thickness, $t_{p,bp,min}$, can be computed from the ratio of required strength to available design strength ($\phi M_{n,bp} = \phi F_y Z$) as shown in Equation 5:

$$t_{p,bp,min} = \sqrt{\frac{8(1.25A_{s,r}F_{y,r})}{\frac{2l_1\theta_1 + l_2(\theta_1+\theta_2) + l_3(\theta_1+\theta_2) + l_4\theta_1 + l_6\theta_1 + l_5\theta_2}{\phi F_{y,bp}}}} \quad (5)$$

where

$$Z = \frac{(1\text{ in.})(t_{p,bp})^2}{4}$$

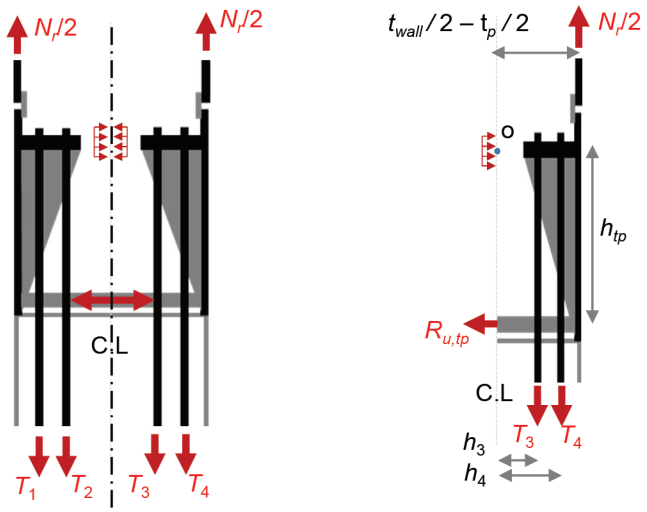

Fig. 7. Required axial force ($R_{u,tp}$) for tie plate design (Seo et al., 2022).

Wing plate Design

The geometry and loading conditions of the wing plate shown in Figure 10 are identical to the triangular bracket seat as shown in the Companion to the AISC Steel Construction Manual Volume 1 (AISC, 2019). Thus, the triangular bracket seat design can be implemented for the wing plate if *P*, *a*, and *b* [Figure 10(b)] can be replaced by T_1+T_2, htp, and Wbp [Figure 10(a)]. The design process involves determination of the wing-plate thickness and calculation of demands and available strengths along section A-A and B-B as shown in Figure 10(b).

EXPERIMENTAL PROGRAM

The experimental investigations were conducted to evaluate the performance of the SC wall-to-RC wall mechanical connections designed through the procedure already shown. The experimental program involved testing seven mechanical connections comprised of four full-scale and three scaled specimens. Full-scale specimens were subjected to monotonic out-of-plane moment (OOPM) and OOPV, whereas the scaled specimens underwent cyclic IPV. In the current study, only OOPV (2 full scale) and IPV (2 small scale) loading scenarios are discussed. One scaled specimen exhibited significant voids and honeycombing during concrete casting, therefore useful experimental data could not be obtained from that specimen. The remaining 2 large-scale specimens subjected to OOPM are presented in Seo et al. (2022).

Design of Test Matrix

The test matrix was designed keeping in mind typical settings of a safety related nuclear facility. Test setup of specimens subjected to OOPV is shown in Figure 11. As shown, the specimen had a wall thickness, T_{wall}, of 36 in. and a wall width, w_{wall}, of 18 in. The length of the test unit, l_{span}, was

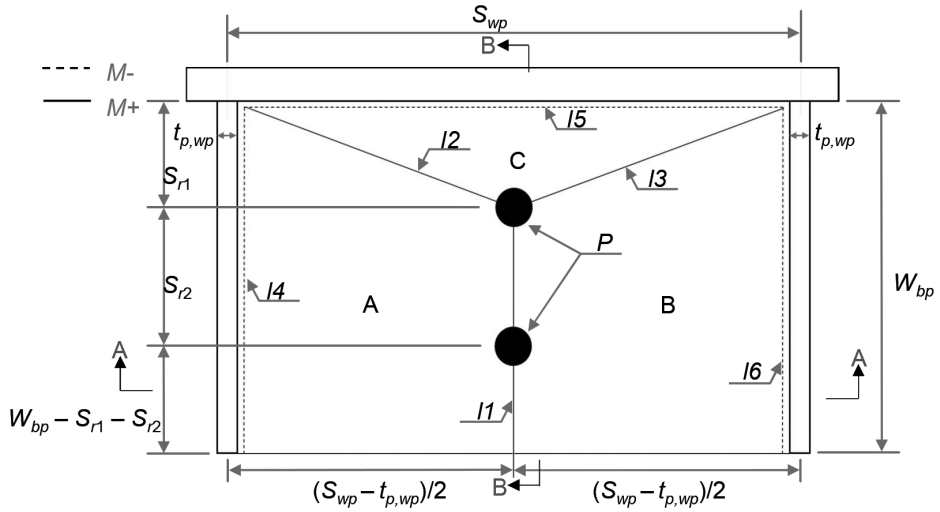

Fig. 8. Yield line method for baseplate design (Seo et al., 2022).

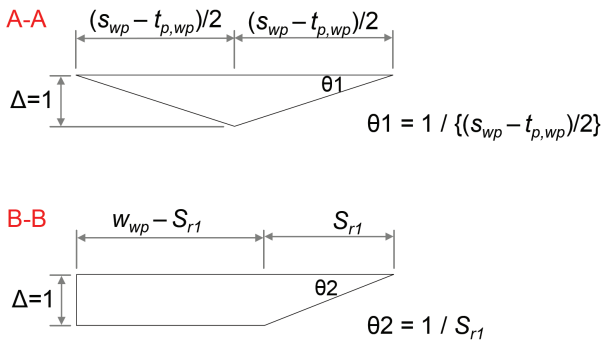

Fig. 9. Small deflection and rotations at section A-A and B-B (Seo et al., 2022).

180 in. ($5.0T_{wall}$). The SC wall portion is comprised of ¾ in. Gr. 50 faceplates (t_p), a reinforcement ratio (ρ_2) of 0.04, 1-in.-diameter steel headed stud anchors at 9 in. center-to-center spacing (s_s), and ASTM A706 Grade 60 #8 tie bars (connecting the faceplates with partial-joint-penetration welds) at 18 in. center-to-center spacing (s_t). The RC wall portion consisted of ASTM A706 Gr. 60 #14 flexural reinforcement (d_b = 1.69 in.) at center-to-center spacing ($s_{1,rc}$) of 9 in. with a longitudinal reinforcement ratio (ρ_1) of 0.014. The longitudinal rebar were placed in four curtains as a pair along each edge. Shear reinforcement of ASTM A706 Gr. 60 #4 double hoop stirrups were placed at the same center-to-center

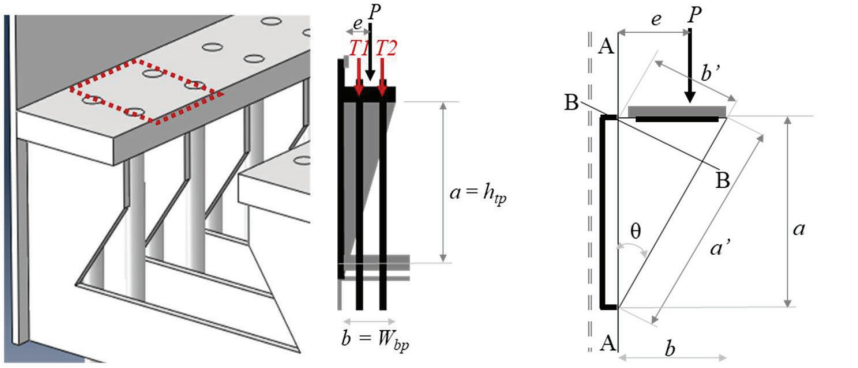

(a) Wing plate *(b) Bracket seat per AISC (2019)*

Fig. 10. Geometry and loading comparison (Seo et al., 2022).

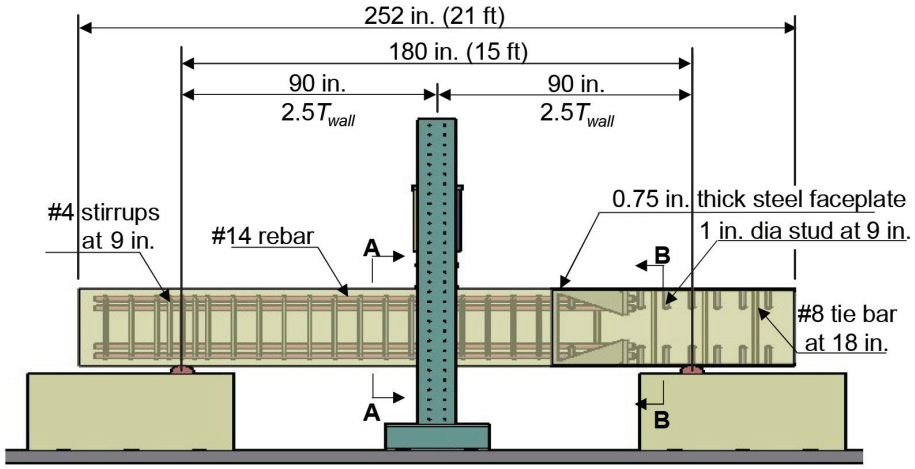

(a) Elevation view

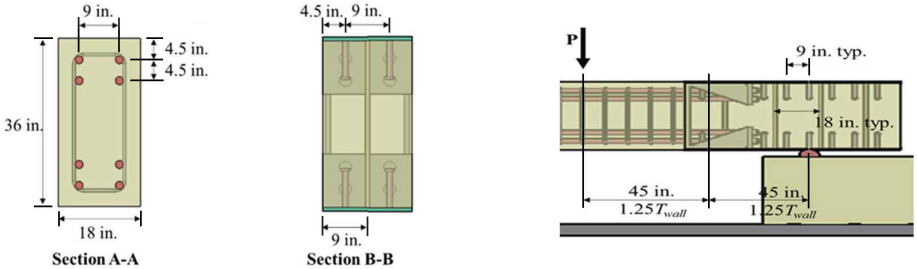

(b) Section view A-A *(c) Section view B-B* *(d) Connection region*

Fig. 11. OOPV test specimen.

spacing (9 in.) along the length of the RC wall. The connection region was comprised of a 1.75-in.-wide (w_{tp}) and 1-in.-thick tie plate (t_{tp}), an 11-in.-wide (w_{bp}) × 2-in.-thick baseplate (t_{bp}), and a 1-in.-thick wing plate (t_{wp}). The connection region was 27 in. long, and all steel plates within the mechanical connection region were Gr. 50.

The test setup of specimens subjected to IPV is shown in Figure 12. The ratio between full scale specimens (OOPV) and reduced scale specimens (IPV) was selected to be 1:3. Hence, the thickness (T_{wall}) and length of wall (l_{span}) for IPV specimens were 12 in. and 60 in., respectively. The specimen height-to-length ratio (h_{wall}/l_{span}) was kept to 1 to maximize the shear contribution. The 1:3 scaling refers to the geometric scaling of the RC and SC portions. However, the exact scaling could not be achieved for the longitudinal rebar. Consequently, the mechanical connection region was redesigned based on the developed design procedure. The SC wall portion consisted of ¼-in.-thick ASTM Gr. 50 faceplates (t_p), a reinforcement ratio (ρ_2) of 0.04, ¼-in.-diameter steel headed stud anchors at center-to-center spacing (s_s) of 3 in., and ASTM A706 Gr. 60 #4 tie bars at center-to-center spacing (s_t) of 6 in. The RC wall portion was comprised of ASTM A706 Gr. 60 #5 longitudinal and horizontal reinforcement (d_b = 0.62 in.), at center-to-center spacing ($s_{1,rc}$) of 3 in., with a reinforcement ratio (ρ_1) of 0.034. The connection region was 9 in. long and comprised of Gr. 50 steel plates constituting a 0.625-in.-wide (w_{tp}) × ⅜-in.-thick tie plate (t_{tp}), a 3.75-in.-wide (w_{bp}) × ⅝-in.-thick baseplate (t_{bp}), and a ⅜-in.-thick wing plate (t_{wp}).

The details of the test matrix are summarized in Table 1. The 2 full-scale and 2 scaled specimens mentioned in Table 1 are nearly identical to each other; the only difference is the rebar-to-baseplate connection configuration. Figure 13 illustrates the two connection plans considered in this study. The coupler (C) connection configuration utilizes a coupler to connect the tapered threaded longitudinal rebar to the baseplate using a high strength bolt (ASTM A449) as shown in Figure 13(a). The double nut (DN) connection configuration also utilizes the coupler, which is connected to the tapered threaded longitudinal rebar at one end and a threaded rod at the other end. The threaded rod is secured to the baseplate utilizing double nuts as shown in Figure 13(b). Table 2 presents the average measured material properties of the test specimens. The concrete strength represents the average measured strength at the day of test as per ASTM C39 (ASTM, 2014) standards. The table also shows the steel uniaxial tensile strength measured according to the ASTM E8 (ASTM, 2013) standards. The yield stress, F_y, was measured according to the 0.2% offset rule.

Instrumentation and Loading Protocol

The test setup of OOPV specimens subjected to monotonic loading, with a 500-kip hydraulic actuator at 45 in. away from the center of the connection region is shown in Figure 11. The arrangement of string potentiometers (SP) and displacement transducers (DT) is presented in Figure 14. As shown, SP1 was attached to the center of the connection region, and a pair of SP2/SP3 was attached under the loading point to measure global deflection and possible twisting of the test setup. Lastly, SP4 was attached under the center of the RC wall portion. One set of two DT was

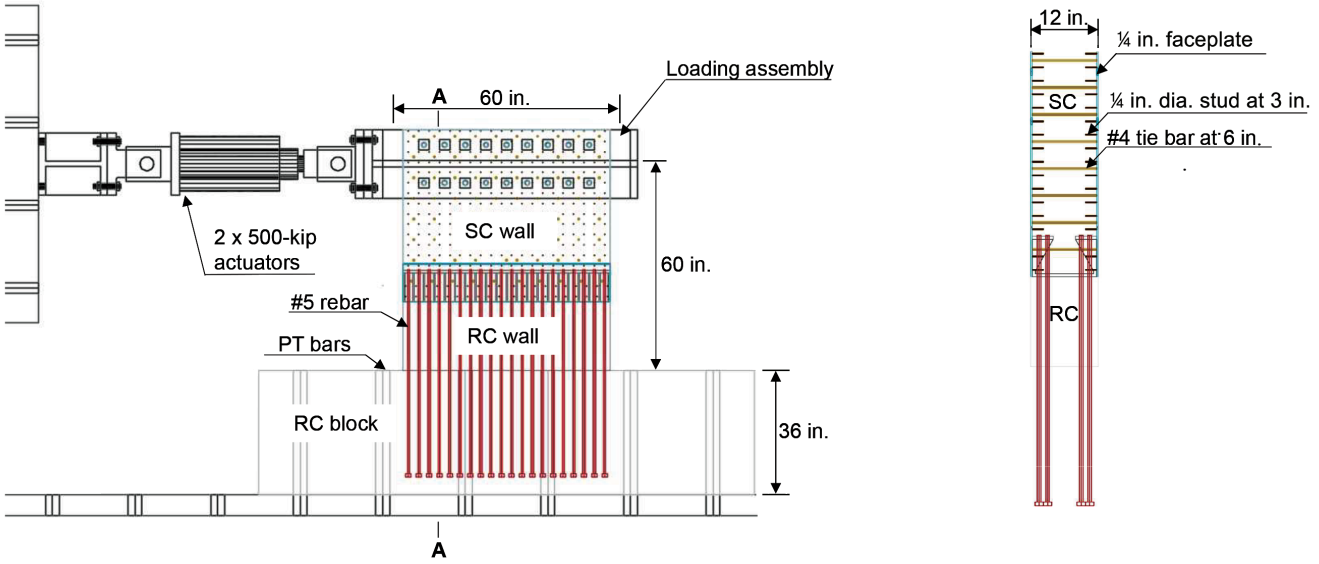

(a) Elevation view *(b) Section view A-A*

Fig. 12. IPV test specimen.

Table 1. Geometric Details of the Test Matrix															
	Overall Dimension			SC Wall				RC Wall			Connection				
Specimen	w_{wall}, h_{wall} (in.)	l_{span} (in.)	T_{wall} (in.)	t_p (in.)	ρ_2	s_s (in.)	s_t (in.)	d_b (in.)	$s_{1,rc}$ (in.)	ρ_1	w_{tp} (in.)	t_{tp} (in.)	w_{bp} (in.)	t_{bp} (in.)	t_{wp} (in.)
OOPV-C	18	180	36	¾	0.04	9	18	1.69	9	0.014	1.75	1	11	2	1
OOPV-DN	18	180	36	¼	0.04	9	18	1.69	9	0.014	1.75	1	11	2	1
IPV-C	60	60	12	¼	0.04	3	6	0.62	3	0.034	0.625	⅜	3.75	⅝	⅜
IPV-DN	60	60	12	¼	0.04	3	6	0.62	3	0.034	0.625	⅜	3.75	⅝	⅜

Table 2. Measured Properties of Test Specimens								
	Steel Yield Strength, F_y (ksi)						Concrete Strength, f'_c (ksi)	Connection Plan
Specimen	Faceplate	Baseplate	Tie Plate	Wing plate	Rebar	Stirrup		
OOPV-C	59	62	57	57	68	67	5.81	Coupler
OOPV-DN	59	62	57	57	68	67	5.76	Double nut
IPV-C	63	63	60	63	65	—	5.93	Coupler
IPV-DN	63	63	60	63	65	—	5.43	Double nut

placed under each roller support to measure the possibility of support settlement. Figure 15 shows the configuration of four electrical-resistance strain gauges (SG) on the interior wing plate and tie plate. One set of two SG was attached on the top and bottom of the baseplates using the configuration shown in Figure 16. In the case of #14 horizontal reinforcement, a pair of SG were attached on each rebar at a horizontal distance of 2 in. from the mechanical coupler as shown in Figure 17. Additionally, one set of two SG was attached on each alternate longitudinal rebar in the RC wall portion under the loading point as shown in Figure 18. Six pairs of SG were also installed on the shear stirrups near the loading point as per Figure 19. The overall lateral behavior of the actual structure is governed by the IPV behavior of both SC and RC walls, which serve as the primary lateral load-resisting system. Therefore, the IPV test specimens were subjected to cyclic lateral loading. The RC portion of the specimens was cast monolithically with the RC block. The RC block was post-tensioned to the laboratory strong floor to prevent sliding and overturning. The post-tensioning forces were designed to prevent any decompression of the concrete foundation from the strong floor, thus providing fixed base conditions. Lateral cyclic loading (and displacement) was applied using two 500-kip hydraulic actuators attached to the laboratory reaction wall and the loading assembly. The test setup of IPV specimens is shown in Figure 12. The lateral loading was increased cyclically as shown in Figure 20. In the figure, V_n is the lateral loading corresponding to the RC wall shear strength calculated using ACI 349-06 (ACI, 2006) Section 21.7.4.1. The measured material properties were used in the calculation, Δ_y is the projected displacement at V_n. Because the test specimens were expected to fail in a non-ductile manner, the displacement at the first cycle of $0.75V_n$ was used to calculate Δ_y. The displacement

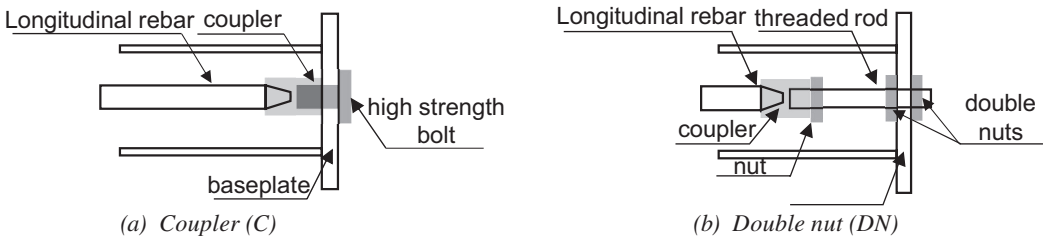

(a) Coupler (C) *(b) Double nut (DN)*

Fig. 13. Rebar to baseplate connection configuration (Seo et al., 2022).

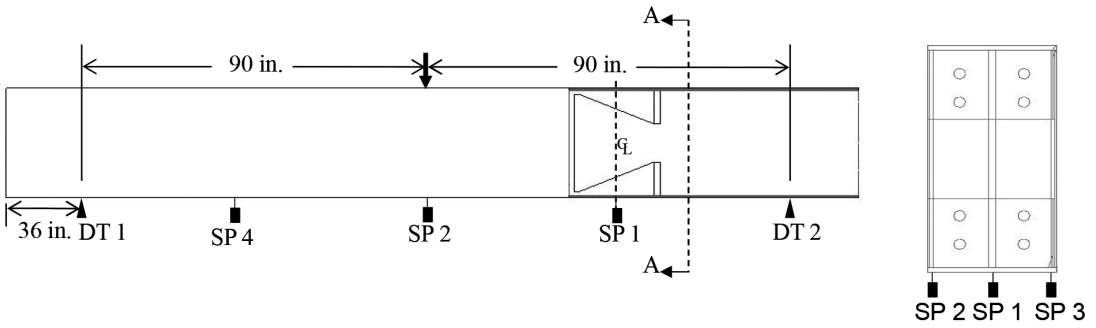

(a) Elevation view *(b) Section view A-A*

Fig. 14. SP and DT sensor layout (OOPV).

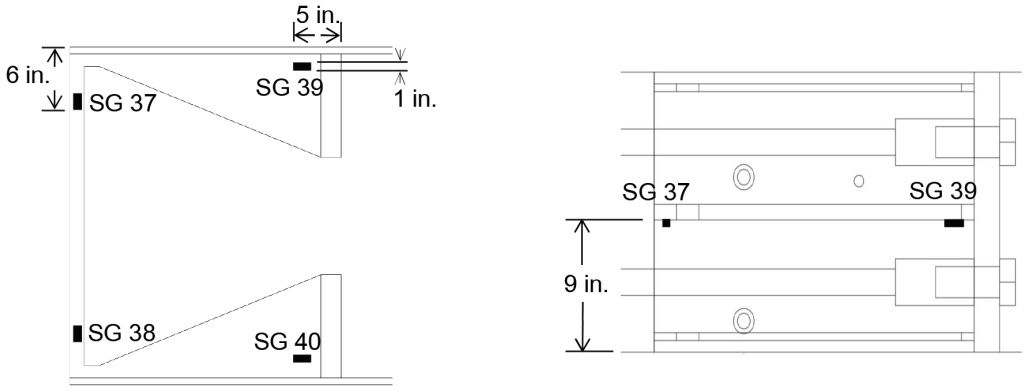

(a) Elevation view *(b) Plan view*

Fig. 15. SG layout of wing plates and tie plates (OOPV).

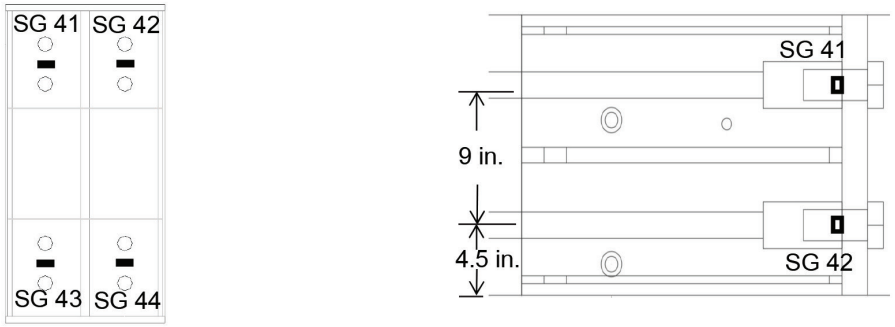

(a) Elevation view *(b) Plan view*

Fig. 16. SG layout of baseplates (OOPV).

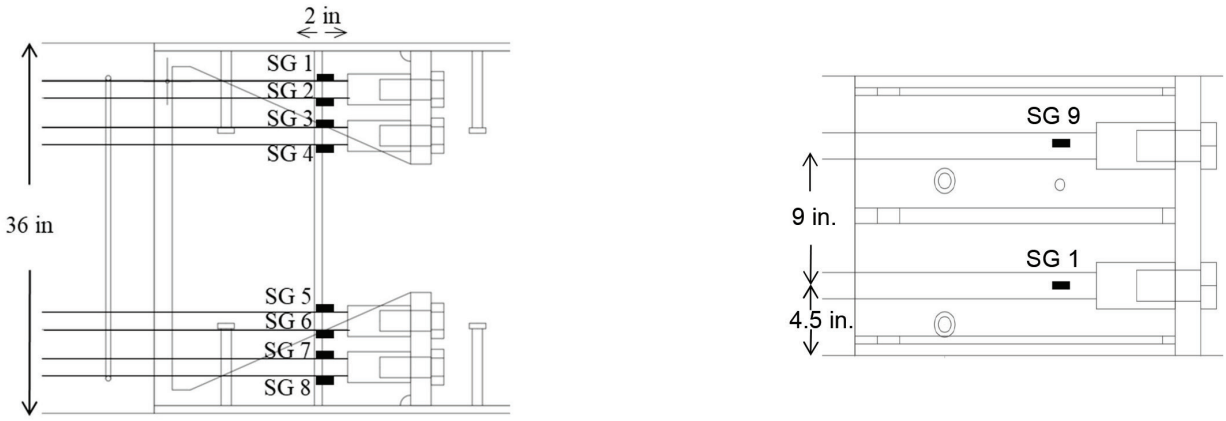

(a) Elevation view *(b) Plan view*

Fig. 17. SG layout of #14 rebar (OOPV).

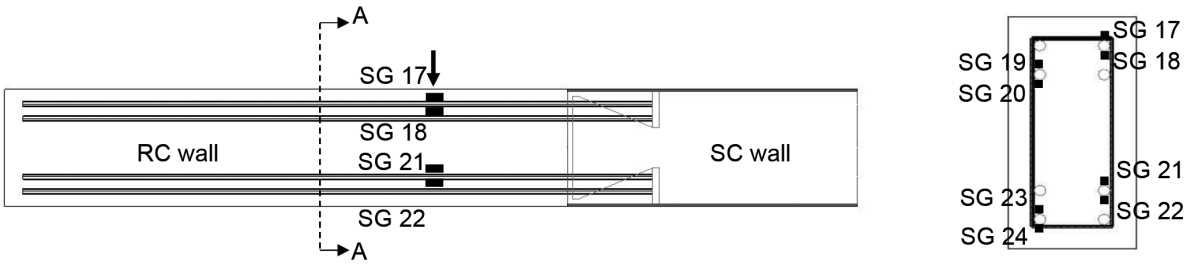

(a) Elevation view *(b) Section view A-A*

Fig. 18. SG layout of #14 rebar at loading point (OOPV).

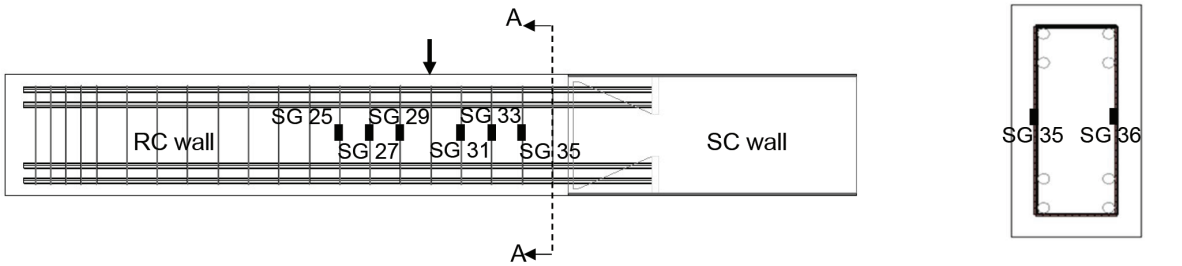

(a) Elevation view *(b) Section view A-A*

Fig. 19. SG layout of stirrups (OOPV).

at $0.75V_n$ was multiplied by 1.33 to estimate Δ_y. Additional displacement cycles with different amplitudes ($1.5\Delta_y$, $2.0\Delta_y$, and $3.0\Delta_y$) were also included in the loading protocol.

A total of seven SPs were utilized to measure the displacement of the RC wall, connection region, SC wall, and foundation block as shown in Figure 21. SP1-SP4 were employed to obtain lateral displacement profiles of the test setup by obtaining values at the loading point and the middle of the SC wall, connection region, and RC wall, respectively. SP5 was used to measure any base slip of the RC wall portion that may have occurred during the test. Lastly, SP6 and SP7 were used to measure vertical displacements. Strain gauge configuration on the tie plates was similar to the OOPV test specimens. Two SG each on exterior tie plate and wing plate were installed on each face of the wall as illustrated in Figure 22. Four pairs of SG were mounted on the vertical rebar at the base of the RC wall on each end (north and south), located at a horizontal distance of 4 in. from the RC foundation block as illustrated in Figure 23. Thus, a total of sixteen SG were installed on the specimen vertical rebar.

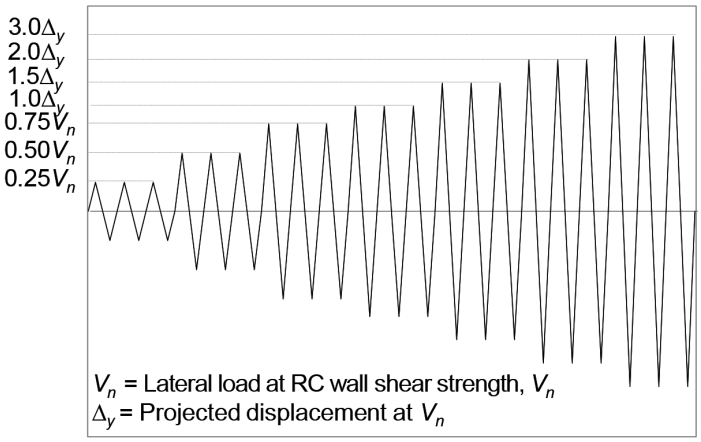

Fig. 20. IPV test loading protocol.

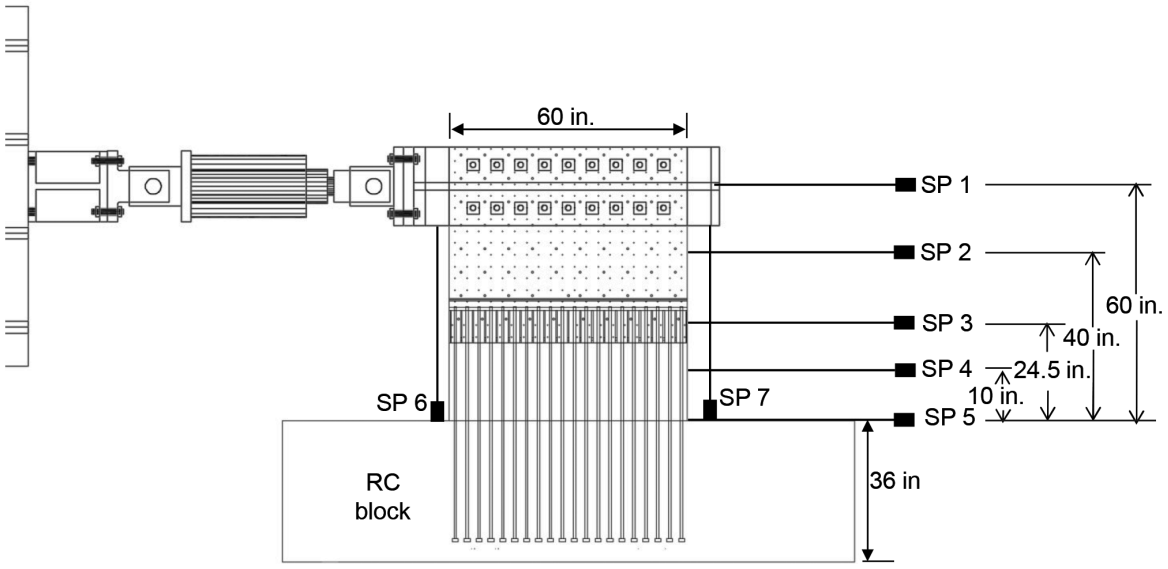

Fig. 21. SP layout (IPV).

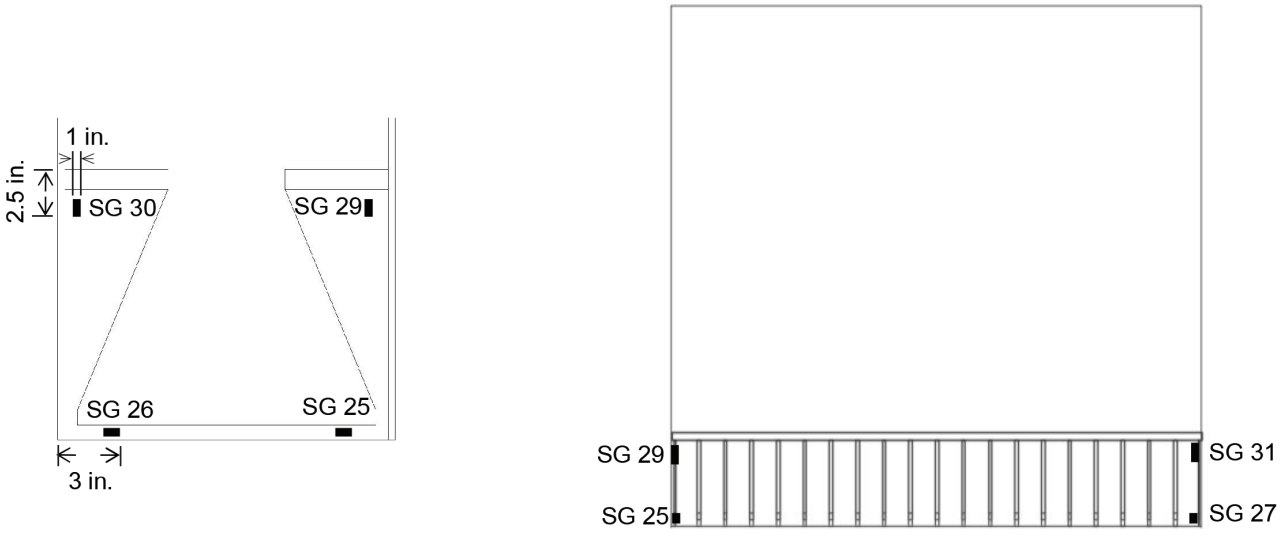

(a) Side view *(b) Elevation view*

Fig. 22. SG layout of wing plates and tie plates (IPV).

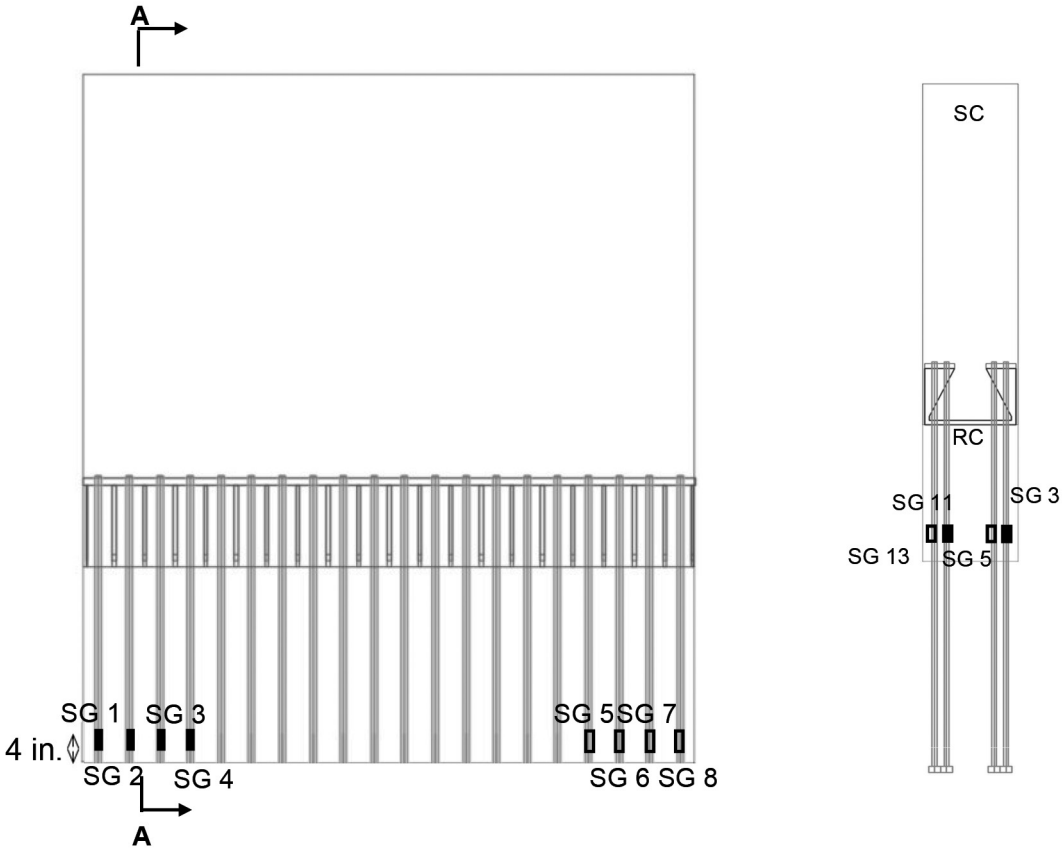

(a) Elevation view *(b) Section view A-A*

Fig. 23. SG layout of #5 rebar (IPV).

EXPERIMENTAL RESULTS

Specimen OOPV-C

Figure 24 shows the overall response in terms of the applied shear—displacement curves. The experimentally measured maximum shear force, V_{max}, was 205 kips, and the corresponding vertical displacements were 0.72 in., 0.41 in., and 0.38 in. at the center, at the RC wall portion, and at the SC wall portion respectively. As shown, initial concrete flexural cracks occurred in the RC wall portion at the applied shear, V, of 50 kips, resulting in changes in the stiffness. Additionally, a rapid increase in the displacement at V_{max} was observed in the RC wall portion due to significant cracking followed by yielding of the shear stirrups. As expected, the maximum displacement, Δ_{max}, was observed under the loading point (SP2,3). V_{max} was greater than the shear capacity of the RC wall portion calculated using ACI 349-06 using measured properties ($V_{n.RC}$ = 167 kips) by 38 kips (22%). The shear force associated with the flexural capacity of the RC wall portion ($V_{Mn.RC}$ = 174 kips) was greater than $V_{n.RC}$ confirming RC shear failure as the governing failure mode.

Figure 25 shows the applied shear–strain response for #14 rebar, #4 stirrups, tie plate, and baseplate. As shown, the bottom #14 rebar under the loading point exhibited strains greater than yield strain (ε_y = 2,328 με) with a maximum strain value of 2,555 με (SG 22). The maximum strain measured from the SG attached next to the couplers was 1,000 με (SG 16). Cracking in the RC wall portion is reflected in the form of yielding of the shear reinforcement with a maximum strain of 2,828 με (SG 25) at V_{max}. Additionally, the maximum strain for the tie plate and baseplate at V_{max} was 1,370 με (SG 38, tie plate) and 436 με (SG 44, baseplate) respectively, with corresponding stress values of

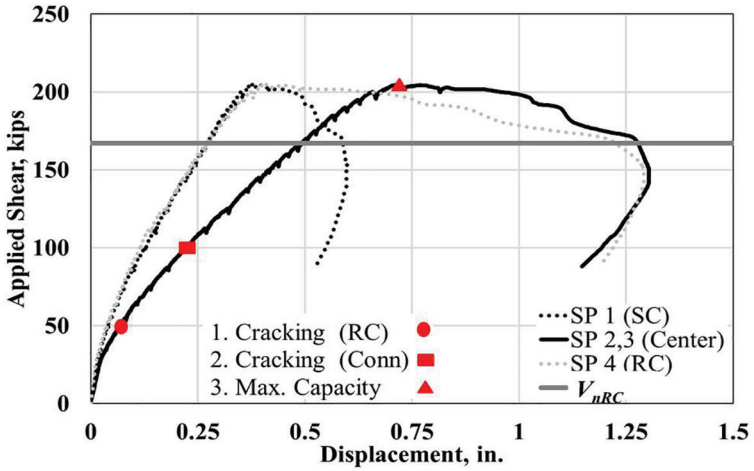

Fig. 24. Applied shear–displacement response (OOPV-C).

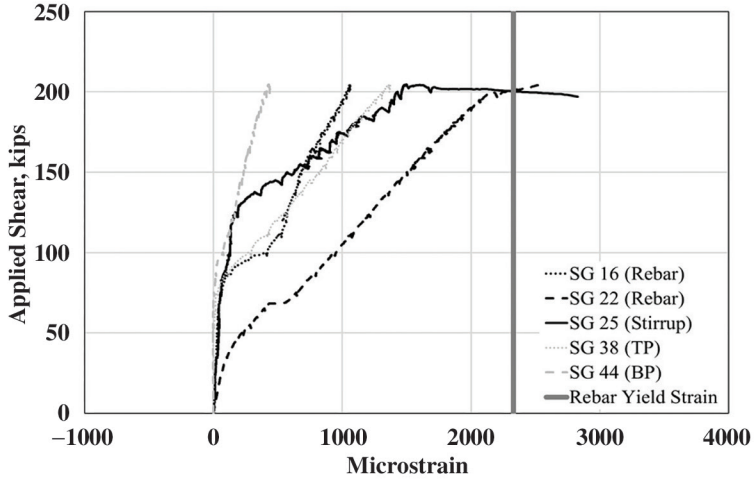

Fig. 25. Applied shear–strain response—#14 rebar, #4 stirrups, tie plate, and baseplate (OOPV-C).

39.7 ksi and 12.6 ksi. Thus, indicating conservatism in the design connection procedure.

Figure 26 shows the overall damage progression in terms of concrete crack patterns. Initially, flexural cracks occurred at the bottom of the RC wall portion at about 24% of V_{max}. As the load increased to 36% of V_{max}, the flexural cracks transformed into flexural-shear cracks along with the formation of new cracks within the RC wall portion. The first shear crack occurred in the connection region at around 100 kips ($0.5V_{max}$). Ultimately, the specimen failed as these diagonal tension cracks (shear cracks) connected the loading point and RC wall portion support as shown in the figure.

Specimen OOPV-DN

The applied shear–displacement response of Specimen OOPV-DN is shown in Figure 27. As shown, the response is similar to that observed from OOPV-C. The experimentally measured maximum shear, V_{max}, was 189 kips, and the corresponding vertical displacements were 0.99 in., 0.68 in., and 0.47 in. at the center, at the RC wall portion, and the SC wall portion, respectively. Initial concrete flexural cracks occurred in the RC wall portion at the applied shear, V, of 50 kips. Additionally, a rapid increase in the displacement at V_{max} was observed in the RC wall portion due to significant cracking followed by yielding of the shear stirrups. As expected, Δ_{max} was observed under the loading point (SP2,3). V_{max} was greater than the RC shear capacity calculated based on ACI 349-06 provisions using measured properties ($V_{n.RC}$ = 167 kips) by 13%. The shear force associated with the flexural capacity of the RC wall portion ($V_{Mn.RC}$ = 174 kips) was greater than $V_{n.RC}$. Thus, confirming RC shear failure as the governing failure mode.

Figure 28 presents the applied shear–strain response for #14 rebar, #4 stirrups, tie plate, and baseplate. As shown, the bottom #14 rebar under the loading point exhibited strains greater than yield strain (ε_y = 2,328 με) with a maximum strain value of 2,873 με (SG 24), whereas the maximum strain value of the rebar next to the couplers was approximately 1,000 με (SG 7). Cracking in the RC wall portion resulted in yielding of the shear reinforcement exhibiting a maximum strain of 2,622 με (SG 26) at V_{max}. Lastly, the respective maximum strain values for the tie plate and baseplate at V_{max} were 1,012 με (SG 37) and 245 με (SG 43) with corresponding stresses of 29.3 ksi and 7.10 ksi. Thus, the

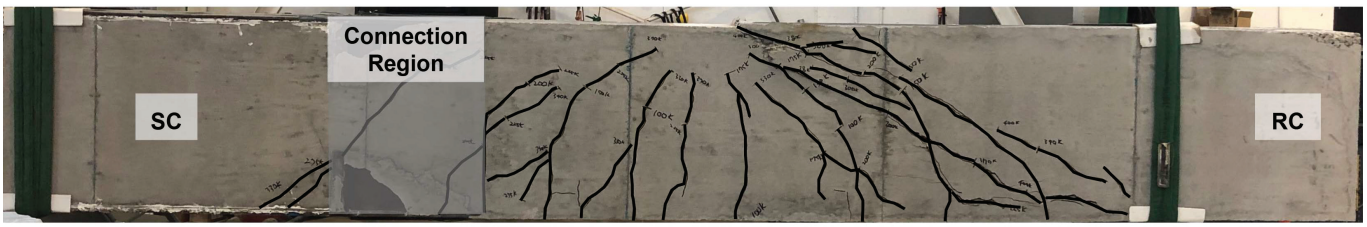

Fig. 26. Concrete crack pattern (west side) (OOPV-C).

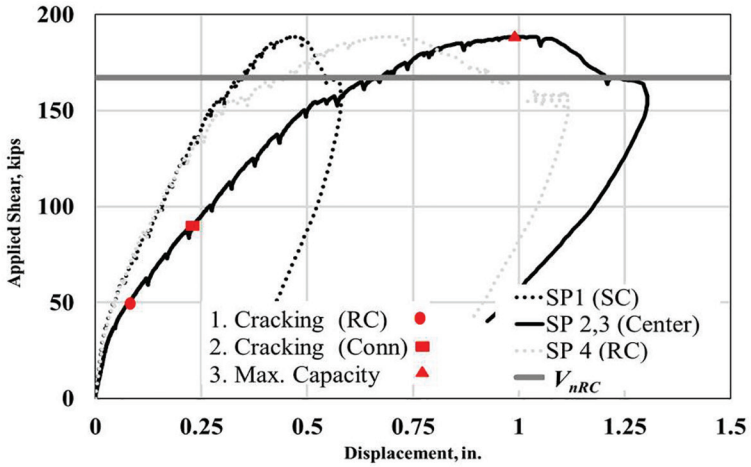

Fig. 27. Applied shear-displacement response (OOPV-DN).

steel components of the connection region remained well within the elastic range.

The overall damage progression in terms of concrete crack patterns is again similar to OOPV-C as shown in Figure 29. Initially, flexural cracks occurred in the bottom of the RC wall portion near the loading point at $0.26V_{max}$. These cracks transformed into flexural-shear cracks along with the formation of additional cracks within the RC wall portion. Shear cracks appeared in the connection region at around 90 kips. Ultimately, the specimen failed due to inelastic diagonal cracks that connected the loading point and RC wall portion support.

Specimen IPV-C

Figure 30 shows the applied force-displacement response of Specimen IPV-C. The response was developed using the measured displacement from SP1. As shown, the specimen behaved in an elastic manner during the first six cycles ($0.25H_n$ and $0.50H_n$). During the first $0.75H_n$ cycle, #5 rebar located at the far south side of the specimen started yielding. During the first $1.5\Delta_y$ cycle, the specimen reached the maximum load, $V_{max.push}$, of 582 kips in push and 576 kips ($V_{max.pull}$) in pull, resulting in the average maximum load, V_{max}, of 579 kips. The corresponding lateral displacements were 0.59 in. (push) and 0.66 in. (pull). The concrete at the

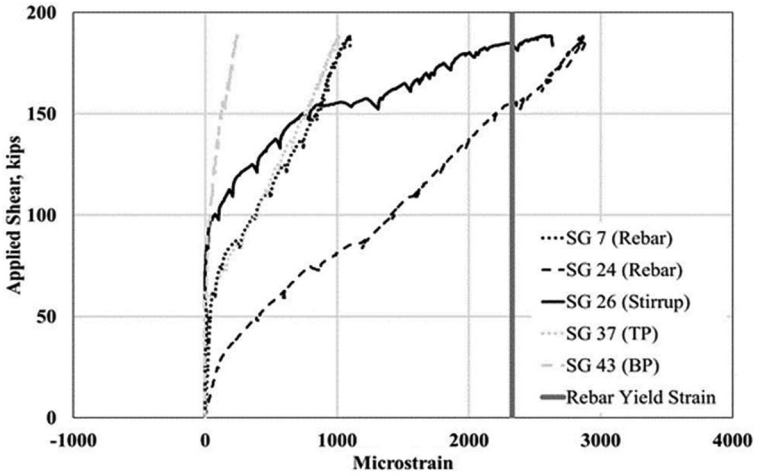

Fig. 28. Applied shear-strain response—#14 rebar, #4 stirrups, tie plate, and baseplate (OOPV-DN).

Fig. 29. Concrete crack pattern (east side) (OOPV-DN).

north toe of the RC wall portion started crushing just before V_{max}. V_{max} is greater than the shear capacity of the RC wall portion ($10f_c'^{0.5}A_c$ = 554 kips) calculated using ACI 349-06 with measured material properties by 25 kips (5%). The load carrying capacity started decreasing due to extensive concrete cracks in the RC wall portion. The specimen failed during the second $2.0\Delta_y$ cycle (push) due to large shear cracks inducing shear failure mode.

Figure 31 shows the applied force–strain response of #5 rebar, tie plates, and wing plates. As shown, the #5 rebar started yielding during the first $0.75H_n$ cycle. The response collected during the first $1.5\Delta_y$ cycle shows that the exterior tie plate (SG 26) almost reached its yield strength exhibiting the maximum strain of 1,932 microstrain (corresponding to 56.0 ksi). The figure also shows the response of wing plates. As presented, it appears that the exterior wingplate (SG 31) exhibited the maximum strain of only –365 microstrain (corresponding to –10.6 ksi). The overall damage progression in terms of concrete crack patterns is shown in Figure 32. Initially, flexural concrete cracks appeared from both ends of the specimen. The RC flexural cracks transformed into flexural-shear cracks, and additional shear cracks were formed during subsequent loading cycles. Eventually, the specimen failed in shear as major shear cracks occurred in the middle of the specimen.

Specimen IPV-DN

Figure 33 shows the overall applied force-displacement behavior of Specimen IPV-DN. As shown, the response was very similar to the specimen tested with the coupler connection plan (IPV-C). The specimen remained in the elastic range during the initial six cycles ($0.25H_n$ and $0.50H_n$). During the first $0.75H_n$ cycle, #5 rebar located at the far south side of the specimen started yielding. During the first $1.5\Delta_y$

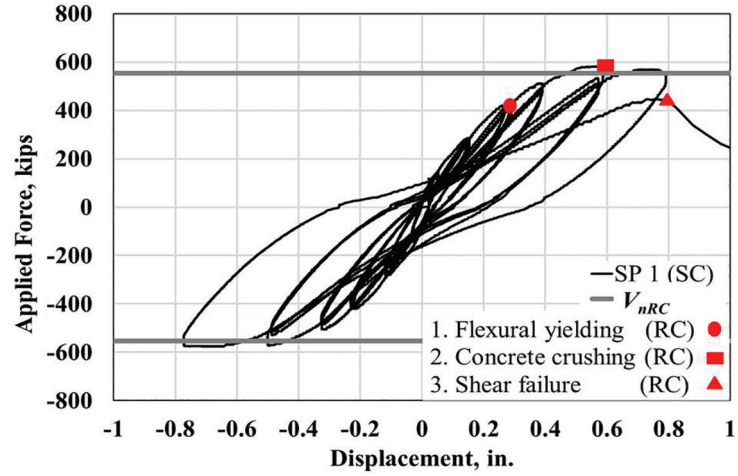

Fig. 30. Applied force-displacement response (IPV-C).

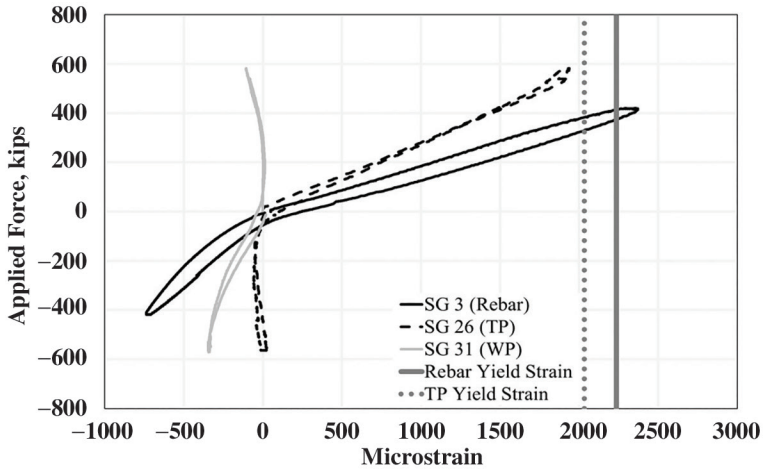

Fig. 31. Applied force-strain response—$0.75H_n$ and $1.5\Delta_y$ (first cycles) (IPV-C).

(a) Elevation view RC wall portion

(b) Side view RC wall portion

Fig. 32. RC wall failure—concrete cracking and spalling (IPV-C).

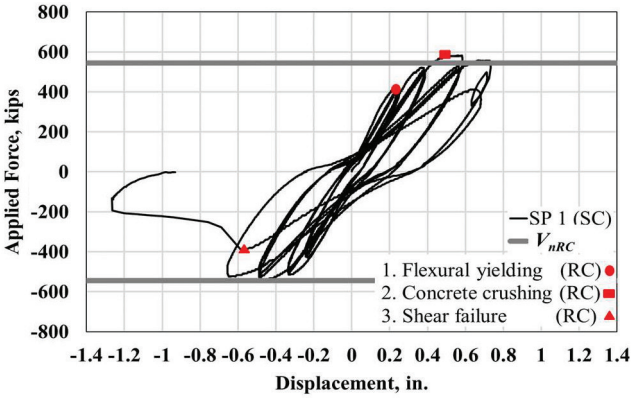

Fig. 33. Applied force-displacement response (IPV-DN).

cycle, the specimen reached the maximum load, $V_{max.push}$, of 582 kips in push and 550 kips in pull, resulting in the average maximum load, V_{max}, of 566 kips. The corresponding lateral displacements were 0.57 in. (push) and 0.46 in. (pull). V_{max} is greater than the shear capacity of the RC wall portion ($10f_c'^{0.5}A_c$ = 531 kips) calculated using ACI 349-06 with measured material properties by 35 kips (or 6%). The concrete at the base of the RC wall portion started crushing just before V_{max}. The load-carrying capacity decreased after V_{max} due to inelastic concrete cracks in the RC wall portion. Ultimately, the specimen failed in shear during the second $2.0\Delta_y$ cycle (pull).

Figure 34 shows the applied force–strain response of #5 rebar and tie plates. As presented, the #5 rebar started yielding during the first $0.75H_n$ cycle. The response collected during the first $1.0\Delta_y$ cycle shows that the exterior tie plate (SG 25) reached its yield strength exhibiting the maximum strain of 2,193 microstrain (63.6 ksi). Figure 35 shows the concrete crack pattern after $2.0\Delta_y$ cycle. As shown, flexural concrete cracks appeared initially from both ends of the specimen, exhibiting a flat (horizontal) crack angle. As the loading increased, additional cracks were formed with inclined crack angles. Eventually, the specimen failed in shear as major cracks occurred in the middle of the specimen.

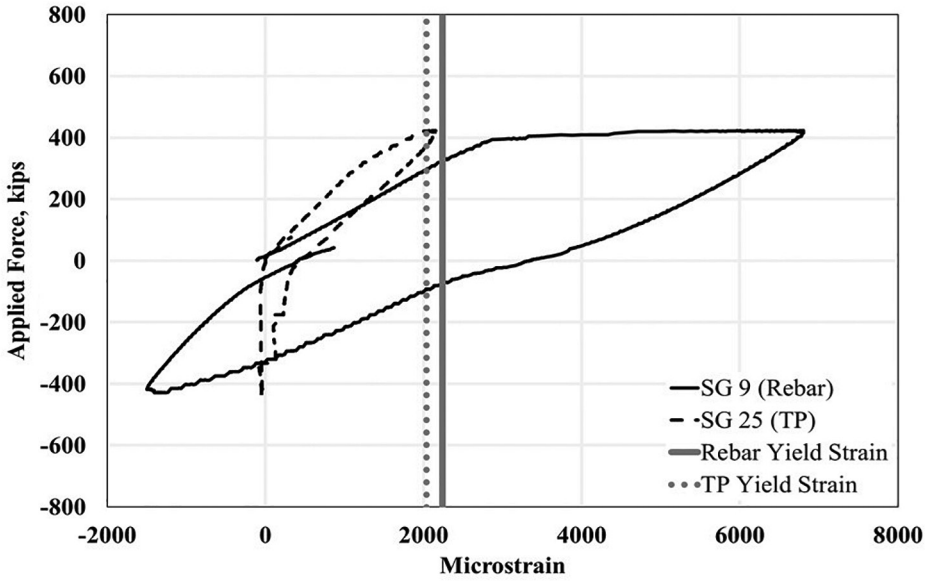

Fig. 34. Applied force strain response—0.75Hn and 1.0Δ_y (first cycles) (IPV-DN).

(a) East side *(b) North side*

Fig. 35. RC wall damage progression (IPV-DN).

FINITE ELEMENT ANALYSES

This section presents the details of three-dimensional (3-D) finite element models (FEMs) developed using LS-DYNA explicit solver (LS-DYNA, 2012a, 2012b). The developed models explicitly accounted for the geometric and material nonlinearities. Numerical analyses were conducted to gain an additional insight into the performance and efficacy of the designed mechanical connection. Details related to the analysis approach, material models, input parameters, and numerical verification of the test results are discussed in the following sections.

Modeling Approach

Numerical models for simulations were created replicating the exact specimen design details covered in the experimental program. SC wall faceplates, tie plates, wing plates, and baseplates of the connection region, and RC wall flexural reinforcement were modeled with 1 in. mesh size solid elements employing full integration element formulation (ELFORM -1). The respective concrete regions of SC and RC walls were also modeled with 1 in. solid elements, however, employing a constant stress reduced integration formulation (ELFORM 1) (LS-DYNA, 2012a, b). The rationale for both these integration techniques used for solid elements in LS-DYNA has been discussed in Part 1 of Seo et al. (2022), and therefore will not be repeated here. Hughes-Liu beam element formulation (1 in. mesh size) with cross-section integration (ELFORM 1) was used to model the RC wall shear reinforcement, SC wall shear connectors, and tie bars. Additionally, other researchers including Bruhl et al. (2015b) and Epackachi et al. (2015b) have also recommended these solid and beam element formulations.

RC wall reinforcement, SC wall shear connectors and tie bars, and the connection region were constrained in respective concrete portions using Constrained_Lagrange_In_Solid (CLIS) keyword depicting a perfect bond. Interaction at the interface between faceplate and infill SC wall concrete, RC wall and SC wall respective concrete portions, and RC wall and foundation concrete (IPV model) were defined via Automatic_Surface_To_Surface contact formulation. This two-way general contact algorithm protects the slave and master nodes against penetration. Additionally, the length of the RC wall vertical rebar extending inside the connection region was less than the development length as per ACI 349 (ACI, 2006), therefore, the same contact definition was used to define their interaction with SC wall infill concrete. Details of LS-DYNA 3D models for OOPV and IPV specimens are presented in Figure 36 and Figure 37.

Material Models and Properties

Material models for simulations were chosen from the library of LS-DYNA (LS-DYNA, 2012a, 2012b). Winfrith_Concrete (MAT 84) and Continuous_Surface_Cap_Model (CSCM) concrete (MAT 159) material models were utilized for simulating IPV and OOPV tests, respectively. The smeared cracking constituent material model (MAT 84) can capture the critical cyclic IPV behavior of concrete such as shear force transfer across cracks due to aggregate interlock, opening and closing of cracks, loss of strength and stiffness parallel to cracks, and tension stiffening, etc. (Teh Hu and Schnobrich; 1990, Vecchio and DeRoo, 1995; Epackachi et al., 2015b). It assumes an elastic perfectly plastic response in compression with plasticity portion based on shear failure surface proposed by Ottosen (1977). The post-cracking behavior of the material model in the tensile region can be simulated using Wittmann's fictitious crack model (Schwer, 2011) based on fracture energy. The fracture energy, G_f, is defined as energy dissipated per unit area during crack opening, and it is equal to the area under the tensile stress-crack width curve. The linear relationship between tensile stress and crack width is considered in this study. Crack width, ω, can be estimated from Equations 6 and 7 (Wittmann et al., 1988), where f_t is the uniaxial tensile strength and Φ is the maximum aggregate size.

$$\omega = \frac{2G_f}{f_t} \tag{6}$$

$$G_f = 1.297\Phi^{0.32} \tag{7}$$

The CSCM concrete material model was developed by the U.S Department of Transportation to predict the performance of concrete involved in roadside safety structures. It is an isotropic model that requires only basic strength data in the form of concrete strength, f'_c, and aggregate size. The cardinal difference between CSCM and the Winfrith model is its ability to model strain softening and modulus reduction in compression. A failure criterion in the form of maximum principal strain (MXEPS) was artificially included by defining MAT_ADD_EROSION keyword in OOPV analysis. MXEPS was calculated using Equation 8 as reported by Yang (2015), where V_e is the volume of one solid element. For IPV numerical models, element erosion was not activated due to the cyclic nature of loading protocol for actual test specimens.

$$\text{MXEPS} = \frac{\omega}{\sqrt[3]{V_e}} \tag{8}$$

The Piecewise_Linear_Plasticity (MAT 24) material model was used to simulate SC wall faceplates, connection region tie plates, wing plates, baseplates, and RC wall reinforcement. It provides the flexibility of explicitly modeling the post-yield behavior in the form of effective stress–plastic strain input curves obtained from uniaxial tensile coupon tests performed during specimen testing. SC wall

shear connectors and tie bars were modeled with a plastic kinematic (MAT 03) material model. Due to the quasi-static nature of these tests, the strain rate effects were not activated in either of these steel material models. Table 3 provides the concrete and steel material properties used in the numerical analyses. The input compressive and tensile strengths were based on the average values obtained from the material tests performed on respective test days.

Numerical Results and Discussion

Figure 38 shows the applied shear–displacement response of the numerical model compared with the experimentally observed behavior (OOPV-C test specimen). The displacement is the numerically predicted displacement under loading point. As shown, the numerical model predicts a somewhat soft response. The reason is attributed to the inherent behavior of the CSCM concrete material model. This material model is an isotropic damage model opposed to anisotropic behavior of concrete in a shear (biaxial) stress state where the compression strut can continue to carry compressive stress after tensile cracking in the orthogonal direction. Nevertheless, the numerical results are in favorable agreement with the observed behavior. The maximum shear, $V_{max}FEA$, predicted by the model is 191 kips, which is greater than the RC shear capacity ($V_{n.RC}$ = 167 kips) calculated using ACI 349-06 by 24 kips. $V_{max}FEA$ is in favorable agreement with $V_{n.RC}$. Additionally, the maximum stress predicted in the bottom layer of #14 rebar is approximately 94 ksi, which also confirms the assumption made using the mechanical connection design philosophy that the maximum axial force that needs to be transferred to the SC wall is 125% of the yield strength of the reinforcing bars

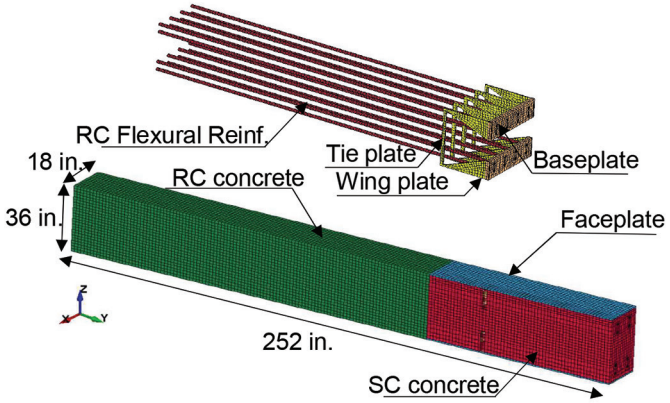

(a) Solid elements

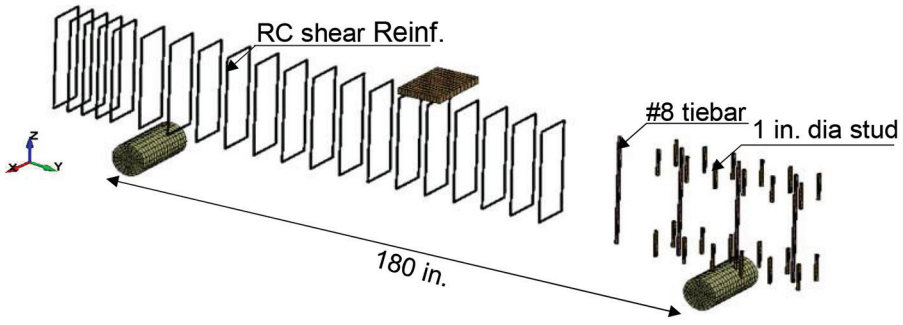

(b) Beam elements

Fig. 36. FEM element formulations (OOPV).

Table 3. Input Parameters for LS-DYNA Material Models			
Material Type	**Input Parameters**	**Value / Equation**	**Reference**
Concrete	Mass density	2.25×10^{-4} lbf s^2/in.^{4}	
	Unconfined compression strength	Table 2	Based on material tests
	Maximum aggregate size	0.75 in. (OOPV), 0.375 in. (IPV)	Experimental data
	Erosion criteria: *MXEPS*	0.005	$\text{MXEPS} = \frac{\omega}{\sqrt[3]{V_e}}$ Equation 8
Steel	Mass density	7.34×10^{-4} lbf s^2/in.^{4}	
	Young's modulus	2.9×10^7 psi	
	Poisson's ratio	0.3	
	Yield strength	Table 2	Based on material tests
	Failure strain		Based on material tests
	Hardening variable	0	LS-DYNA, 2012a, 2012b

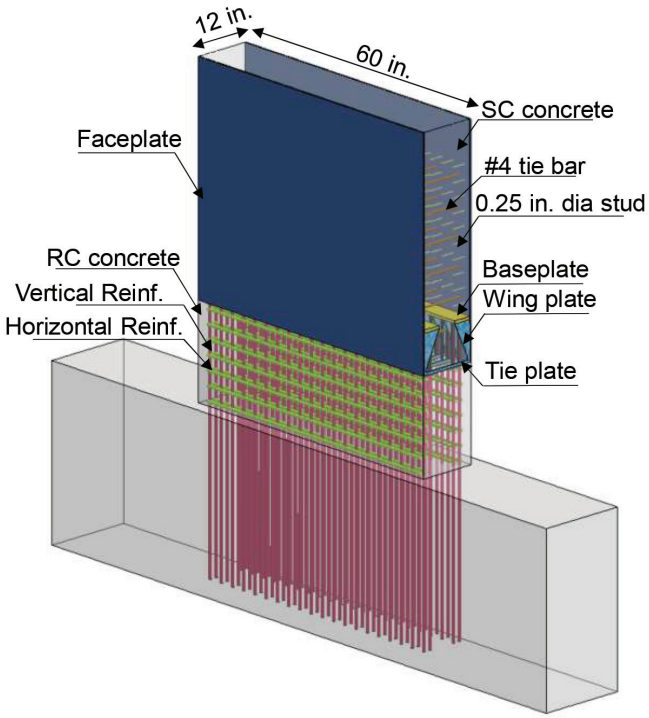

Fig. 37. LS-DYNA model (IPV).

($1.25F_{y,r}$ = 85 ksi). Strain contour plots of the mechanical connection region are shown in Figure 39. As presented, all steel components (including tie plate, wing plate, and baseplate) in the connection region remained in the elastic range until the connected RC wall portion failed in shear. Additionally, wing and baseplates were subjected to lower strain as compared to tieplates due to a significant concrete contribution, similar to what was observed during experimental verification.

Figure 40 shows the applied shear–displacement response of the numerical model compared with the experimentally measured response of the IPV-C test specimen. The displacement is the numerically predicted value at the loading point (60 in. from the base of RC wall). The model underwent a series of events such as vertical rebar yielding, tie bar yielding, and stud yielding (not shown here for brevity). The analysis was eventually stopped due to unstable shear failure of the RC wall portion after exceeding its shear capacity ($V_{n.RC}$ = 554 kips). The maximum shear force predicted from the model, V_{maxFEA}, is 564 kips. V_{maxFEA} is in favorable agreement with $V_{n.RC}$ within an accuracy of 2%. Longitudinal strain contour plots of the mechanical connection region are shown in Figure 41. The maximum respective strain values in tie plates, wing plates, and baseplates at V_{maxFEA} indicate that all steel components in the connection region remained in the elastic range and the wing and baseplates were subjected to lower strain as compared to the tieplates. The predicted strain values for both OOPV and IPV models were lower than the experimentally observed response. This is attributed to the treatment of the connection region in the numerical models. The connection region was embedded inside the infill concrete in

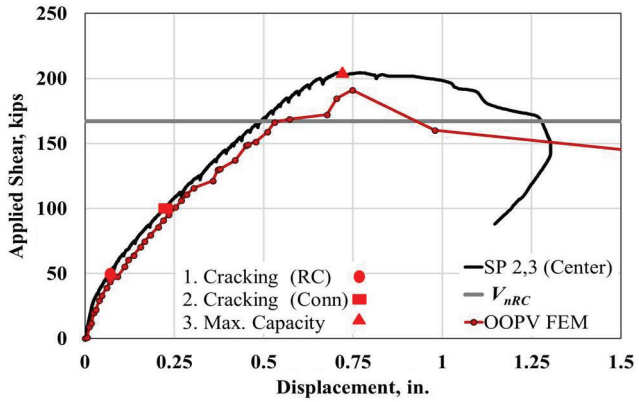

Fig. 38. Comparison between experimental (OOPV-C) and FEA results.

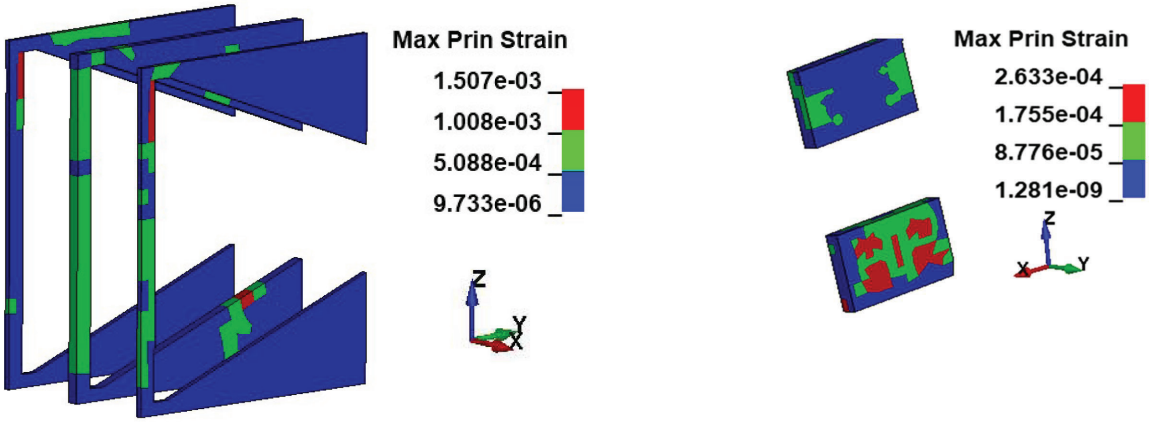

(a) Tie plate and wing plate *(b) Baseplate*

Fig. 39. OOPV strain contour plot.

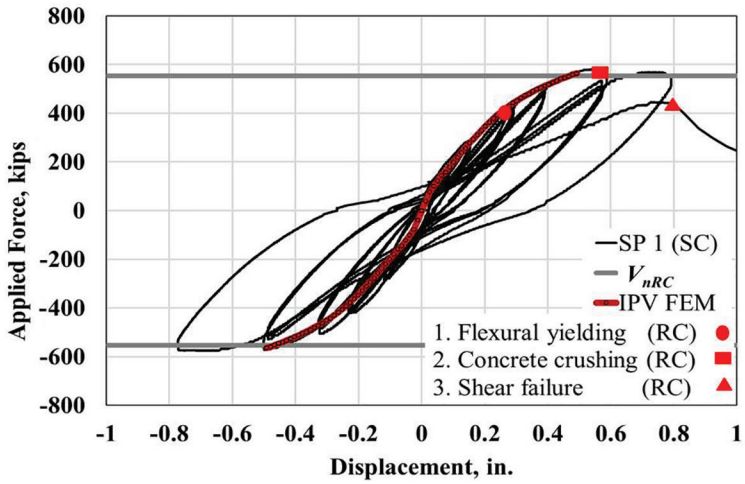

Fig. 40. Comparison between experimental (IPV-C) and FEA results.

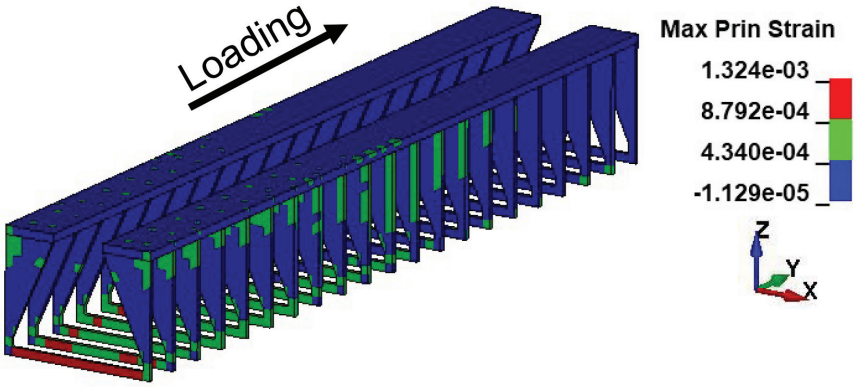

Fig. 41. Connection region strain contour plot (IPV).

Table 4. Summary of Test Results						
Specimen	Maximum Load ^{Exp}, P_{max}, V_{max} (kips)	Maximum Load ^{FEA}, P_{max}^{FEA}, V_{max}^{FEA} (kips)	RC Capacity, P_{MnRC}, V_{nRC} (kips)	Max. Load^{Exp} RC Capacity	Max. Load^{FEA} RC Capacity	Failure Mode
OOPM-C	585	571	495	1.18	1.15	RC flexural yielding
OOPM-DN	571		494	1.15		RC flexural yielding
OOPV-C	205	191	167	1.23	1.14	RC shear
OOPV-DN	189		167	1.13		RC shear
IPV-C	579	564	554	1.04	1.02	RC shear
IPV-DN	566		531	1.06		RC shear

Table 5. Comparison Between Maximum Steel Strain and Stress Values							
		Maximum Microstrain (in./in. × 10^{-6})			Maximum Stress (ksi)		
Verification	Specimen	Tie plate	Wing plate	Baseplate	Tie plate	Wing plate	Baseplate
Experimental	OOPM-C	1436	360	802	42	10	23
	OOPM-DN	1671	297	176	49	9	5
	OOPV-C	1370	60	436	40	2	13
	OOPV-DN	1012	100	245	29	3	7
	IPV-C	1932	365	–	56	11	–
	IPV-DN	2193	–	–	64	–	–
Numerical	OOPM	1600	313	120	46	9	4
	OOPV	855	194	147	25	6	4
	IPV	1280	131	–	37	4	–

the models depicting a perfect bond, whereas limited bonding was achieved in the test specimens. Nevertheless, the predicted response is in reasonable agreement with the observed behavior.

SUMMARY AND CONCLUSIONS

This section presents the important findings and conclusions from the complete study including both Part 1 (Seo et al., 2022) and Part 2 of this series of papers. The study aimed at the development and validation (both experimental and numerical) of the performance, strength, ductility, and failure modes of the designed mechanical connection. The designed connection was based on a full-strength connection design philosophy. The experimental program involved testing seven mechanical connections comprised of four full-scale and three scaled specimens. Full-scale specimens were subjected to monotonic out-of-plane moment (OOPM) and out-of-plane shear (OOPV). The remaining three scaled specimens were subjected to cyclic in-plane shear (IPV). The two rebar-to-baseplate connection configurations—coupler (C) and double nut (DN)—were tested. The observed applied force–displacement and applied force–steel strain responses were evaluated to determine the ultimate strength and governing failure modes. Additionally, detailed finite element models (FEMs) were developed and benchmarked against experimental data to gain an additional insight into the connection behavior and to compensate for the limited experimental database.

Table 4 summarizes the results from the experimental and numerical investigation. As presented, the observed and predicted governing failure mode of all test specimens is either RC flexural yielding or RC shear failure. The experimentally observed maximum loads, P_{max} and V_{max}, of all test specimens exceeded their respective RC capacities, $P_{Mn.RC}$ and $V_{n.RC}$. In addition, the predicted maximum loads, P_{max}^{FEA} and V_{max}^{FEA}, of all three numerical models are greater than the respective RC capacities, $P_{Mn.RC}$ and $V_{n.RC}$,

and are in reasonable agreement with the observed values. Table 5 presents a summary of maximum strain and the corresponding stress values of the steel components in the connection region from both experimental and numerical verification. As shown, all steel components (including tieplates, wing plates, and baseplates) in the connection region remained in the elastic range, except the tieplates of Specimen IPV-DN, until the connected RC wall portion developed its capacity (either RC flexural yielding or RC shear). For Specimen IPV-C and IPV-DN relatively higher tie plate strain values are attributed to the location of gauges on the test specimens, i.e., strain gauges were installed on the two exterior tieplates (3⁄16 in.) which were thinner than the interior tieplates (3⁄8 in.) by 50%.

The results from both experimental and numerical investigations concluded that:

(1) SC wall-to-RC wall mechanical connections should be designed and detailed to develop the full-strength of the weaker of the two connected structures in order to ensure energy dissipation away from the connection region during a design level earthquake.

(2) The type of rebar-to-baseplate connection configuration, coupler (C) or double nut (DN), does not have a significant influence on the force transfer mechanism of the designed connection.

(3) Tieplates connecting the two opposite faceplates are recommended in the connection region to resist the tensile component of the moment generated due to the eccentricity associated with force transfer from rebar to faceplates.

(4) Due to rebar congestion caused by a high steel reinforcement ratio, caution is required in cases with cast-in-place concrete near the connection region and RC wall portion to prevent honey combing, voids, and premature failure. Self-consolidating concrete is recommended under such situations.

(5) All the steel components in the connection region including tie plates, wing plates, and baseplates remained in the elastic range until the RC wall developed its flexural or shear capacity.

(6) Experimentally observed and numerically predicted strain values in the wing plates and baseplates remained below their respective yield strains. This is attributed to the significant contribution of concrete during the force transfer from RC-to-SC structure exhibiting conservatism in the designed mechanical connection.

(7) The proposed connection design procedure is suitable and conservative for SC wall-to-RC wall mechanical connections.

(8) Additional experimental and numerical studies are recommended to further expand the limited database, and to evaluate the influence of different design parameters including wall thickness, rebar layers, rebar-to-baseplate connection, and tie plate configuration, etc.

ACKNOWLEDGEMENTS

The authors would like to acknowledge the valuable contribution of KEPCO E&C, Korea, (sponsor) and all the technical staff involved in the experimental and numerical work during the execution of the project. However, the views presented in this paper are solely that of the authors.

REFERENCES

ACI (2006), *Code Requirements for Nuclear Safety-Related Concrete Structures (ACI 349-06) and Commentary*, ACI 349-06, American Concrete Institute, Farmington Hills, Mich.

ACI (2019), *Building Code Requirements for Structural Concrete*, ACI 318-19, American Concrete Institute, Farmington Hills, Mich.

AISC (2015), *Specification for Safety-Related Steel Structures for Nuclear Facilities Including Supplement No. 1*, ANSI/AISC N690s1-15, American Institute of Steel Construction, Chicago, Ill.

AISC (2018), *Specification for Safety-Related Steel Structures for Nuclear Facilities*, ANSI/AISC N690-18, American Institute of Steel Construction, Chicago, Ill.

AISC (2019), *Companion to the AISC Steel Construction Manual Volume 1: Design Examples*, Version 15.1, American Institute of Steel Construction, Chicago, Ill.

ASTM (2013), *Standard Test Method for Tension Testing of Metallic Materials*, ASTM E8/E8M, ASTM International, West Conshohocken, Pa.

ASTM (2014), *Standard Test Method for Compressive Strength of Cylindrical Concrete Specimens*, ASTM C39/C39M, ASTM International, West Conshohocken, Pa.

Anvari, A. T., Bhardwaj, S.R., Wazalwar, P., and Varma, A.H. (2020), "Stability of Speedcore Walls Under Fire Loading: Summary of Numerical Analyses," *Proceedings of the Annual Stability Conference, Structural Stability Research Council*, April 21–24, Atlanta, Ga.

Bhardwaj, S.R. and Varma, A.H. (2017), *Design of Modular Steel-Plate Composite Walls for Safety Related Nuclear Facilities*, Design Guide 32, AISC, Chicago, Ill.

Biskinis, D.E., Roupakias, G.K., and Fardis, M.N. (2004), "Degradation of Shear Strength of Reinforced Concrete Members with Inelastic Cyclic Displacements," *ACI Structural Journal*, Vol. 101, Issue 6, pp. 773–783.

Booth, P.N., Bhardwaj, S.R., Tseng, T.C., Seo, J., and Varma, A.H. (2020), "Ultimate Shear Strength of Steel-Plate Composite (SC) Walls with Boundary Elements," *Journal of Constructional Steel Research*, Vol. 165. https://doi.org/10.1016/j.jcsr.2019.105810

Bruhl, J., Varma, A.H., and Johnson, W.H. (2015a), "Design of Composite SC Walls to Prevent Perforation from Missile Impact," *International Journal of Impact Engineering*, Vol. 75, pp. 75–87. http://dx.doi.org/10.1016/j.ijimpeng.2014.07.015

Bruhl, J.C., Varma, A.H., and Kim, J.M. (2015b), "Static Resistance Function for Steel-Plate Composite (SC) Walls Subject to Impactive Loading," *Nuclear Engineering and Design,* Vol. 295, pp. 843–859. https://doi.10.1016/j.nucengdes.2015.07.037

Carrillo, J. and Alcocer, S.M. (2013), "Shear Strength of Reinforced Concrete Walls for Seismic Design of Low-Rise Housing," *ACI Structural Journal*, Vol. 110, Issue 3.

DOE (2006), "Accident Analysis for Aircraft Crash into Hazardous Facilities," DOE-STD-3014, U.S. Department of Energy, Washington, D.C.

Epackachi, S., Nguyen, N.H., Kurt, E.G., Whittaker, A.S., and Varma, A.H. (2015a), "In-Plane Seismic Behavior of Rectangular Steel-Plate Composite Wall Piers," *Journal of Structural Engineering*, Vol. 141, Issue 7. http://dx.doi.10.1061/(ASCE)st.1943-541x.0001148

Epackachi, S., Whittaker, A.S., Varma, A.H., and Kurt, E.G. (2015b), "Finite Element Modeling of Steel-plate Concrete Composite Wall Piers," *Engineering Structures*, Vol. 100, pp. 369–384.

Hwang, K.M., Lee, K.J., and Kim, W.K. (2013), "An Experimental Study on the Flexural and Shear Behavior of Steel Plate Concrete—Reinforced Concrete Connected Structures," *Nuclear Engineering and Design*, Vol. 257, pp. 88–99. https:// dx.doi.org/10.1016/j.nucengdes.2012.12.020

IAEA (2011), "Construction Technologies for Nuclear Power Plants," IAEA Nuclear Energy Series No. NP-T-2.5, International Atomic Energy Agency, Vienna.

JEAC (2009), *Technical Code for Seismic Design of Steel Plate Reinforced Concrete Structures: Buildings and Structures*, JEAC-4618, Japanese Electric Association Nuclear Standards Committee, Tokyo, Japan.

Kurt, E.G. (2016), "Steel-Plate Composite (SC) Walls and their Basemat Connections: Seismic Behavior, Analysis, and Design," Ph.D. Dissertation, Purdue University, West Lafayette, Ind.

LS-DYNA (2012a), Keyword User's Manual, Volume I, Version 971 R6.0.0, Livermore Software Technology Corporation (LSTC), Livermore, Calif.

LS-DYNA (2012b), Keyword User's Manual, Volume II, Version 971 R6.0.0, Livermore Software Technology Corporation (LSTC), Livermore, Calif.

Mo, Y.L., Zhong, J., and Hsu, T.C. (2008), "Seismic Simulation of RC Wall-Type Structures," *Engineering Structures*, Vol. 30, Issue 11, pp. 3,2167–3,175.

Ottosen, N.S. (1977), "A Failure Criterion for Concrete," *Journal of Engineering Mechanics Division*, Vol. 103, No. 4, pp. 527–535.

Ozaki, M., Akita, S., Osuga, H., Nakayama, T., and Adachi, N. (2004), "Study on Steel Plate Reinforced Concrete Panels Subjected to Cyclic In-Plane Shear," *Nuclear Engineering and Design*, Vol. 228, pp. 225–244. https://doi.org/10.1016/j.nucengdes.2003.06.010

Schwer, L. (2011). "The Winfrith Model: Beauty or Beast? Insights into the Winfrith Concrete Model," *Proceedings of the 8th European LS-DYNA Users Conference*, Strasbourg.

Sener, K., Varma, A.H., Booth, P.N., and Fujimoto, R. (2015), "Seismic Behavior of a Containment Internal Structure Consisting of Composite SC Walls," *Nuclear Engineering and Design*, Vol. 295, pp. 804–816. http://dx.doi.org/10.1016/j.nucengdes.2015.07.038

Sener, K.C., and Varma, A.H. (2021), "Steel-Plate Composite Walls with Different Types of Out-of-Plane Shear Reinforcement: Behavior, Analysis, and Design," *Journal of Structural Engineering*, Vol. 147, Issue 2. https://doi.10.1061/(ASCE)st.1943-541x.0002870

Seo, J., Varma, A.H., Sener, K., and Ayhan, D. (2016), "Steel-Plate Composite (SC) Walls: In-Plane Shear Behavior, Database, and Design," *Journal of Constructional Steel Research*, Vol. 119, pp. 202–215. https://doi.org/10.1016/j.jcsr.2015.12.013

Seo, J. and Varma, A.H. (2017a), "Experimental Behavior and Design of Steel Plate Composite-to-Reinforced Concrete Lap Splice Connections," *Journal of Structural Engineering*, Vol. 143, Issue 5. https://doi. 10.1061/(ASCE)st.1943-541x.0001711

Seo, J. and Varma, A.H. (2017b), "SC Wall-to-Slab Connections in Safety Related Nuclear Facilities," *Proceedings of the 24th International Conference on Structural Mechanics in Reactor Technology (SMiRT-24)*, August 20–25, Busan, Korea.

Seo, J., Anwar, H.S., and Varma, A.H. (2022), "Steel-Plate Composite (SC) Wall-to-Reinforced Concrete (RC) Wall Mechanical Connection- Part 1," *Engineering Journal*, AISC, Vol. 59, No.1, pp. 31–52.

Teh Hu, H. and Schnobrich, W.C. (1990), "Nonlinear Analysis of Cracked Reinforced Concrete," *ACI Structural Journal*, Vol. 87, No. 2, pp. 199–207.

Usta, M. (2017), "Shear Strength of Structural Walls Subjected to Load Cycles," Ph.D. Dissertation, Purdue University, West Lafayette, Ind.

Varma, A.H., Malushte, S.R., Sener, K.C., and Lai, Z. (2014), "Steel-Plate Composite (SC) Walls for Safety Related Nuclear Facilities: Design for In-Plane Forces and Out-of-Plane Moments," *Nuclear Engineering and Design*, Vol. 269, pp. 240–249. https://dx.doi.org/10.1016/j.nucengdes.2013.09.019

Vecchio, F.J. and DeRoo, A. (1995), "Smeared-Crack Modeling of Concrete Tension Splitting," *Journal of Engineering Mechanics*, Vol. 121, No. 6.

Wittmann, F.H., Rokugo, K., Bruhwiler, E., Mihashi, H., and Simonin, P. (1988), "Fracture Energy and Strain Softening of Concrete as Determined by Means of Compact Tension Specimens," *Materials and Structures*, Vol. 21, Issue 121, pp. 21–32.

Yang, Y. (2015), "Shear Strength and Behavior of Reinforced Concrete Structures with T-Headed Bars in Safety-Related Nuclear Facilities," Ph.D. Dissertation, Purdue University, West Lafayette, Ind.

Guide for Authors

Scope

Engineering Journal is dedicated to the improvement and advancement of steel construction. Its pages are open to all who wish to report on new developments or techniques in steel design, research, the design and/or construction of new projects, steel fabrication methods, or new products of significance to the uses of steel in construction. Only original papers should be submitted.

General

Papers intended for publication should be submitted by email Margaret Matthew, editor, at **matthew@aisc.org**.

The articles published in the *Engineering Journal* undergo peer review before publication for (1) originality of contribution; (2) technical value to the steel construction community; (3) proper credit to others working in the same area; (4) prior publication of the material; and (5) justification of the conclusion based on the report.

All papers within the scope outlined above will be reviewed by engineers selected from among AISC, industry, design firms, and universities. The standard review process includes outside review by an average of three reviewers, who are experts in their respective technical area, and volunteers in the program. Papers not accepted will not be returned to the author. Published papers become the property of the American Institute of Steel Construction and are protected by appropriate copyrights. No proofs will be sent to authors.

Manuscripts

Manuscripts must be provided in Microsoft Word format. Include a PDF with your submittal so we may verify fonts, equations and figures. View our complete author guidelines at **aisc.org/ej**.

Smarter. Stronger. Steel.

American Institute of Steel Construction
130 E Randolph St, Ste 2000, Chicago, IL 60601
312.670.2400 | aisc.org/ej